MULTICONTRAST MRI OF ATHEROSCLEROTIC PLAQUES: ACQUISITION, CHARACTERIZATION AND RECONSTRUCTION

A Thesis
Presented to
The Academic Faculty

by

Binjian Sun

In Partial Fulfillment
of the Requirements for the Degree
Doctor of Philosophy in the
Department of Biomedical Engineering

Georgia Institute of Technology
August 2007

MULTICONTRAST MRI OF ATHEROSCLEROTIC PLAQUES: ACQUISITION, CHARACTERIZATION AND RECONSTRUCTION

Approved by:

Dr. Don P. Giddens, Advisor
Department of Biomedical Engineering
Georgia Institute of Technology

Dr. John N. Oshinski, Co-advisor
Department of Biomedical Engineering
Georgia Institute of Technology

Dr. Raymond P. Vito
School of Mechanical Engineering
Georgia Institute of Technology

Dr. W. Robert Taylor
School of Medicine
Emory University

Dr. Robert C. Long, Jr.
Department of Radiology
Emory University

Date Approved: 18 June 2007

This thesis is dedicated to my family ...

ACKNOWLEDGEMENTS

It is such a blessing for me to have the tremendous help offered by many people all along the journey of my doctoral years. I couldn't imagine how dull the life will be without their support and encouragement!

I must first express my deepest gratitude to my dissertation committee: Drs. Don P. Giddens, John N. Oshinski, W. Robert Taylor, Raymond P. Vito and Robert C. Long, Jr. My thesis advisors, Dr. Giddens and Dr. Oshinski, deserve special recognition for their exceptional guidance. Their extensive knowledge, eminent insight and genuine kindness make me feel so privileged to research under their supervision! The remarkable education and enlightening suggestions my committee members offered greatly inspired the development of the current thesis. Their encouragement and patience indeed motivated me to purse new directions in research. Furthermore, I thank other faculty members who provided immense contributions to this thesis. In particular, I must acknowledge Dr. David Vega, Dr. Diana Weiss and Ms. Giji Joseph. Additionally, much appreciation to Dr. Hui Mao, Dr. Puneet Sharma and Dr. Marijn Brummer from the Frederik Philips MR Research Center.

I am grateful to Ms. Joanne Wheatley, Ms. Lisa Cox, Ms. Marvis Zanders and Mr. Christopher Ruffin for the kind assistance they provided. Moreover, I acknowledge the MRI lab members: Kevin, Jana and Brandon; and everyone from the cardiovascular lab: Amanda, Suo Jin, Yan, Stephanie, Massimiliano, Sungho, Yi and Annica. It has been my greatest pleasure to work with them and I cherish the time we spent together in the lab.

I thank my parents, Chao Sun and Ruilin Zeng, my brother, Binyuan Sun, for their persistent encouragement all through my life. Their emotional support empowers me to face the rough time courageously and strive to achieve the exceptional. I owe special thanks to my long term friends Qiangguo, Ruifeng and their families. The laughters and happiness they brought to my life is invaluable.

Most of all, I am deeply indebted to my wife, Lei Zhang, for her unconditional love and

support in every way. She always knows how to ease me when I feel anxious. Our marriage is the most successful project I have ever accomplished.

TABLE OF CONTENTS

LIST OF TABLES

LIST OF FIGURES

SUMMARY

Cardiovascular Disease (CVD) continues to be the leading cause of death in western countries according to the statistics update by the American Heart Association. Atherosclerosis is estimated to be responsible for a large portion of CVD and affects 60 million people in the United States. Accurate diagnosis is crucial for proper treatment planning. Currently, the clinical standard screening technique for diagnosing atherosclerosis is x-ray angiography, which reveals the residual lumen size. X-ray angiographic images possess good resolution and contrast, however, lumen size is not always a proper criterion given the positive remodeling nature of atherosclerotic plaques. In the past decade, it has been shown that most plaques responsible for a fatal or nonfatal myocardial infarction are less than 70% stenosed. Clinical data support the idea that plaques producing non-flow-limiting stenoses account for more cases of plaque rupture and thrombosis than plaques producing a more severe stenosis. Due to this fact, plaque itself must be imaged in order to assess its vulnerability. A wealth of literature suggests that multicontrast MRI has the potential of characterizing plaque constituents, and thus is a promising technique for plaque imaging.

Because of the technical difficulties associated with *in-vivo* plaque imaging and the fact that our research was aimed at developing new methodologies, our approaches was to image excised coronary arteries under simulated *in-vivo* conditions in a tissue culture chamber. It is shown by this research that automatic plaque characterization techniques developed under *ex-vivo* conditions still apply for *in-vivo* studies. Based on this finding, an automatic plaque characterization technique using multicontrast MRI was developed. Furthermore, "shared k-space" reconstruction techniques were interrogated to assess their feasibility in accelerating multicontrast MRI acquisition. Results show that these techniques are promising in accelerating multicontrast MRI acquisitions.

Overall, the current thesis addresses: 1) the impact of plaque "freshness" on multicontrast MRI, 2) issues and solutions in automatic plaque characterization, 3) potential

schemes that accelerate multicontrast MR acquisitions.

CHAPTER I

INTRODUCTION

1.1 Introduction

Atherosclerosis, a systematic inflammatory disease, is the major contributor to cardiovascular disease [57, 62, 78], and affects 60 million people in the United States [1]. The identification of vulnerable atherosclerotic plaque and understanding of its formation appear to be crucial for the management and treatment of the clinical sequelae of atherosclerosis. Research [14, 34, 35] has shown that lumen size is not sufficient to predict the occurrence of clinical events. From a pathological point of view, information on plaque morphology and composition may be more valuable in the vulnerability assessment than lumen size. Driven by such clinical requirements, many imaging modalities have been investigated in atherosclerotic plaque characterization. These modalities include but are not limited to: intravascular ultrasound (IVUS) [69], optical coherence tomography (OCT) [44], ultra-fast electron beam coherence tomography (EBCT) [79] and magnetic resonance imaging (MRI) [93]. Excellent soft tissue contrast, abundant imaging mechanisms and non-invasive nature make MRI more promising than its peers [28] for this task. In Figure 1, images from the three most investigated plaque imaging modalities (CT, Ultrasound and MRI) illustrate MRI's priorities.

MR studies of atherosclerosis require the use of combined MR sequences to achieve the characterization goal [13, 27, 28, 30, 106, 109]. This new approach is known as multicontrast MRI of atherosclerotic plaque imaging.

1.2 Motivation

Multicontrast MRI is still in its developing phase [23, 28, 80, 107], and there are several problems yet to be solved. First of all, *in-vivo study of coronary plaques using MRI is still restricted by technical limitations.* Specifically, most previous research in MR coronary vessel wall imaging was performed under *ex-vivo* conditions. Secondly, *there is still no effective*

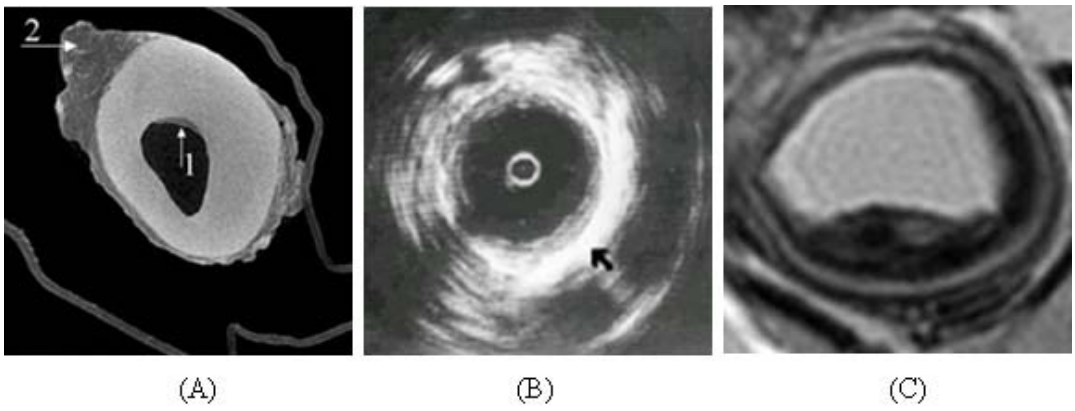

Figure 1: Comparison of plaque imaging modalities. (A) microCT [51], (B) intravascular ultrasound [82] and (C) high resolution T2 weighted MR images of atherosclerotic plaques. It can be seen that MRI possesses much better soft tissue contrast than CT and ultrasound.

means to automatically characterize plaque constituents. Thirdly, the number and type of MRI contrast mechanisms that should be used to inspect plaque's vulnerability are still unclear. In the original multicontrast MRI approach, three sequences are used (T1 weighted, T2 weighted and proton density weighted). Many successful supplements to the original technique have been added for better constituent differentiation. An example is Diffusion Weighted Imaging (DWI) that gives a more homogenous appearance of thrombus than other contrast mechanisms [95]. With more contrast mechanisms included in multicontrast MR imaging, *reducing acquisition time becomes more important than ever.*

1.3 The Problem Statement

What can we do to address the issues mentioned above and bring MR plaque imaging closer to clinical application? To answer the question, this thesis intends to develop a feasible and robust automated plaque characterization scheme based on multicontrast MR data; evaluate the feasibility of extending automated plaque characterization from *ex-vivo* to *in-vivo* scans; and explore possible means to accelerate multicontrast MRI acquisition.

Specifically, the goals of this thesis include:

1. Acquire multicontrast MRI in coronary atherosclerotic plaques under simulated *in-vivo* conditions.

(a) Design an MR scanner - compatible tissue culture system to maintain the physiological environment (and hence the MR properties of tissues) during acquisition.

(b) Evaluate and compare the multicontrast MRI results obtained from *fresh* and *preserved* stages using a histological gold standard.

(c) Measure the quantitative MR properties of plaque constituents at 4.7T under both *fresh* and *preserved* conditions.

2. Develop automatic characterization routines for plaque constituents using multicontrast MRI.

(a) Classify principal constituents in vulnerable atherosclerotic plaques using a Fuzzy C-Means (FCM) based clustering algorithm.

(b) Design a statistically based technique for labeling plaque constituents using quantitative MR properties.

(c) Develop an automatic plaque characterization routine.

3. Adapt "shared k-space" reconstruction methods in accelerating multicontrast MRI acquisitions.

(a) Adapt Keyhole and Reduced Imaging by Generalized-series Reconstruction (RIGR) techniques developed for dynamic imaging to the application of multicontrast MRI.

(b) Evaluate the performance of keyhole and RIGR reconstruction.

1.4 Approach

The title of this dissertation is "Multicontrast MRI of Atherosclerotic Plaques: Acquisition, Characterization and Reconstruction". The development of the thesis follows this sequence.

Firstly, essential physical and mathematical knowledge about the MR signal and image contrast was introduced. Image acquisition considerations including contrast mechanism selection, pulse sequence modification and vessel sample handling were then explained with

theoretical and empirical justifications. After all the theoretical analysis, multicontrast MR data were acquired with proper imaging protocol.

Secondly, the acquired multicontrast MRI data were employed to develop an automatic plaque characterization algorithm. Characterization, a pattern recognition task in image processing, was divided into two separate steps: classification/segmentation and labeling. The general approaches of classification were introduced briefly. For MR images, classification is further complicated due to practical issues such as partial volume effect and system imperfections. Therefore, modifications were introduced to the basic form of classification routine to improve its performance under such situations. To overcome the difficulties associated with traditional labeling practice, a novel labeling schemes was proposed. A new characterization algorithm, combining the proposed classification and labeling scheme, was then developed for plaque characterization. The data acquired previously were used to evaluate the performance of characterization.

Lastly, the dilemma of the contrast mechanism number and acquisition time was touched. Possible solutions to this issue were outlined. In the current thesis, efforts were addressed on the reconstruction side regarding the reduction of MR acquisition time. Specifically, "shared k-space" techniques were proposed for this purpose. The theoretical background of the techniques was detailed to justify their usage. The techniques were then evaluated on multicontrast MR data acquired on both research and clinical scanners.

1.5 Thesis Organization

The organization of the pages to follow closely adheres to the progression described above. Each chapter is essentially a stand-alone collection of related experiments targeted to achieve specific aims mentioned above.

Chapter II offers background information of atherosclerosis from a clinical, biological and technical standpoint. It covers key findings from biomedical science related investigations and gives an overview of the available biomedical imaging techniques of plaque characterization. It finally focused on the discussion of MRI's current role in plaque imaging, along with specific technical difficulties.

Chapter III touches the theoretical background of MRI's contrast mechanisms. It leads to a better understanding of multicontrast and quantitative MRI.

Chapter IV starts with the detailed description of MRI experiment setup and MRI acquisition protocol. The multicontrast MRI results of "fresh" and "preserved" vessels are then compared both qualitatively and quantitatively.

Chapter V aims at developing a fully automatic plaque characterization routine to assist the evaluation of the plaque vulnerability. The chapter starts with the classification/segmentation issue related to plaque characterization. Specific concerns of multicontrast MRI classification were introduced and solved while seeking a novel classification technique. Then, efforts were made on developing a tissue labeling scheme to tag the classification results. Finally, a novel characterization technique combining the classification and labeling was developed and evaluated on the MR data acquired in Chapter IV.

Chapter VI emphasizes the importance of reducing the MR acquisition time on the clinical practice of multicontrast MR plaque imaging. The theoretical background and implications of "shared k-space" reconstructions developed for dynamic imaging is first introduced. The techniques were then applied to multicontrast MR plaque imaging aiming at accelerating the MR acquisitions. Data reconstructed by the "shared k-space" techniques were finally evaluated to assess the feasibility of reducing imaging time using this type of reconstruction.

Chapter VII summarizes the major findings of the whole thesis, provides further research directions and concludes the thesis.

1.6 Scope of Document

It is presumed the reader has basic background with human physiology and MRI. Fundamental concepts including proton spin dynamics, electromagnetism, quantum mechanics - Schrödinger wavefunction, and MR image formation (Fourier theory) is used without detailed explanation. Some general MRI principles, especially those related to image contrast, are covered as they were discussed in each section. For more dedicated descriptions about

MRI physics, the reader is directed to reference books by Haacke et al. [39] and Vlaardingerbroek et al. [101]. The image formation theory and techniques for MRI are covered more thoroughly in the book by Liang and Lauterbur [55].

CHAPTER II

CLINICAL BACKGROUND AND LITERATURE REVIEW

2.1 Introduction

Healthy vessels of the human arterial tree, with few exceptions, are composed of three layers: the inner-most intima layer, the middle media layer and the outer-most adventitia layer. Atherosclerosis is a chronic, progressive disease characterized by the deposition of lipid and buildup of fibrous/necrotic tissues in the intimal layer of medium and large vessels [57, 62, 78]. It is a systemic inflammatory response to "injuries" resulting from lipoproteins and/or other risk factors. It is estimated that 50% of CVD, which is the leading cause of death and claims some 2600 deaths per day in the United States [1], is atherosclerosis related [62]. Despite the slow pace of its development, atherosclerosis often results in acute clinical manifestations, including ischemia, stroke and myocardial infarction.

According to traditional notion, bulky plaques may reduce blood flow, causing clinical symptoms. However, clinical data from serial angiographic studies demonstrate discontinuous increments for most atherosclerotic lesions [57]. This finding leads to the current concept that an acute occlusion results from formation of thrombus, accounting for more clinical complications than flow-limiting lesions [25, 62]. Indeed, evidence from clinical and animal research have proven that physical disruption of plaques may trigger thrombosis, and thus occlusion. Three types of physical disruptions are assumed [37]. The first type is superficial erosion, which comprises about 25% [37] to 40% [14, 32] of fatal thrombi. The second type is the disruption of intra-plaque micro-vessels, which leads to intra-plaque hemorrhage and sudden plaque progression. The last type is fibrous cap rupture and is the most common mechanism for plaque disruption and accounts for about 60% [14, 32] to 75% [37] of clinical events. It is also hypothesized that under many situations, cap rupture is "silent" and introduces no clinical outcomes. A consequence of these "silent" ruptures is that smooth muscle cell accumulation and collagen secretion can rapidly transform plaque lesions from

atheromatic to fibrotic. With the overwhelming clinical evidence, the prevailing wisdom is that lumen size itself is not sufficient to predict the vulnerability of atherosclerotic plaque.

2.2 Atherosclerotic Plaque

2.2.1 Plaque Formation

Generally speaking, atherosclerotic plaque is caused by the accumulation of lipid and fibrous elements in artery walls. Emerging evidence from bimolecular and pathology research suggests the formation of plaque is a series of inflammatory responses of the immune system triggered by the high concentration of low-density lipoprotein (LDL) in plasma [57, 62, 78].

According to the current notion, atherosclerotic plaques begin as intimal thickening, which may not necessarily be pathological. The thickened intima regions, however, are susceptible to the recruitment of lipid and development of atherosclerotic plaques. It has been shown that low wall shear stress plays immense role in lipid accumulation [33, 36, 49, 110]. During the initial stage of plaque progression, lipid pools form in the intimal layer. The continued deposition of lipid then increases the size of lipid pools and leads to the formation of a lipid-rich core. If inflammatory conditions prevail and risk factors persist, the lipid core may grow, and vessels take a compensatory response to maintain the lumen size and enlarge [34, 35]. At the same time, smooth muscle cells may migrate from the media to the intima and cause the proliferation of collagenous tissue. Usually, a fibrous cap is formed on the lumen side of the lipid core. Extracellular matrix degradation may occur, caused by proteinases. Moreover, pro-inflammatory cytokines such as interferon-g (IFN-g) may limit the synthesis of new collagen [57]. Both mechanisms render fibrous cap over the lipid core thinner and more susceptible to rupture. Rupture of the lipid core may be lethal or introduce new plaque constituents including: thrombus, intra-plaque thrombi and calcification.

2.2.2 Lesion Types and Plaque Vulnerability

Based on composition and morphological information, the American Heart Association published a series of papers describing the classification of atherosclerotic plaques [87, 88, 89]

Table 1: The Plaque Lesion Types Defined by American Heart Association

Lesion Types	Description	Histological Appearance
Type I	initial lesion	isolated macrophage foam cells
Type II	fatty streak lesion	intracellular lipid deposition
Type III	intermediate lesion	small extracellular lipid pools
Type IV	atheroma lesion	lipid core
Type V	fibroatheroma lesion	fibrotic cap over lipid core (may be multiple layers) or mainly fibrotic or mainly calcified
Type VI	complicated lesion	defect surface with hemorrhage and thrombus

†Subcategory of lesion types not listed.

based on composition and morphology. Briefly, plaques are classified into 6 types (Table 1).

More recently, Varmani et al [99], proposed a revised plaque characterization scheme based on the AHA definition, which facilitates the assessment of plaque vulnerability. In their report, atherosclerotic plaques are categorized as non-atherosclerotic intimal lesions; intimal thickening; intimal xanthoma (fatty streak); progressive atherosclerotic lesions; pathological intimal thickening (with or without erosion); fibrous cap atheroma (with or without erosion); thin cap atheroma; rupture plaque and fibrotic plaque. More detailed differentiation specifically for vulnerable atherosclerotic plaques has been done based on the knowledge from clinical and histological studies [66, 67, 68].

Vulnerable plaque is the type of plaque that triggers clinical manifestations, including transit ischemia attack, stroke and myocardium infarction. The classic model of vulnerable atherosclerotic plaque is thin cap atheroma (AHA Type IV) which can be identified by a bulky lipid core underlying a thin fibrous cap. Besides the rupture-prone thin cap atheroma, vulnerable plaques also may contain ruptured plaque with sub-occlusive thrombus; erosion-prone plaque; eroded plaque with sub-occlusive thrombus; plaque with intra-plaque hemorrhage; plaque with calcific nodule protruding into the vessel lumen or chronically stenotic plaque containing calcification and intra-plaque thrombi [67]. Schematic illustration of various vulnerable plaques is shown in Figure 2.

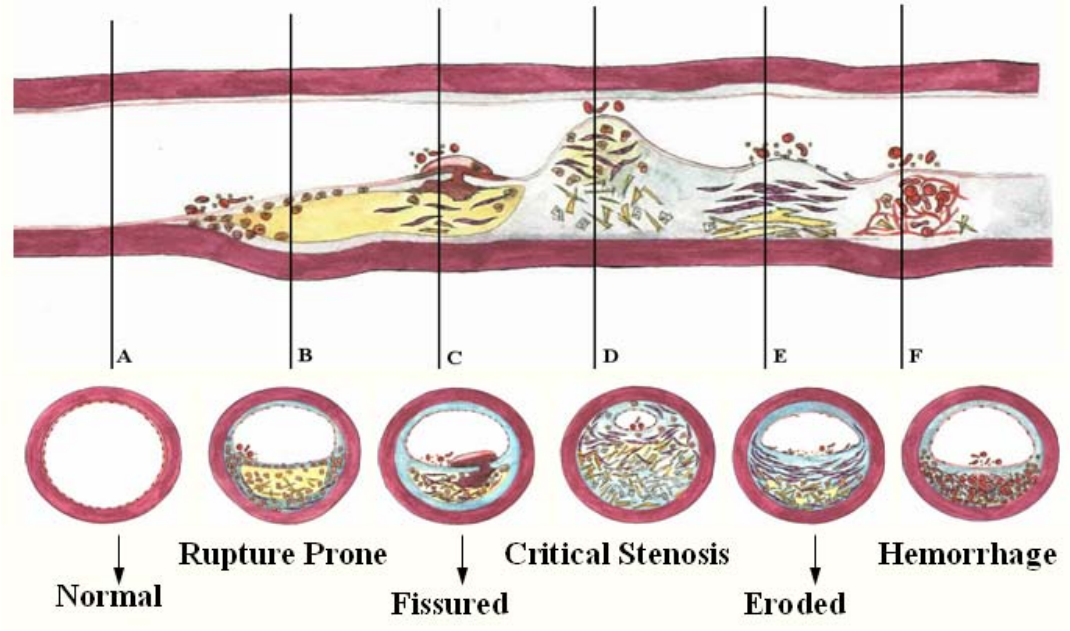

Figure 2: Vulnerable atherosclerotic plaques. Figure borrowed from www.vp.org.

It is clear from the above discussion that the vulnerability of atherosclerotic plaques is reflected by plaque composition and morphology. Generally speaking, all plaques of AHA type III and up can trigger clinical outcomes, and thus are vulnerable.

2.2.3 Plaque Constituents

Excluding adventitia, atherosclerotic vessels may contain the following tissue types: smooth muscle cells, collagen, proteoglycans, fibronectin elastic fibers, crystalline cholesterol, cholesteryl esters, phospholipids, T-lymphocytes, platelets, red blood cells and etc [56]. The plaque constituents composed of these tissues, according to plaque characterization nomenclature, are usually called intact media/intracellular matrix, dense to loose fibrous tissue, fibrous cap, lipid/necrotic core and intra-plaque/overlying thrombus.

The differentiation of fibrous tissue and fibrous cap is somewhat obscure. Generally speaking, the fibrous cap resides above a lipid core, whilst fibrous tissue appears elsewhere in the intima. Their constitutions, in most cases, also differ slightly. Fibrous caps usually contain more smooth muscle cells than fibrous tissue, and are often infiltrated by macrophages and lymphocytes [99].

2.3 Atherosclerosis and Medical Imaging

2.3.1 X-ray Angiography

Currently, the clinical standard screening technique for diagnosing atherosclerosis is X-ray angiography, which reveals the residual lumen size.

In X-ray angiography, residual lumen size is set as a measure for the vulnerability of atherosclerosis. When the lumen is 50%-70% occluded, it is considered to be an intermediate stenosis; when the occlusion is greater than 70 percent, it is considered to be a severe stenosis. X-ray angiography provides good resolution and contrast, however, it is an invasive technique. More importantly, as mentioned previously, lumen size is not always a proper criterion given the positive remodeling nature of atherosclerotic plaques [34, 35]. In the past decade, it has been shown that most plaques underlying a fatal or nonfatal myocardial infarctions are less than 70% stenosed [14]. For coronary artery atherosclerosis specifically, nearly 70 percent of clinical events are triggered by plaque rupture, and the other 30 percent can be attributed to thrombi formation due to the denudation of endothelial cells [99]. Research has shown that plaque producing non-flow-limiting stenoses account for more cases of plaque rupture and thrombosis than plaques producing a more severe stenosis [25]. As this was realized, researchers began to investigate plaque imaging techniques that focus on imaging atherosclerotic plaque itself.

To identify the morphology and composition of atherosclerotic plaques, many medical imaging modalities including intravascular ultrasound (IVUS), optical coherence tomography (OCT), angioscopy, near-infrared (NIR) spectroscopy, multi-slice computed tomography (CT), electron-beam computed tomography (EBCT), MRI, etc. have been investigated.

2.3.2 Intravascular Ultrasound

IVUS is a catheter-based, invasive technique based on transmitting and receiving high frequency ultrasonic signals to scan biological systems. In order to directly image a specific region of the artery, a catheter needs to be placed to the vicinity of the area. Because of the

fast imaging speed of ultrasound, this technique can provide real-time results. IVUS differentiates plaque components based on their differences in echogenicity. Typical atherosclerotic plaque can be differentiated into [69]:

1. Calcification, with high echoreflective regions with acoustic shadows.

2. Thrombus or lipid region, with hypoechoic regions.

3. Fibrous tissue, with hyperechoic regions.

The spatial resolution of this technique with the current generation catheter is about 100-250 μm. A major drawback, besides invasiveness, for this technique is the low sensitivity to detect lipid components in plaques [31].

IVUS elastography, a related technique, relies on the mechanical property differences between plaque tissues to differentiate them. This technique may provide better tissue differentiation based on the mechanical properties of plaque constituents [22]. However, there are still concerns in using this technique under a clinical setting.

2.3.3 Optical Coherence Tomography

OCT is similar, in theory, to IVUS except for the subsititution of ultrasound with infrared light. It possesses better signal-to-noise ratio (SNR) and resolution [44]. The reported resolution of OCT is as high as 10 μm. *In-vivo* studies of this technique prove its potential in characterizing major plaque components [44]. Despite the superiority in resolution and SNR to IVUS, this technique suffers invasiveness and poor penetration depth in tissue (1-2cm).

2.3.4 Electronic Beam CT

EBCT, multi-slice and spiral CT have been proposed by several researchers to inspect the plaque vulnerability. X-ray's inherent deficiency in soft tissue contrast, however, makes this technique insensitive to "soft" plaques. Therefore, calcium scores are usually calculated based on CT images and used as a biomarker for plaque vulnerability assessment [79].

Although calcification amount may not be a superior indicator compared to standard coronary risk factors, this method has its promise in detecting advanced coronary atherosclerosis for patients at intermediate risk [28].

2.3.5 Angioscopy and Near-Infrared Spectroscopy

Angioscopy utilizes an intravascular scope to directly inspect the surface of the vessel lumen. Research demonstrated the ability of this technique in visualizing ruptured plaque and mural thrombus on the lumen side of the plaque [96]. The clinical use of this technique is somewhat hindered by its invasiveness and the limitation of not being able to detect the inner layers of vessel walls.

In contrast to angioscopy, NIR has better tissue penetration and is suitable for inspecting the chemical composition of atherosclerotic plaques. It may be promising in assisting other interventional techniques for plaque vulnerability assessment.

2.4 MRI Plaque Imaging

Compared to the above techniques, MRI has superiorities for both its non-invasiveness and excellent soft tissue contrast. More importantly, MRI offers abundant image contrast mechanisms. For these reasons, MR plaque imaging has been an active research area for the past decade.

2.4.1 Brief Introduction of MRI

The intensity and contrast in MR images are controlled by the MR properties of tissues. For the vast majority of MR scanning, the signal source is the spinning protons in "water" [1]. To simplify the scenario, we can assume a single proton spinning inside the MR scanner. Since the proton is positively charged, the spinning introduces electric current. According to Maxwell's law, this current will introduce a small magnetic field perpendicular to the spinning plane. The outside magnetic field (B_0) produced by the scanner tends to force this small magnetic field to align with it. This is known as magnetization. In MR imaging, another excitation magnetic pulse (B_1) is utilized to deviate the small magnetization away

[1] The "water" here also includes lipid and other bio-molecules.

from the equilibrium position. As a consequence, the small magnetization starts to relax and finally realigns with B_0 (i.e., returning to equilibrium). The relaxation signal is picked up by the receiver coil of the MR system. It should be noted what is described here is from a classical mechanics viewpoint. In quantum mechanics, there are only two energy stages in which a proton can exist: parallel or anti-parallel. The magnetization is their macro statistics manifestation.

The MR signal's differences between two or more tissues give the image contrast. The underlying reason for signal differences is the difference in materials' MR properties, which include but not limited to proton density, T1, T2, apparent diffusion coefficient (ADC) and susceptibility. Proton density can be simply understood as how many protons (mainly in water) are present in a specific tissue. T1 is also called spin-lattice relaxation, which is a measure of how fast the excited magnetization recovers back to equilibrium. During relaxation, each spin loses energy to its nearby environment in this situation. T2 is also known as spin-spin relaxation, and is a measure of how quickly the excited magnetization disappears in the direction that perpendicular to B_0 (transverse). Each spin, under this situation, loses energy to its surrounding spins. ADC is a measure of the water molecules' Brownian motion in tissues. The diffusivity introduces additional magnetization relaxation via de-phasing. Susceptibility is related to the material's magnetization property (dia-, para- and ferro-magnetic). Functional MRI is an example that utilizes susceptibility to generate MR image contrast. In traditional spin echo and gradient echo sequences, the image contrast comes from a mixed effect of proton density, T1 and T2. In diffusion weighted imaging, diffusivity plays an additional role in image contrast. By specifically addressing one of the properties through manipulating imaging parameters, we can make the MR image weighted on this property (i.e., image contrast is predominately determined by this property). For instance, a T2 weighted image mainly reflects the T2 differences among tissues. The whole process of spin excitation and relaxation is governed by the Bloch equation:

$$d\vec{M}/dt = \vec{M} \times \gamma\vec{B} - (M_x\vec{i} + M_y\vec{j})/T2 - (M_z\vec{k} + {M_z}^0\vec{k})/T1 \quad (1)$$

Here, $\vec{M}$ is the magnetization; M_x, M_y, M_z are magnetization component along x, y

and z, respectively; $\vec{i}, \vec{j}$ and $\vec{k}$ are unit vectors; γ is the gyromagnetic ratio and $\vec{B}$ is the excitation magnetic field strength.

2.4.2 Introduction on MRI Plaque Imaging

Given that lipid core is a good biomarker in evaluating plaque vulnerability, early MR studies of atherosclerosis aim at characterizing the lipid signal from atherosclerotic plaques [3, 63, 98]. However, this approach has met with limited success because of poor image SNR. Indeed, Toussiant et al. [94] showed in a spectroscopic study that the lipid protons in a lipid core merely contribute less than 10% of the overall MR signal. What is even worse about this approach is that it may cause false positive diagnosis because lipid core is not the only component contributing to plaque vulnerability [99].

Because of these issues, T2 weighted MR images with much higher SNR were sought in order to better characterize plaques [93, 94]. It is shown by several studies [5, 77] that a quantitative T2 map is able to characterize major plaque constituents. Currently, most researchers agree that T2 weighting is the best single contrast mechanism for plaque characterization [80]. However, T2 weighted image alone fails to capture the subtle differences of some plaque constituents. For example, Serfaty et al. [81] demonstrated that a T2 weighted MR image alone was insufficient in identifying the size of lipid core.

The situation is ameliorated when multiple MR images with different contrast mechanisms are used to achieve the characterization goal [13, 27, 28, 30, 83, 102, 106, 109]. This approach is known as multicontrast MRI of atherosclerotic plaque imaging. The basic hypothesis of multicontrast MRI is that if two tissues share one similar MR property, e.g. T2, their other MR properties may be different and can be used to separate them. So, theoretically, the more contrast mechanisms used in multicontrast MRI, the more chance we have to characterize all plaque components. Based on this technique, improved plaque characterization can be achieved. Generally speaking, the contrast mechanisms involved in multicontrast MRI are spin echo/fast spin echo based proton density, T2 and T1 weighted imaging, which ensure high SNR and resolution of the acquired MR images. Other than these contrasts, magnetization transfer contrast (MTC) [70], diffusion weighted imaging

(DWI) [95] and chemical shift imaging (CSI) [93] were also interrogated for providing additional contrasts. Among these contrast mechanisms, DWI shows promise in assisting proton density, T2 and T1 weighted MRI to characterize plaques. It was noticed that DWI gives a much more homogenous appearance of thrombus than other contrast mechanisms [5, 95]. In addition, Clarke et al [17] reported that DWI offers excellent contrast between extracellular lipid core and other tissues.

Multicontrast MRI plaque imaging is still in a developing phase, and a major concern for most researchers in this field is how to make this technique clinically applicable. There is no standard clinical procedure as of now that utilizes multicontrast MRI alone to diagnose atherosclerosis. In the early stages of research, most MR studies were done *ex-vivo*. *In-vivo* studies were mainly focused on carotid plaques [13, 29, 93, 109] because of the relatively large size of the vessel, low motion effects, and superficial location. Although some progresses [10, 11, 26, 29, 48] has been made recently in coronary imaging, *in-vivo* coronary plaque characterization is still inapplicable because of the technical limitations. Some researchers achieved a resolution of about 400μm in *in-vivo* coronary plaque imaging, which is sufficient for identifying the wall volume and thickness, but insufficient to characterize plaque constituents. Coronary arteries are relatively small and have tortuous and unpredictable courses. The great motion introduced by cardiac and respiratory motion additionally complicates the problem. Therefore, our knowledge about multicontrast MRI of coronary atherosclerosis is still heavily dependent on *ex-vivo* studies. A major concern with such approaches is that the multicontrast MR image contrasts may be different compared to those under *in-vivo* conditions.

2.4.3 Image Processing for Tissue Characterization

Data analysis is another major difficulty associated with multicontrast MRI. Generally, manual segmentation and labeling are needed for plaque characterization. This approach needs expertise and is time-consuming. In addition, manual characterization usually subjects to inter and intra-observer biases.

Automatic plaque characterization may potentially mitigate these problems. Several

researchers have investigated the feasibility and assessed the performance of a variety of automatic plaque characterization techniques [2, 16, 17, 43, 61, 105]. Most of the proposed methods are based on *ex-vivo* data [2, 16, 17, 43, 105].

Generally, characterization techniques can be roughly divided into two categories: edge-based [2, 105] and intensity-based [2, 16, 17, 43, 61] approaches. Edge-based methods separate different tissues relying on the images' discontinuity (edge); intensity-based techniques group segments of the same tissue based on their intensity similarity. In this sense, the edge-based techniques actually incorporate more information (both intensity and spatial) than intensity-based techniques (only intensity). This fact generally endows edge-based techniques with better performance in segmentation tasks. However, when it comes to characterization, edge-based techniques usually need considerable operator interaction especially for multicontrast MRI. For this reason, edge-based techniques were only investigated on single MR images characterization [105] or applied to detect the boundaries of vessel walls [2].

The intensity-based techniques can be further divided into two sub-categories: supervised [16, 17, 61] and unsupervised [2, 43] approaches. The supervised method needs training of the classifier prior to the classification, i.e., the operator has to teach the classifier prior to classification what intensity (or other properties) a specific tissue type should possess. For MRI, the training is not "universal". Each time the imaging parameters and/or scanner change, the classifier has to be re-trained. Unsupervised techniques, on the other hand, learn by themselves the common intensity (or other properties) that each type of tissue should possess, and therefore it is more robust. Because only intensity information is utilized in traditional intensity-based techniques, these methods are usually very sensitive to intensity variations introduced by noise, field inhomogeneity, partial volume effects (PVE), etc. This problem can be mitigated by including spatial information into the classification process [43, 58, 59, 60, 73, 103].

Following a similar approach as manual plaque characterization, the vast majority of automated plaque characterization techniques separate plaque constituents based on the

comparative contrasts of MR images of each contrast mechanism. The comparative contrasts are usually summarized as intensity tables [2, 27, 30, 43, 83], which are used to differentiate plaque tissues.

It should be noted that characterization is different from classification, at least under the scope of this thesis. To avoid misunderstanding, we should clarify the notions of classification and characterization here. Classification is defined as multiple tissue segmentation (the simplest case is two tissue segmentation), and characterization is defined as the combination of classification and labeling. In other words, classification serves the purpose of differentiating different constituents, whilst characterization involves both differentiating tissue constituents and tagging classification results according to each tissue's specific characteristics.

For manual plaque characterization, the labeling is performed based on specific intensity patterns (intensity table) for each plaque constituent manifested in multicontrast MR images. However, these patterns may alter due to change of imaging parameters. Comparatively, the tissue MR properties, including T1 (spin-lattice) relaxation time, T2 (spin-spin) relaxation time, proton density and ADC, may potentially be a more consistent measure in plaque constituents labeling since they are tissue type independent and only rely on temperature and field strength.

2.5 Contrast Mechanism vs. Acquisition Time

It is always desirable to have more contrast mechanisms when practicing atherosclerotic plaque characterization since more information helps better in separating the plaque components. Clark et al. [17] used eight contrast mechanisms including proton density, T2, and T1 weighted fast spin echo, steady-state acquisition, T1 weighted spoiled gradient-echo with and without magnetization transfer, and diffusion weighted spin echo sequences to automatically characterize plaque constituents.

Despite the apparent advantage, it is impractical to include too many contrast mechanisms under clinical settings due to the lengthy acquisition needed. Moreover, too many contrast mechanisms impose additional difficulty on registering MR images. Because of the

high resolution and SNR required to characterize plaque constituents, fast imaging techniques such as echo planar imaging, fast gradient echo and fast imaging with steady state precession (FISP) are not suitable for reducing the acquisition time. In other words, viable fast imaging schemes should not sacrifice image resolution and SNR in multicontrast MRI.

2.6 Conclusion

In this chapter, we reviewed the clinical aspects of atherosclerosis and point out the need of identifying vulnerable plaques in order to prospectively assess the risk of clinical events. Many clinical tests including C-Reactive Protein (CRP) test, CT angiography and IVUS are currently available to predicate the vulnerability of atherosclerosis. Emerging clinical evidence indicates that the plaque constituents and morphology could provide more accurate predication about clinical risk. A new technique, called multicontrast MRI, is promising in characterizing atherosclerotic plaques and assessing their vulnerability. There are still some technical difficulties associated with this approach, which challenge its application under clinical settings. In addition, the time cost of multiple scans in multicontrast MRI has not been addressed. Moreover, due to the fact that most multicontrast MRI studies on coronary plaques were conducted on excised vessel specimens, systematic evaluation of vessel "freshness" on multicontrast MRI results needs to be performed to avoid potential pitfalls.

CHAPTER III

FUNDAMENTALS OF MR PHYSICS AND IMAGE CONTRAST

3.1 Introduction

In this section, the commonly known mathematical formulations of MR signal expression will be introduced. This outline of MR physics serves as theoretical background to better understand the contrast in MRI. Moreover, it provides insights about tissues' quantitative properties including T1, T2, proton density as well as diffusivity.

3.2 The Basics of MR Signal and Pulse Sequences

Generally speaking, magnetic resonance imaging focuses on detecting the magnetoelectrical signal from the unpaired protons. The spinning of a proton gives rise to a small magnetization. Under normal situations, the magnetization has no preferred directions and thus the bulk magnetization manifested is zero. However, when an outside magnetic field is present, slightly more magnetizations tend to algin with the outside field because it is a low energy configuration. As a result, a bulk magnetization parallel to the outside magnetic field is generated. Under this classic model, it can be shown that once the bulk magnetization deviates from the outside magnetic field direction, a torque will be imposed to the magnetization and cause it to precess around the outside magnetic field. As mentioned earlier, the outside magnetic field is usually known as B_0. The frequency of the precession is usually known as the lamor frequency and can be calculated as $w = \gamma B_0$, where γ is the gyromagnetic ratio.

One of the fundamental theories that MRI relies on is magnetic resonance, which indicates that the magnetization will be nutated (deviate from the outside magnetic field while doing precession) away from the outside magnetic field by an additional magnetic field, B_1, that has the same frequency (resonance) as the lamor frequency. In quantum mechanics, there are only two energy configurations for precessing protons: parallel and anti-parallel. Specific quantum energy, determined by the lamor frequency, is needed to allow the configuration change for proton precession. Classically, this property is easily understood under

the framework of a rotating coordinate system. If the rotational frequency of this system is equal to lamor frequency, the internal magnetization will be stationary in this reference system. If B_1 is precessing at the same frequency, it is also stationary in the reference coordination. Under this framework, the torque on the magnetization imposed by B_1 is constant and keeps on flipping the magnetization. Otherwise, its effect will be canceled out after integration over time. Since the lamor frequency is at radio frequency range for protons under the operational magnetic field of MRI systems, the B_1 is usually known as an RF pulse.

The Bloch equation (Eq. (1)) introduced in the last chapter is the central law governing magnetic resonance signals. It contains two parts: excitation and relaxation. The excitation part of Bloch equation is the first term on the right hand side. Usually, the excitation process is very quick so that the relaxation during this period can be ignored. To simplify the Bloch equation, the vector form of magnetization is usually decomposed to the orthogonal coordinates. Accordingly, the Bloch equation is usually expressed in matrix form. The matrix expression of Bloch equation without relaxation is shown in Equation (2). The prime is used to indicate that it is in the rotating coordinating system.

$$\begin{bmatrix} d\vec{M}_{x'}/dt \\ d\vec{M}_{y'}/dt \\ d\vec{M}_{z'}/dt \end{bmatrix} = \begin{bmatrix} 0 & 0 & -\gamma B_{1y'} \\ 0 & 0 & \gamma B_{1x'} \\ \gamma B_{1y'} & -\gamma B_{1x'} & 0 \end{bmatrix} \begin{bmatrix} d\vec{M}_{x'} \\ d\vec{M}_{y'} \\ d\vec{M}_{z'} \end{bmatrix} \tag{2}$$

MRI systems rely on coils (RCL circuits) to transmit RF pulses and detect the MR signals (proportional to magnetization). In order to explain the contrasts of MR images, relaxation needs to be introduced. Generally speaking, relaxation is the process that the deviated magnetization, nutated by B_1, returns to equilibrium (alignment with the outside magnetic field). Basically, there are two factors contributing to the relaxation of the magnetization: spin-lattice relaxation and spin-lattice relaxation. The spin-lattice relaxation is usually called T1 relaxation, and it is a measure of how the longitudinal magnetization ($\vec{M}_z$) regrows back to its equilibrium value ($\vec{M}_0$). The spin-spin relaxation, also known as T2 relaxation, describes how fast the transverse magnetization ($\vec{M}_T = \vec{M}_x + i\vec{M}_y$) disappears.

All the factors that contribute to T1 relaxation equally affect T2 relaxation. Therefore, T2 is always smaller than T1. Details about the relaxation can be referred to the BPP theory proposed by Bloembergen, Purcell and Pound [9]. Including relaxation in Equation (2), the Bloch equation then can be reformulated to Equation (3).

$$\begin{bmatrix} d\vec{M}_{x'}/dt \\ d\vec{M}_{y'}/dt \\ d\vec{M}_{z'}/dt \end{bmatrix} = \begin{bmatrix} -1/T2 & 0 & -\gamma B_{1y'} \\ 0 & -1/T2 & \gamma B_{1x'} \\ \gamma B_{1y'} & -\gamma B_{1x'} & -1/T1 \end{bmatrix} \begin{bmatrix} d\vec{M}_{x'} \\ d\vec{M}_{y'} \\ d\vec{M}_{z'} \end{bmatrix} + \begin{bmatrix} 0 \\ 0 \\ d\vec{M}_0/T1 \end{bmatrix} \tag{3}$$

If the above Bloch equation is applied to several homogenous materials, the signal will be different for different materials because of their characteristic equilibrium magnetizations (proportional to proton density), T1 and T2 values. In other words, the contrast of MR images is contributed by the tissue's characteristic MR properties, including but not restricted to, T1, T2 and proton density. The amount of contribution of each MR property can be controlled by the MR pulse sequence and will be explained in more detail later in this chapter.

Before providing the description of MRI pulse sequence, the issue of signal localization has to be resolved. So far, we have been focusing on homogenous tissues. In order to image mixtures of tissues in biological systems, there has to be a way to localize the signal. The first successful method for signal localization, know as zeugmatography, was presented by Nobel laureate Dr. Lauterbur in 1973 [52]. In this novel paper, the idea of using gradients to create differences between spatial locations led to the modern technique of magnetic resonance imaging. This process is usually called spatial encoding. As a general statement, a gradient field is needed for all the dimensions whose spatial location is to be resolved. For instance, gradients are needed along the three axes for three dimensional cartesian MR imaging.

Theoretically, spatial encoding can be easily understood from fundamental signal processing principles. Assuming a biological system can be divided into voxels of equal sizes, each voxel can be expressed using its cartesian coordinates (x, y, z). If there are gradients (G_x, G_y, G_z) applied during time T_{start} and time T_{end}, the complex transverse magnetization

can be expressed as:

$$M_T(x,y,z)e^{-j\gamma\int_{T_{start}}^{T_{end}}(G_x\cdot x+G_y\cdot y+G_z\cdot z)dt}e^{-j\gamma B_0 T_{end}} \tag{4}$$

Since the last exponential is solely caused by lamor precession, it can be dropped in the rotating frame, and the complex signal can be simplified as:

$$M_T(x,y,z)e^{-j\gamma\int_{T_{start}}^{T_{end}}(G_x\cdot x+G_y\cdot y+G_z\cdot z)dt} \tag{5}$$

The presence of the gradients essentially causes the differences in lamor frequency inside the biological systems depending on the spatial location. If the gradients are constant for all the spatial locations, the mixed signal MR coil detected is proportional to the signal integral of all the voxels assuming the size of each voxel is (dx, dy, dz). It is formulated as Equation (6).

$$S=\int_X\int_Y\int_Z M_T(x,y,z)e^{-j\gamma\int_{T_{start}}^{T_{end}}(G_x\cdot x+G_y\cdot y+G_z\cdot z)dt}dxdydz \tag{6}$$

Equation (6) can be simplified to (7) by substituting $\gamma\!\!\!^{-}\int_{T_{start}}^{T_{end}} G_x dt$, $\gamma\!\!\!^{-}\int_{T_{start}}^{T_{end}} G_y dt$ and $\gamma\!\!\!^{-}\int_{T_{start}}^{T_{end}} G_z dt$ with k_x, k_y and k_z. Here, $\gamma\!\!\!^{-}$ equals $\gamma/2\pi$.

$$S(k_x,k_y,k_z)=\int_X\int_Y\int_Z M_T(x,y,z)e^{-2\pi j(k_x\cdot x+k_y\cdot y+k_z\cdot z)dt}dxdydz \tag{7}$$

It is a boon to MRI that Equation (7) demonstrated that the magnetization, $M_T(x,y,z)$, and the acquired signal, $S(k_x,k_y,k_z)$, is a Fourier pair. From a signal processing point of view, the acquired data are in the frequency space. In MR physics, this space is usually called k-space. Basic Fourier theory indicates that a biological system can be represented by $N\times M\times L$ voxels after an inverse Fourier transform of $N\times M\times L$ evenly distributed k-space data. From the above discussion, it is apparent that in order to gather these evenly distributed points in k-space, multiple acquisitions with different gradients integral (magnitude or duration) are needed. The combination of RF pulses and gradient fields associated with appropriate timing, known as pulse sequence diagram (PSD), is used to collect the k-space data. For technical details about MR pulse sequences, the readers are referred to books by Vlaardingerbroek [100], Haacke [39] and Bernstein [6]. A simple two

dimensional spin echo PSD is illustrated in Figure 3. Spin echo and its variant sequences are the workhorse of clinical MR imaging for their comparative high SNR. Throughout this dissertation, most of the imaging sequences are spin echo based. Therefore, important aspects of this type of sequence will be covered in the following discussion.

In MRI, relaxation is not the only contributor to signal decay. Both gradients and magnetic field inhomogeneity cause magnetizations at different spatial locations to precess at different frequency, which additionally complicates the MR signal. Fortunately, none of these effects is irreversible. For most cases, gradients are essential for MR signal localization (see above description). There are situations, however, when the gradient effect needs to be reversed. For example, in Figure 3, the slice selective gradient for the 90 degree pulse is associated with negative polarity gradient to cancel out the de-phasing effect. Technically, the effect of a specific gradient can be canceled by forcing the integral of this gradient to be zero at the time of signal acquisition. This treatment makes the phases at different locations identical [1], thus maximizing the signal (gradient echo). Field inhomogeneity, on the other hand, is always undesirable for imaging. Therefore, its effect needs to be minimized to avoid signal loss and image artifacts. The easiest treatment for this issue is to acquire signal as soon as the magnetization is flipped. This ensures that the magnetization signal decay due to field inhomogeneity is minimal. Another treatment is the spin echo (Hahn echo) technique. Spin echo technique relies on the administration of two RF pulses - a 90 degree pulse and a 180 degree pulse. To understand the technique, two magnetizations under different fields can be considered. After the first 90 degree pulse, both magnetizations are flipped into the transverse plane. Because of the difference in magnetic field strength, these two magnetizations precess at different frequency and lose phase. Assuming the phases are ϕ and φ for the faster and slower magnetizations after a period of $TE/2$, respectively, the second 180 degree pulse will reverse the phase. That is, after the 180 degree pulse, the phases become $-\phi$ and $-\varphi$ for the faster and slower magnetizations, respectively. After another $TE/2$, both magnetizations have zero phase and the signal (spin echo) is maximized. TE is usually called echo time in MRI.

[1] Assuming the outside magnetic field is perfectly homogenous.

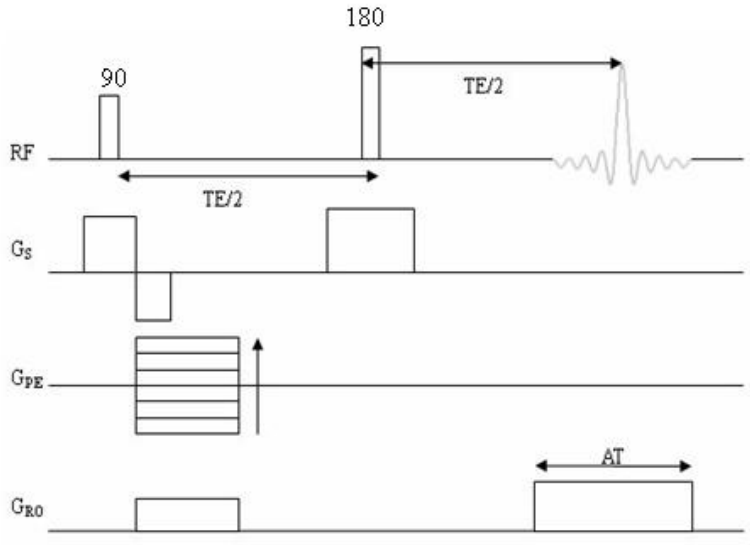

Figure 3: Spin echo pulse sequence diagram. RF is the radio frequency electromagnetic pulse. G_{ss} is the slice selective gradient - for a 90 degree pulse, a specific slice is selected based on the frequency range rendered by the G_{ss}. this gradient introduced gradient dephasing and must be refocused using a gradient with negative polarity. For 180 degree pulse, the slice selective gradient is non-selective (gradient is actually off). Therefore, no refocusing gradient is needed. G_{PE} is the phase encoding gradient, and for each repetition time, TR, the gradient is increased by a constant amount (arrow shows the direction). G_{RO} is the readout gradient. The portion before 180 degree pulse is the read refocusing pulse, whose area is half of the portion after 180 degree pulse. This ensures the frequency space along the readout direction is sampled symmetrically around zero. The signal is acquired during the acquisition time, AT, with an Analog-to-Digital converter (ADC).

In order to cover the k-space for MRI reconstruction, the pulse sequences (e.g., Figure 3) need to be run multiple times. The duration for each run is called repetition time or TR. For better understanding of MR PSD, the k-space trajectory (coverage scheme) needs to be mentioned. Taking Figure 3 as an example, its corresponding k-space trajectory is shown in Figure 4. K_{RO} is incremented with the increment of time (during that acquisition time, AT, of G_{RO}), while K_{PE} is incremented through the increment of phase encoding gradient, G_{PE}. For each TR, a specific line of K_{RO} is acquired. Therefore, if N lines is needed along the K_{PE} direction, this specific pulse sequence needs to be repeated for N times.

The presence of gradients changes the MRI signal. This change is reflected in the Bloch equation shown in Equation (8), where $\vec{r}$ is the direction unit vector.

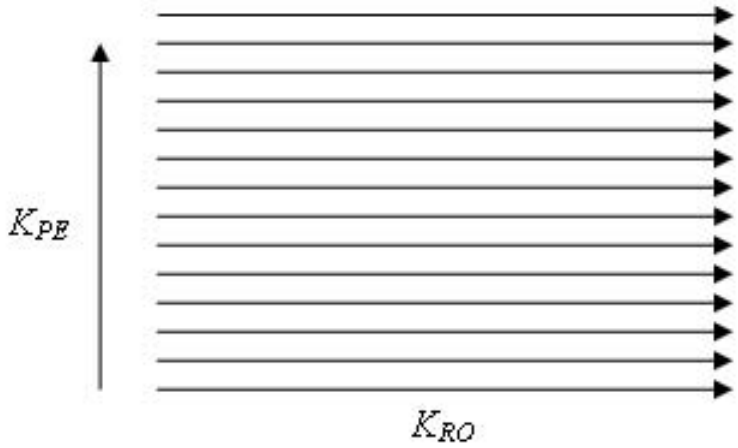

Figure 4: K-space trajectory corresponding to the PSD of Figure 4. K_{PE} is along the phase encoding direction and K is along the readout direction.

$$\begin{bmatrix} d\vec{M}_{x'}/dt \\ d\vec{M}_{y'}/dt \\ d\vec{M}_{z'}/dt \end{bmatrix} = \begin{bmatrix} -1/T2 & \vec{G}\cdot\vec{r} & -\gamma B_{1y'} \\ -\vec{G}\cdot\vec{r} & -1/T2 & \gamma B_{1x'} \\ \gamma B_{1y'} & -\gamma B_{1x'} & -1/T1 \end{bmatrix} \begin{bmatrix} d\vec{M}_{x'} \\ d\vec{M}_{y'} \\ d\vec{M}_{z'} \end{bmatrix} + \begin{bmatrix} 0 \\ 0 \\ d\vec{M}_0/T1 \end{bmatrix} \tag{8}$$

Without detailed mathematical derivation, the analytical solution of the Bloch equation in the image domain under the spin echo PSD framework is shown in Equation (9). In this equation, $S(x, y, z)$ is used to symbolize the signal intensity at location (x, y, z) in the spatial domain; $M(\rho(x, y, z), T, B_0)$ is the magnetization that is determined by proton density $\rho(x, y, z)$, temperature T and external magnetic field B_0.

$$S(x, y, z) \propto M(\rho(x, y, z), T, B_0)(1 - 2e^{-(TR-TE/2)/T1} + e^{-TR/T1})e^{-TE/T2} \tag{9}$$

In spin echo based sequences, TR is usually much greater than TE. Therefore, Equation (9) is usually simplified as Equation (10).

$$S(x, y, z) \propto M(\rho(x, y, z), T, B_0)(1 - e^{-TR/T1})e^{-TE/T2} \tag{10}$$

Equation (10) provides the fundamental basis in understanding MRI contrast mechanism. In cases of large TR and TE, the RHS of Equation (10) can be approximated by

$M(\rho(x,y,z),T,B_0)e^{-TE/T2}$. Therefore, T2 becomes the dominant factor contributing to the signal and the image contrast is said to be T2 weighted. When TR is large and TE is small, on the other hand, the RHS of Equation (10) approximates to $M(\rho(x,y,z),T,B_0)$. Under this situation, the image contrast will be predominately determined by proton density (proton density weighted). The last configuration is when both TR and TE are small. Under this setting, the RHS of Equation (10) approximates to $M(\rho(x,y,z),T,B_0)(1-e^{-TR/T1})$, and thus the image contrast is T1 weighted.

Besides these three basic contrast mechanisms, pulse sequences can be designed to reflect other MR properties that can separate plaque tissues. For plaque imaging, an additional MR property besides T1, T2 and proton density is water diffusivity. Studies [5, 95] show that water diffusivity may be critical in characterizing the mural or intra-plaque thrombus. The reason that water diffusivity will affect the MRI signal is because of the local variation of the magnetic field. Even if the magnetic field is perfectly uniform, there are variations at the molecular level because of chemical environment differences from location to location. Part of the effect from magnetic field variation is irreversible because of the Brownian motion of water molecules (protons). Signal from a specific proton can be refocused with a spin echo sequence if it builds up the same amount of phase during the de-phasing and rephasing period. This is generally not true for protons with motion. This effect can be exaggerated by adding diffusion gradients in the PSD (Figure 5). It should be noted that the diffusion gradients have directionality. In Figure 5, only diffusion along the slice selected direction is sensitized.

With the diffusion gradients, an additional exponential decay is added to Equation (10) to yield Equation (11), where D is water diffusivity; G_d is the pulse field gradient; Δ and δ are the diffusion time and duration of the pulse gradient, respectively. Usually, $\gamma^2 G_d^2 \delta^2(\Delta - \delta/3)$ is replaced by b to simplify the equation.

$$S(x,y,z) \propto M(\rho(x,y,z),T,B_0)(1-e^{-TR/T1})e^{-TE/T2}e^{-\gamma^2 G_d^2 \delta^2(\Delta-\delta/3)D} \tag{11}$$

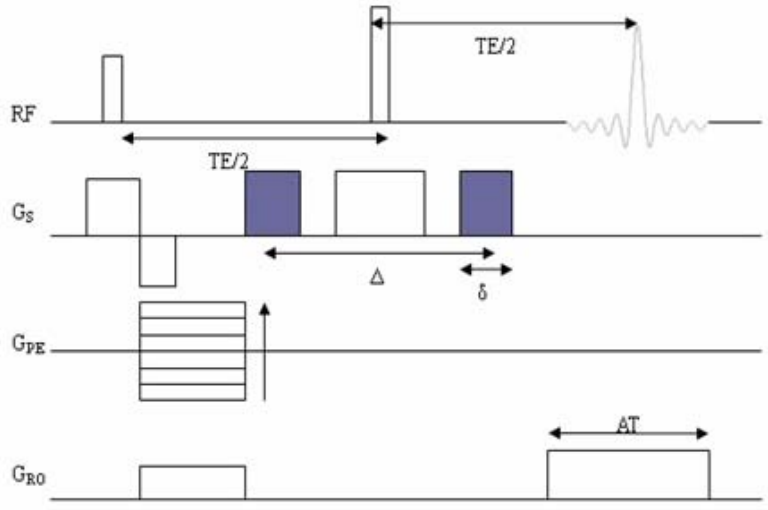

Figure 5: Spin echo pulse sequence diagram with diffusion gradient. The purple area shows the diffusion gradients. Δ is the diffusion time and δ is the diffusion gradient time.

3.3 Quantitative MRI

From the above discussion, it has can be seen that the contrast of MR images is controlled by several MR properties. Under certain situations, it is desired to separate these effects. This task can be accomplished by fitting the MR signal according to an expected model and re-synthesizing fitting parameters into quantitative maps, which are also known as quantitative MRI.

The basic idea of quantitative MRI computation is not complicated, although it may be a different story for sequence design and map computation. For spin echo based sequences, fortunately, both the acquisition scheme and map calculation is comparatively easy. For simplicity, we can assume the PSD of Figure 5 and its corresponding signal expression of Equation (12) [2]. Overall, there are four unknowns for this equation: $M(\rho(x, y, z), T, B_0)$ (proton density), T1, T2 and diffusivity (D). Theoretically, we only need four equations, or equivalently four combinations of TR and TE, to calculate these values. In practice, however, least squares are usually applied to over-determined equation matrix for better accuracy. For instance, in computing quantitative T2 maps, multiple (≥ 2) TE values were

[2] b equals zero without diffusion gradients.

selected with a fixed TR and b values. Under this situation, the signal equation can be simplified as Equation (13). The T2 value of plaque components can then be calculated by fitting the pixel intensities on these images to an exponential decay. The fitting process can be further simplified by taking a logarithm transformation of the equation. This results in a linear fit of Equation (14).

$$S(x,y,z) \propto M(\rho(x,y,z),T,B_0)(1-e^{-TR/T1})e^{-TE/T2}e^{-bD} \tag{12}$$

$$S(x,y,z) \propto Constant \cdot e^{-TE/T2} \tag{13}$$

$$ln(S(x,y,z)) \propto ln(Constant) - TE/T2 \tag{14}$$

In a similar manner, diffusivity can be computed by fixing the TR and TE values while varying the b value. The T1 value can be calculated by fixing TE and b. Nonlinear fitting has to be performed for T1 calculation since the equation can not be linearized.

3.4 Pulse Sequence Modification for Quantitative MRI

As seen in previous discussions, the diffusion gradients render the MR image contrast diffusion weighted. Without these gradients, there are still small contributions from water diffusion to MR image contrast because of the interactions between other imaging gradients (e.g., the read refocusing and readout gradients behave as a pair of diffusion gradients). In traditional spin echo and turbo spin echo sequences, this additional diffusion effect is shown to be dependent on the echo time, TE. Specifically, without any derivation, Equation (10) should be replaced with the more accurate expression: Equation (15).

$$S(x,y,z) \propto M(\rho(x,y,z),T,B_0)(1-e^{-TR/T1})e^{-TE/T2}e^{-\gamma^2 {G_r}^2 (AT/2)^2 (TE-AT/6)D} \tag{15}$$

In this equation, ${G_r}^2$ is the magnitude of the readout gradient. For high resolution acquisitions, since ${G_r}^2$ is usually high, the effect of this unwanted diffusion becomes greater. Because of the unwanted diffusion, the measured quantitative T2 values differ from their

real values. Under this situation, the calculated T2 value can be expressed by the following Equation (16).

$$1/T2_{cal} = 1/T2_{real} + \gamma^2 {G_r}^2 (AT/2)^2 D \tag{16}$$

In the current study, accurate measurements of tissues' T2 values are important in evaluating multicontrast MRI and characterizing plaque components. Therefore, to better estimate the quantitative T2 values, the traditional spin echo sequence was modified by moving the phase encoding and read refocusing gradients from prior to the 180 degree RF pulse to after it [65]. With this modification, the diffusion effect introduced by imaging gradients is no longer dependent on TE. Therefore, the additional diffusion term becomes a constant during the T2 computation, and thus has no effect on the calculated T2 value.

To evaluate its performance, we compared the measured T2 values of Medium 199 tissue culture solution using traditional and revised sequences. The T2 value (T = 20°C) calculated using the spectroscopic Carr-Purcell-Meiboom-Gill (CPMG) sequence was $823ms$ and was set as the gold standard. The T2 values calculated using traditional and modified SE imaging sequences were $128ms$ and $798ms$, respectively. It can be seen that the modified sequence gives a much better T2 estimation. Another advantage in using this sequence is the SNR improvement due to reduced diffusion interference. Figure (6) shows the PSD of this modification.

For diffusion weighted sequences, the diffusion gradients are usually regarded as the only contributor to diffusion contrast. This assumption, however, is only an approximation. There are interactions between imaging and diffusion gradients that cause additional diffusion during the MR acquisition as previously mentioned. This is known as "cross term effect", and it causes inaccuracy in ADC measurement. To better understand the "cross term effect", it is beneficial to examine the signal equation of DWI (Eq. (17)).

$$S = S(0) e^{-D \int (\int_0^t G(\tau) d\tau)^2 dt} \tag{17}$$

In this equation, $S(0)$ is the MR signal without diffusion. If gradient G is broken into

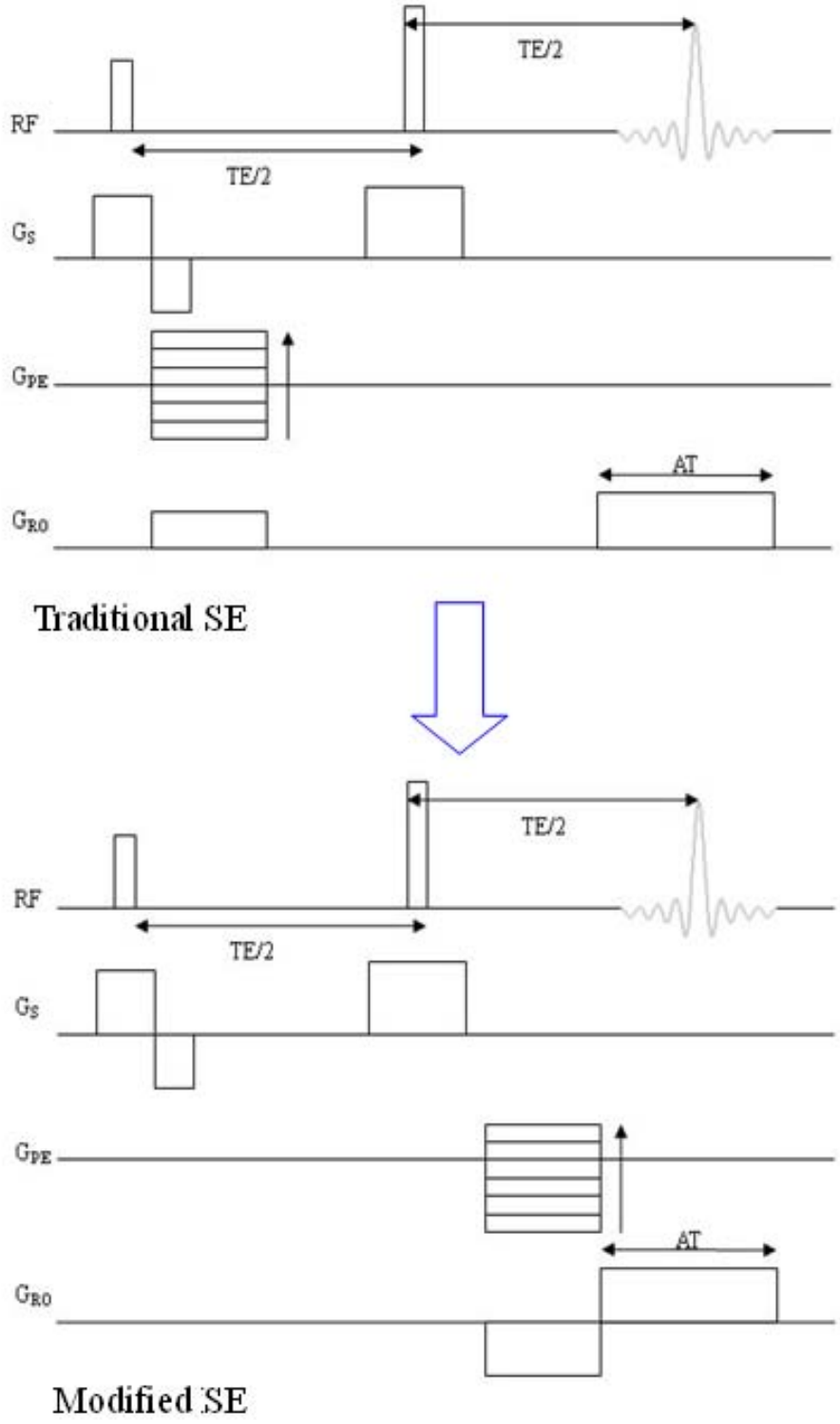

Figure 6: Traditional(upper) and modified(lower) spin echo sequences. The modified sequence minimized the effect from unwanted water diffusion caused by the integrations from imaging gradients.

an imaging gradient G_i and a diffusion gradient G_d, the equation is reformulated as:

$$S = S(0)e^{-D\int(\int_0^t G_i(\tau)d\tau+\int_0^t G_d(\tau)d)^2dt} \tag{18}$$

Additionally, if we replace $\int_0^t G_i(\tau)d\tau$ with f_i and $\int_0^t G_d(\tau)d\tau$ with f_d, this equation is simplified as:

$$S = S(0)e^{-D\int(f_i+f_d)^2dt} = S(0)e^{-D\int(f_i^2+2f_if_d+f_d^2)dt} \tag{19}$$

From this equation, it can be seen, when changing f_d in calculating D, the "cross term", f_if_d, changes as well despite f_i remaining constant. As a consequence, the measured water diffusion coefficients employing this sequence deviate from their physical values. Based on the scheme proposed by Hong et al. [42], a modified diffusion weighted spin echo sequence is used in the current study for quantitative measurement of the plaque components' diffusivities. In this modified scheme, each lobe of the diffusion gradients is replaced with a bipolar gradient pair. This treatment ensures that the cross term effect is canceled. Detailed mathematical justification of this scheme can be found in reference [42]. In Figure (7), both the traditional and modified diffusion weighted sequence are shown. The corresponding f_i, f_{id} and f_if_d are shown in Figure (8). It can be seen that in the modified DWI sequence (Fig. 8(B)), the "cross term effect" integrates to zero at the time of signal sampling, and thus has no effect on ADC calculation.

The ADC value (T = 20°C) of water calculated applying this revised sequence was $2.5\times 10^5 cm^2/s$ in all three orientations (phase encoding, slice selective and readout directions). The traditional sequence, however, gave different ADC values for different orientations. The reference value of water ADC value was calculated as follows:

1. Calculate ADC(1) by using DWI images with gradient 0, +g1, +g2, +g3 ...
2. Calculate ADC(2) by using DWI images with gradient 0, -g1, -g2, -g3 ...
3. The ADC value is the geometric mean of ADC(1) and ADC(2).

This technique cancels out the "cross term" but requires twice the acquisition time. The water's ADC value using this method was $2.5 \times 10^5 cm^2/s$ as well, which validated the performance of our modified sequence.

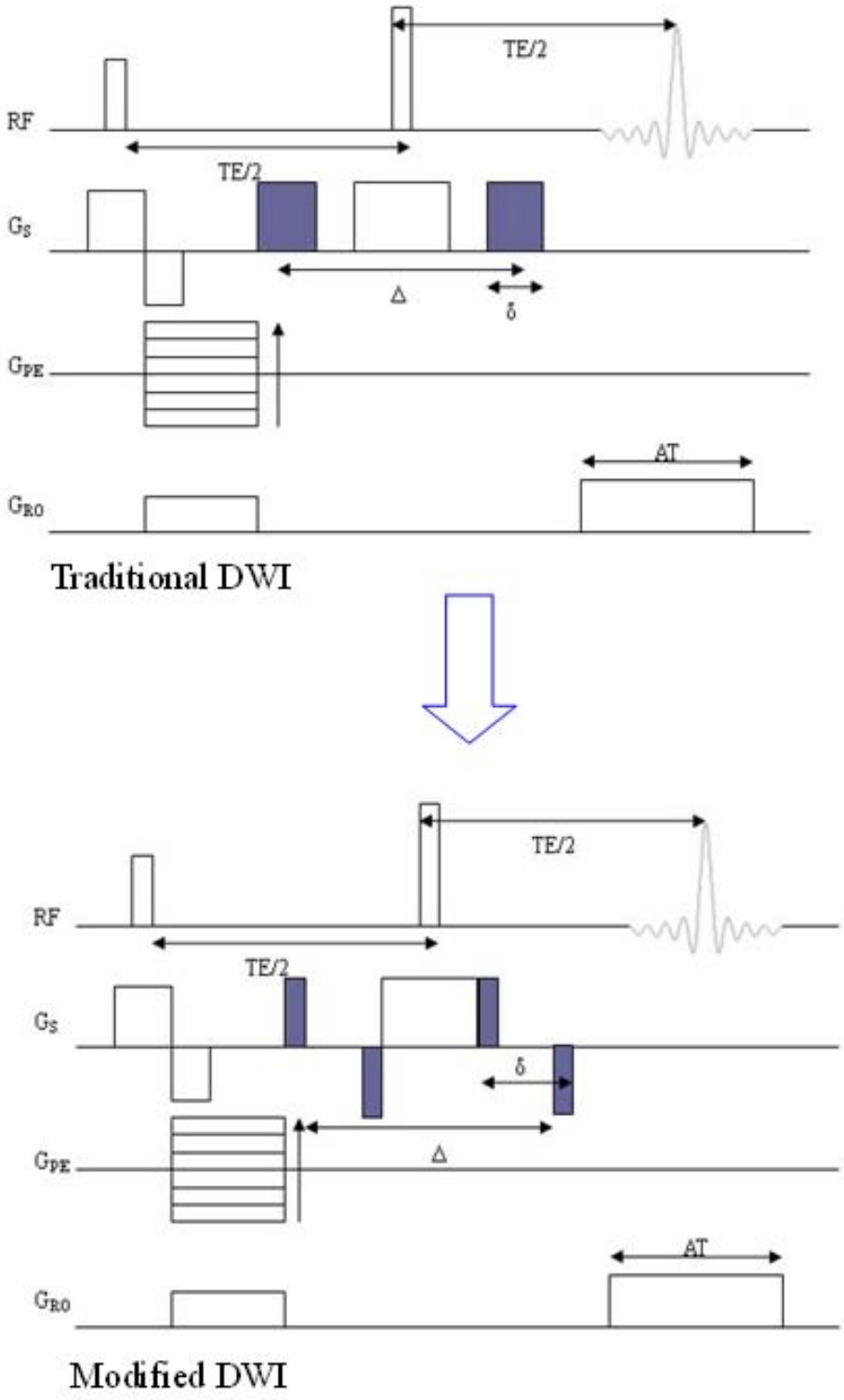

Figure 7: Traditional (upper) and modified (lower) pulse field gradient sequences. Each single lobe of the diffusion gradients is replaced by a bipolar gradient pair to cancel the effects from the interactions of imaging gradients.

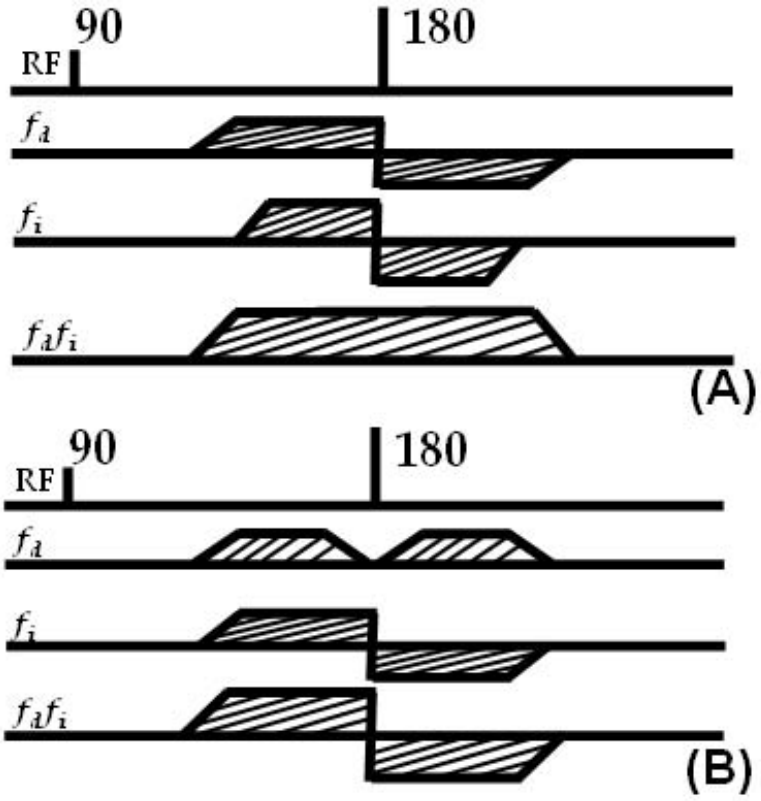

Figure 8: The f_i, f_{id} and $f_i f_d$ for traditional (A) and modified (B) diffusion weighted sequences. It can be seen that in the modified DWI sequence, the "cross term effect" integrates to zero at the time of signal sampling.

3.5 Summary

Two important aspects of MRI covered in the current chapter are: contrast mechanisms and tissue's biophysical properties. These knowledge is essential for the understanding of multicontrast MRI plaque imaging and MR property based tissue labeling, which will be touched in later chapters.

CHAPTER IV

MULTICONTRAST MRI OF CORONARY PLAQUES UNDER SIMULATED *IN-VIVO* CONDITIONS

4.1 Introduction

Several technical difficulties hinder the clinical practice of coronary vessel wall imaging. First of all, the tiny size of coronary atherosclerotic plaques requires high resolution scans to reveal the morphological details needed in evaluating plaque vulnerability. Acquisition-wise, high resolution usually means compromise of the SNR and increase in scanning time. Analysis-wise, small plaque size makes registration of MR images with different contrast mechanisms more difficult. Additionally, the deep location of coronary vessels in the human body usually causes significant SNR reduction due to the relatively low sensitivity of cardiac coils. Moreover, physiological motions including heart beat and respiration inevitably introduce artifacts and increase difficulty in high resolution scans. Despite the recent development in coronary vessel wall imaging owing to imaging techniques like navigator echo and radial sampling, it is still the consensus that current resolution and SNR are insufficient for coronary plaque characterization.

Due to these difficulties, MR plaque imaging studies are mainly focused on carotid plaques. For coronary atherosclerotic plaques, only limited MR studies have been conducted under *ex-vivo* conditions. Valuable knowledge has been gained from *ex-vivo* research on coronary plaque MRI. However, there are concerns that tissue preservation may affect MR image contrast and hence influence plaque characterization. Therefore, assessing the effects of preservation is critical to ensure that multicontrast characterization techniques developed for preserved coronary plaques still apply for *in-vivo* imaging.

4.2 Coronary Artery Preparation

In the current study [91], all the coronary artery samples were acquired from the explanted hearts of transplant patients recruited at Emory University Hospital. Totally, fifteen vessels

were selected for the current study. Healthy and extremely calcified vessels were excluded.

For all the samples, the following vessel preparation procedure was conducted. The explanted hearts were placed in ice-cold Kreb's solution immediately after explantation. Coronary arteries were removed from the transplanted heart within an hour and placed in Medium 199 and kept in an incubator at $37°C$ until scanned. Medium 199 contains inorganic salt, vitamins, amino acids and several other components that support the growth of cells. MRI scans were performed on average 4 ± 2 hours after explantation (all within 24 hours of surgery). Following the scan, MR images were inspected to identify atherosclerotic plaques and evaluate image quality. The vessels were fixed and stored in 10% buffered formalin solution (*Fisher Scientific, Pittsburgh, PA*) for 48 hours. Ten of the fifteen vessels were scanned a second time to evaluate the influence of preservation on multicontrast MRI of coronary plaques. The other five vessels did not undergo the second scan for reasons related to scanner availability. In the ten vessels that were scanned twice, five were from heart failure patients with non-ischemic etiology and five vessels were from heart failure patients with ischemic cardiomyopathy. Typical atherosclerotic plaque components, including necrotic core, fibrous cap, calcification, and dense fibrous tissue were present in the vessels. The study was approved by the university's institutional review board.

4.3 Tissue Culture Chamber

To approximate *in-vivo* conditions, a custom-designed MR-compatible tissue culture chamber was built to keep temperature, pressure and nutrient environment of the vessels at *in-vivo* levels during MR scanning. Figure 9 shows the front and side view of the chamber.

The chamber consists of a $35mm$ diameter cylindrical polycarbonate tube, which holds vessel specimens and tissue culture media. End caps are present on each side of the tube. On each cap, there is a cannula connected to the inside of the vessel, then to plastic tubes that run outside the bore. The purpose of these plastic tubes is to perfuse the vessels and to maintain a specific inner pressure in order to maintain vessel morphology mimicking to the *in-vivo* situation. An orifice on the tissue culture chamber provides access to an MR compatible thermocouple so that the temperature can be monitored during the imaging

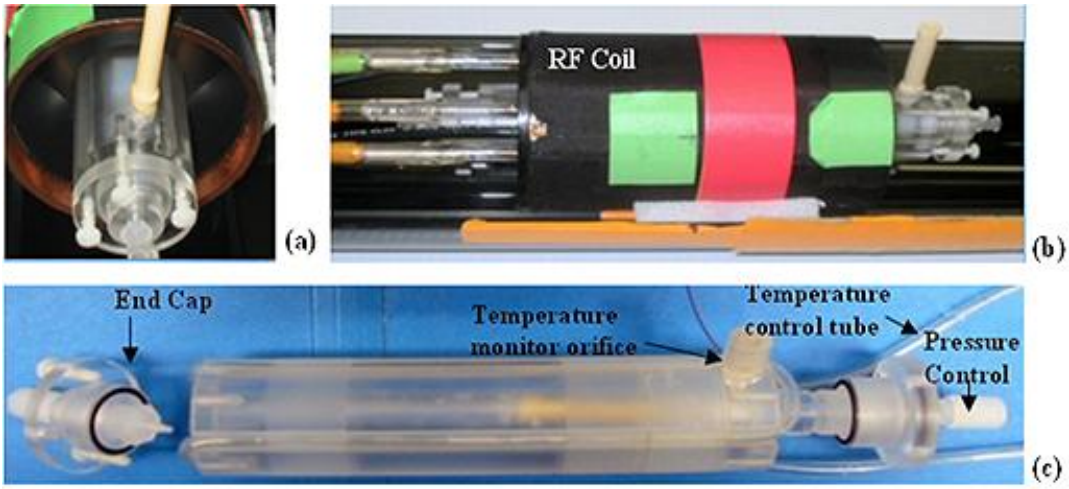

Figure 9: MR-compatible tissue culture chamber (a) front-view and (b) side-view of the chamber inside the birdcage coil; (c) detailed view of the chamber with description.

session. The chamber was filled with Medium 199 (T1$\approx 3.4s$ at $37°C$) to provide necessary nutrient environment for vessel tissues. Temperature was kept at $37°C$ via warm water circulating around the chamber through a plastic tube. The use of tissue culture system in simulating the *in-vivo* conditions has been justified by previous research [75]. Furthermore, vessels were imaged within 24 hours to ensure the viability of tissue constituents.

4.4 MRI Acquisition

Prior to the acquisition, plastic markers producing no MR signal were attached to each vessel and the vessel was mounted on cannulas. These markers contained no MR signal and were used to register MR images with histological slices during image analysis.

The MR scans were conducted on a 4.7T small animal MR scanner (*INOVA, Varian, Inc., USA*) with a 37-mm-diameter 16-element birdcage quadrature coil. Proton density weighted SE (TR/TE=$3.5s/15ms$), T2 weighted SE (TR/TE=$3.5s/50-60ms$), T1 weighted SE (TR/TE=$0.9-1.4s/15ms$) and diffusion weighted SE ($b = 234s/mm^2$) images were obtained with four signal averages. In addition, two partial T2 weighted SE (TR/TE=$3.5s/30-40ms$) and one to four diffusion weighted images ($b = 0-300s/mm^2$) were acquired to measure quantitative T2 and ADC values for plaque components. Field-of-view (FOV) was $3cm \times 3cm$ and an acquisition matrix of 256×256 was used (resolution

after zero filling=58.6$\mu m \times 58.6\mu m$). Slice thickness was $1mm$. Multiple slices were acquired alternatively to avoid cross-talk. Imaging parameters for the preserved vessels were kept the same as those for the fresh vessel to facilitate comparison. Eighteen to twenty-one slices were acquired per vessel with no gap.

4.5 Histology

After imaging, each of the 15 vessels were embedded in Methyl Methacrylate (MMA) and $5\mu m$ serial sections were obtained. Hematoxylin and Eosin (H&E), Masson's Trichrome, Smooth Muscle Actin, and Verhoeff-Van Gieson stains were then performed on each section. The histological sections serve as the "reference standard" in evaluating plaque component characterization. Decalcification was not performed prior to the sectioning so as to keep the calcification information. The following vascular components were identified by histology: lipid/necrotic core, fibrocellular/fibrous cap, fibrous tissue, thrombus, media/extracellular matrix and calcification.

In general, multicontrast MR images correlated well with corresponding histological stains. Two examples, a relatively healthy vessel (Fig. 10(A)) and a fibrotic plaque ((Fig. 10(B))), are shown to demonstrate this. In the following section, specific attention will be paid to the comparison between multicontrast MR results of fresh and preserved vessels.

4.6 Effects of Vessel Preservation on Multicontrast MRI

Atherosclerotic tissue types in all the ten vessels scanned under fresh and preserved conditions included dense fibrous tissue, calcification, media/extracellular matrix, lipid core, fibrous cap, fresh thrombus, intimal hyperplasia, neo-intima and sections of relatively healthy vessel. Among the five vessels from subjects with ischemic dilated cardiomyopathy, two contained fibrotic lesions (AHA type Vb-Vc); one contained a complicated lesion with overlying thrombus (AHA type VI); and two contained fibroatheroma plaques (AHA type V).

4.6.1 Qualitative Comparison Between "Fresh" and "Preserved" Multicontrast MRI

The multicontrast MR images of both fresh and preserved vessels were aligned with the help of plastic markers and morphological landmarks. The results demonstrated a good

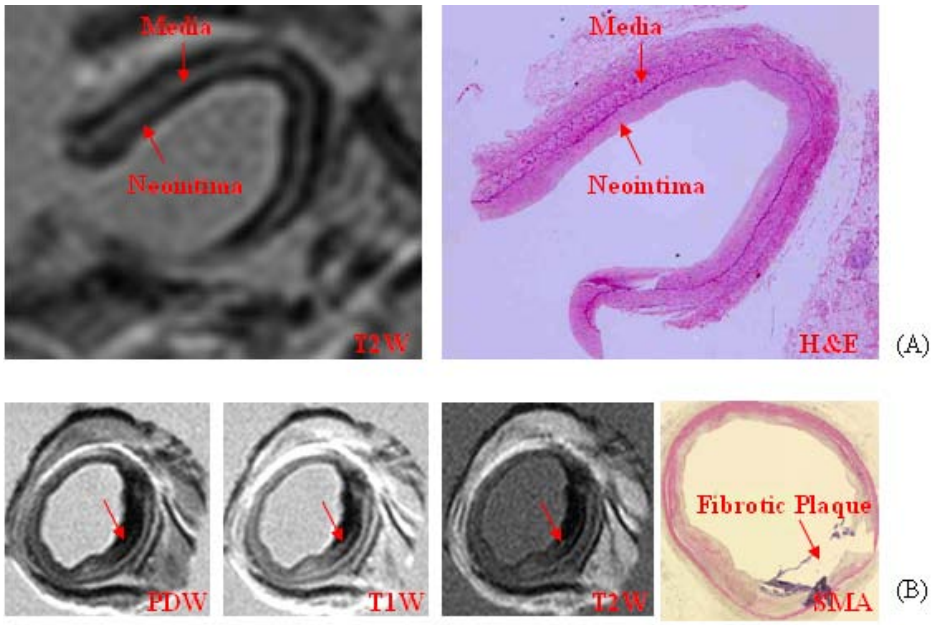

Figure 10: MR and corresponding histological images of fresh coronary vessels. (A) the T2 weighted MR image and the H&E stain of a comparatively healthy vessel, (B) Proton density, T1 and T2 weighted MR images of a fibrotic plaque and smooth muscle actin stain from the same location.

visual correspondence between MRI scans and histology.

An example comparison of fresh scan, preserved scan and histology from an advanced lesion is shown in Figure 11. The images shown are typical for the results of all vessels. In general, the visual appearance of the multicontrast results from scans under fresh and preserved conditions were comparable. The contrasts between plaque tissues does not seem to be affected by the viability and freshness of most of the plaque tissues. However, in one case, we identified an apparent intensity change for fresh mural thrombus. This case is shown in Figure 12. It can be seen that the mural thrombus identified on histology changes from hypo-intense to iso/hyper-intense after the preservation.

It was not surprising that the appearance of thrombus was different between fresh and preserved conditions. In previous studies, it has been reported that thrombus usually gives a non-uniform appearance in MR images [19, 80]. The fresh thrombus is hypo-intense because of the iron-bearing red blood cells. Iron products, behaving similar to contrast agents, change the local magnetic field and accelerate MR signal de-phasing. It affects T2 and diffusion weighted images via proton diffusion. T1 and proton density weighted

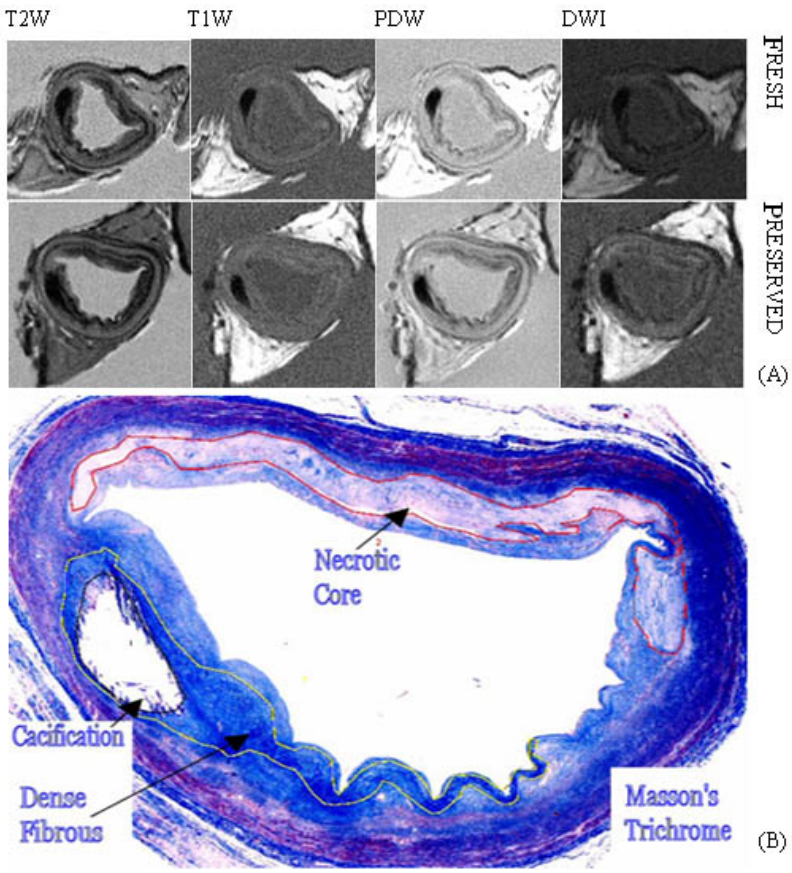

Figure 11: Comparison of multicontrast (T2, T1, Proton Density and Diffusion Weighted) MRI results with histology. (A) multicontrast MRI acquired under fresh and preserved conditions for the same location, (B) corresponding Masson's Trichrome stain.

images are less affected because of the shorter TE value used. In this study, the age of the thrombus at the fresh stage was not known. From its MR appearance, it was postulated to be comparatively fresh.

4.6.2 Signal-to-Noise Ratio Comparisons

Signal-to-Noise (SNR) for media, fibrous cap, necrotic core and dense fibrous tissue were measured on proton density and T2 weighted MR images for both "fresh" and "preserved" scans. The SNR of each plaque component is defined as its mean signal intensity divided by the standard deviation of noise, which is calculated from regions without MR signal (e.g. air). The grouped results were compared using a two-tailed, paired sample t-test. SNR was not measured for T1 and diffusion weighted MR images because of the lower contrast of plaque tissues in these images.

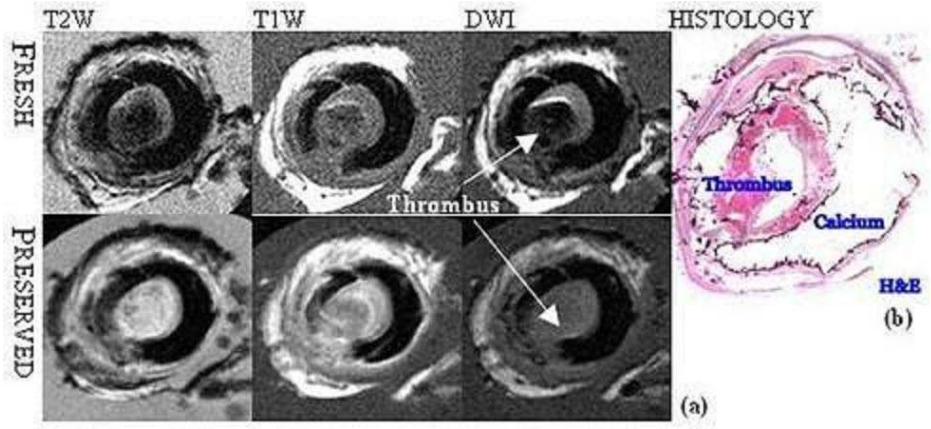

Figure 12: Example shows apparent signal intensity change for fresh thrombus after the preservation. Thrombus changes from hypo-intense at fresh stage to hyper-intense after preservation on T2 and diffusion weighted images. (a) shows the multicontrast MR images and (b) shows the corresponding H&E stain.

The SNR is determined for the fresh and preserved conditions for each plaque component are summarized in Table 2. The comparison showed better SNR was obtained under preserved conditions over fresh conditions, which may be due to the fixation process during preservation. This small change ($p = 0.02$) in SNR may imply small changes in tissue's MR properties.

Thrombus was excluded from the SNR analysis because of the non-uniformity of its intensity on MR images. In contrast to other plaque constituents, thrombus did show apparent signal change between MR scans under fresh and preserved stages. In the thrombus region of one vessel, intensity changed from hypo-intense at fresh stage to hyper-intense after preservation (Fig. 12). As mentioned above, the change in signal intensity of thrombus depends on its age and may be related to the reduction of intact red blood cells filled with iron-rich products from deoxyhemoglobin breakdown [39].

4.6.3 T2 and ADC Comparisons

Quantitative T2 and ADC maps were calculated using the acquired MRI data. Quantitative T2 and ADC maps are images whose pixel intensities reflect the T2 and ADC values of the spatial location, respectively. The computation of these maps relies on the theory discussed

Table 2: SNR of Major Plaque Components in T2 and Proton Density Weighted MR Images of Fresh and Preserved Vessels

		Media	**Dense Fibrous**	**Fibrous Cap**	**Lipid Core**	**Grouped p-value**
PD Weighted	Fresh	32.6±3.9	22.4±7.4	35.2±1.7	25.6±0.9	0.002
	Preserved	35.6±2.5	24.9±13.3	35.8±3.6	27.2±0.1	
T2 Weighed	Fresh	15.2±12.1	6.2±2.6	22.4±8.5	9.7±7.8	0.003
	Preserved	16.5±16.8	6.3±3.4	24.3±3.9	11.4±0.7	

†Thrombus not included for its non-uniform intensity appearance in PD and T2 weighted MR images.
‡STDs shown are STDs between slices and vessels.

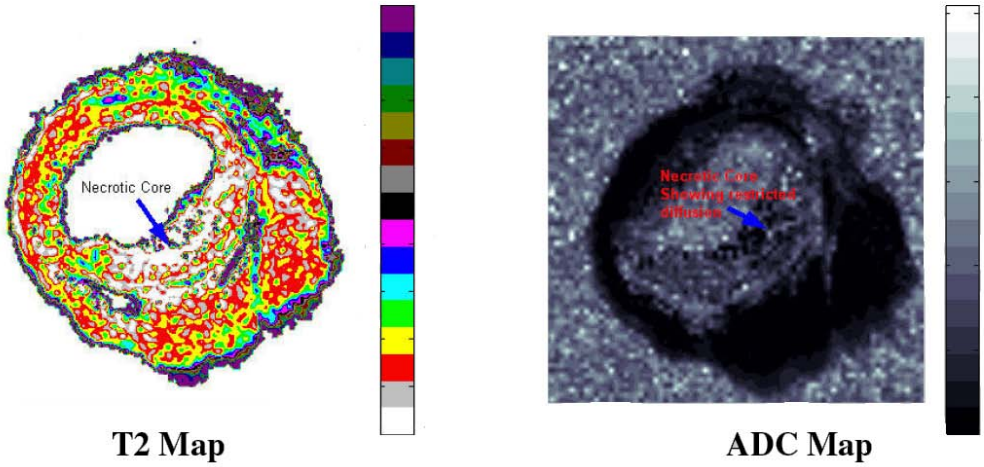

Figure 13: The T2 and ADC maps at a location of a plaque with necrotic core.

in the quantitative MRI section. In our study, four MR images (TR/TE $= 3.5s/30-60ms$) were used to generate the quantitative T2 maps and two to five diffusion weighted MR images ($b = 0-300s/mm^2$) were used to generate the ADC maps. In Figure 13, a T2 map and an ADC map at a location with necrotic tissue is shown.

To measure the quantitative T2 and ADC values for plaque components, the fitted T2 and ADC maps were manually characterized with the guidance of histological images. Specifically, manual segmentation groups the regions on quantitative maps to one of the following category: background tissue culture media, adipose fat, fibrocellular, fibrous tissue, necrotic core and media/extracellular matrix. Thrombus was excluded from the measurements because only one instance was captured and also because of the variable T2 values

for this tissue type. T2 and ADC values of pixels belonging to a specific tissue type on these characterized maps were determined.

Based on these measured values, the means and standard deviations of these plaque components were calculated and summarized in Table 3. The student t-test on T2 values shows a small, but significant difference in all plaque constituents between fresh and preserved stages. The media/extracellular matrix showed the most significant changes in T2 after preservation.

Previous research by Toussiant et al. [93] evaluated the influence of vessel "freshness" on MRI of carotid arteries with a different preservation procedures that involved freezing vessels to -60°C rather than formalin fixation. In that study, T2 values of major plaque components (fibrous cap, media, lipid core and adventitia) were determined using a clinical scanner. T2 values were found to be similar between *in-vivo* and *ex-vivo* conditions. However, poor resolution and questions about the accuracy of the dual-echo, T2 measurement sequence caused potential errors. A study by Dalager-Pedersen et al. [20] evaluated the influence of formalin preservation on the size, morphology and T2 property of carotid plaques at room temperature. They found that changes introduced by formalin fixation were minimal compared to those introduced by temperature change and decalcification process. Of all plaque constituents, only media showed a significant, but small, change in T2 value as a result of this process. The different results between their study and ours may be due to the vessel prepare procedure difference. In that study, vessels were taken at autopsy and frozen to -18°C, so no scans on real "fresh" vessels were done.

It should be noted that similar to previous research [81], our results with T2 values showed limited contrast between necrotic core and fibrous tissues. The reason for the similarity in appearance may due to the similarity in composition between fibrous tissue and "hard" necrotic core. Clinically, there are two kinds of necrotic cores: "soft" and "hard". The "soft" core usually contains semifluid extracellular lipid, while the "hard" ones contain mainly collagen and tissue debris. Because of the patient population in the current study, the majority of necrotic cores we captured are "hard" ones.

Our measured ADC values of fibrous tissue and media are similar to those of collagenous

Table 3: T2 and ADC Values for Plaque Tissues of Fresh and Preserved Vessels

	T2(ms)		**ADC**(cm^2/s)	
	Fresh	**Preserved**	**Fresh**	**Preserved**
Media	49.7±9.7	58.0±12.5	1.9±0.8	2.3±1.1
Fibrous Tissue	28.8±8.7	32.9±7.8	1.3±0.8	1.5±0.7
Necrotic Core	30.6±7.0	34.9±5.1	0.9±0.6	1.10.4
Fibrocellular	54.7±10.7	62.4±10.1	2.2±0.8	1.9±0.5
Adipose Fat	43.2±6.3	40.7±6.7	0.24±0.05	0.25±0.06

caps measured by Toussiant et al. [95]. The ADC value of our adipose fat region is similar to the ADC value of lipid core measured by previous studies [5, 95], however, our measured ADC values in necrotic core regions show higher diffusivity. This can be explained by the limited presence of excellular lipid in these necrotic cores.

4.7 Conclusions

In our study of explanted coronary arteries, efforts were made to simulate the *in-vivo* conditions for explanted coronary vessels. This is critical since plaque characterization techniques (both manual and automatic) reported in the literature rely heavily on techniques developed using *ex-vivo* scans. Furthermore, there is still no report of *in-vivo* multicontrast coronary plaque because of the technical difficulties. Therefore, the current study also facilitates the evaluation of multicontrast MRI coronary plaque characterization in future clinical studies. A subset of vessel samples (10 out of 15) were chosen to be imaged a second time after preservation in order to access the impact of vessel viability on multicontrast MR results.

From the imaging results, the multicontrast MRI could be used to positively characterize atherosclerotic plaques. This has already been verified by many previous studies. The significance of our research is that we further demonstrated that coronary arteries under the simulated *in-vivo* conditions give similar results as those obtained from preserved vessels. This provides justification hypothesizing a possible clinical utility for MR coronary plaque characterization, provided technical issues can be overcome.

When comparing the multicontrast MRI results of fresh and preserved vessels, it is

observed that the contrasts of most plaque components (except fresh thrombus) are comparable on the multicontrast MR images between fresh and preserved vessels. The primary inference of this observation is that it may be acceptable to adapt plaque characterization techniques developed based on *ex-vivo* multicontrast MRI to *in-vivo* studies. The verification of this claim is postponed to the next chapter, where automatic plaque characterization is introduced. It should be noted that this claim is only true for plaque characterization algorithms relying on comparative intensity of each plaque constituents. Under this situation, the changes of tissues' MR properties are not necessarily coupled with a change in plaque characterization results. In contrast to this, retraining is needed for plaque characterization techniques, which rely on absolute values such as intensity or T2 (e.g. PIEC technique covered in the next chapter).

The quantitative MR properties including T2 and ADC for all typical plaque constituents show small yet significant changes after preservation. In addition, slightly better SNR was achieved for multicontrast MR images from preserved vessels. The implication of these results suggests that the viability of plaque tissue components does affect the multicontrast MR results. Any plaque characterization technique relying on quantitative MR properties may be subject to modifications when adapting from *ex-vivo* to *in-vivo* studies.

CHAPTER V

AUTOMATIC PLAQUE CHARACTERIZATION EMPLOYING MULTICONTRAST MRI

5.1 Introduction

The main purpose of multicontrast MRI is to characterize the composition and morphology of atherosclerotic plaques in order to assess their vulnerability. As of now, plaque characterization using multicontrast MRI data still relies heavily on manual segmentation. This approach requires expertise and is time-consuming. In addition, the manual characterization results are subject to inter and intra-observer biases. One of the primary goals of this thesis is to develop an automatic plaque characterization technique to mitigate these difficulties.

Several researchers [2, 16, 17, 43, 61, 105] have already investigated the feasibility and performance of a variety of automatic characterization techniques that can facilitate plaque constituent differentiation. Following the methodology of manual characterization, the majority of these techniques characterize plaque constituents based on their comparative contrasts on MR images of each contrast mechanism (e.g., tissue appearing very hypo-intense on proton, T1, T2 as well as diffusion weighted images should be calcification.). The comparative contrasts are usually summarized as an intensity table, which is used to label plaque components [2, 27, 30, 43, 83]. Despite the wide application of this approach, there are several issues that hinder its application for automatic plaque characterization. Firstly, the intensity table is imaging parameter dependent, and thus needs to be generated exclusively for the chosen set of imaging parameters. Therefore, it is not surprising that the intensity table differs among various studies. This increases the complexity of plaque characterization, and more importantly, makes automatic plaque characterization inapplicable when the table is not available. Secondly, unsupervised techniques [2, 43] require knowing all the plaque constituents present prior to characterizing a specific multicontrast MR dataset to

avoid over or under classification. Supervised techniques [16, 17, 61] do not require this prior knowledge. However, repetitive training needed for supervised techniques makes them more susceptible to changes in the imaging sequences and parameters. Lastly, unsupervised techniques [2, 43] may encounter logic difficulties that hamper characterization. For example, assuming there are three tissues present in plaques with their intensity $A > B > C$, if there are only two tissues (X, Y) present in a specific plaque, then X and Y can be any combination of either two of the three possible constituents (A, B, C). Because of this, additional restrictions or user interactions have to be employed in cases of this ambiguity. Supervised techniques [16, 17, 61] do not have this logic difficulty. However, even a small change in imaging conditions may cause erroneous characterization results if the supervised classifier was not retrained. This renders the supervised techniques extremely sensitive to imaging conditions - parameters, scanning system, pulse sequences and even post-processing.

It is worthwhile to reemphasize the differences of classification, labeling and characterization in the current thesis (see also Chapter II). Classification is regarded as the step that differentiates plaque components, while labeling is the post classification step that labels clustered constituent groups. Characterization is a combination of classification and labeling. For supervised techniques, labeling is woven into the classification step. For unsupervised techniques, on the other hand, separate logic (e.g., comparative contrast) is needed to label classified results. From the above general discussions about the pros and cons of supervised and unsupervised plaque characterization techniques, it can be seen that all the difficulties are related to the labeling of plaque components. Because supervised characterization techniques have no separate labeling step, improvements regarding the characterization difficulties could be more easily made to unsupervised techniques.

In the current thesis, efforts were dedicated to combine a clustering based classification technique with a labeling step that is independent of imaging parameters to resolve the issues associated with the existing automatic plaque characterization techniques. The organization of this chapter is as follows: in the first half, unsupervised clustering techniques are introduced to classify/segment plaque constituents; in the second half, labeling techniques are described and combined with classification to yield characterization techniques.

The characterization techniques were applied to both the acquired multicontrast MR data described in the previous chapter and simulated data sets for evaluation.

5.2 Plaque Component Classification/Segmentation

Tissue classification/segmentation is a fundamental task in image processing and is involved in many clinical applications [8]. Despite the large number of segmentation methods available, two major categories can be identified: edge-based and intensity-based segmentation. Intensity-based segmentation algorithms group pixels based on intensity similarity and are more heavily used in classification work than edge-based segmentation. Since multicontrast plaque characterization involves classification based on multiple images, intensity-based segmentation techniques are more easily applicable, and thus selected for this purpose.

5.2.1 Fuzzy C-Means Classification

As an intensity-based classification/segmentation technique, Fuzzy C-Means (FCM) clustering [7] has been applied widely in MR tissue classification tasks [40, 60, 71]. A FCM algorithm classifies the image purely based on intensity. Each pixel is assigned a membership function, which resembles the percentage of this pixel that belongs to each class. Defuzzification of the membership matrix by picking up the highest percentage class as the class of this pixel generates the final classification result. For instance, pixel i with highest similarity to centroid j will have a greater value of $M_{i,j}$ than $M_{i,k}$ (k can be any class other than j), this ensures the classification correctness using a maximum *a posteriori* (MAP) like defuzzification scheme.

Specifically, the FCM classification is realized by minimizing the objective function formulated as Equation (20). Here, $M_{i,j}$ is the membership function of pixel i to be class j with fuzzification factor m, x_i is the intensity of pixel i, w_j is the centroid for class j, c is the total class number, and n is the total pixel number.

$$J_{FCM} = \sum_{j=1}^{c} \sum_{i=1}^{n} M_{i,j}^{m} \|x_i - w_j\|^2 \tag{20}$$

Usually, typical pixel intensities for all classes are manually selected as the initial centroids for the objective function. The objective function is then numerically resolved through a gradient descent minimization search with an additional restriction that the summation of all the memberships for a specific pixel.

Based on gradient descent minimization search, the membership function could be calculated with Equation (21). In this equation, the second term on the left hand side is the Lagrange multiplier that constrains the membership function summation of any pixel in the image domain, Ω, equals to one.

$$\frac{\partial J_{FCM}}{\partial M_{i,j}} + \sum_{i \in \Omega} \lambda_i (1 - \sum_{j=1}^{c} M_{i,j}) = 0 \tag{21}$$

Partial differentiating Equation (21), the membership function is derived as Equation (22). With the constraint that the summation of membership function equals to 1 (Equation (23)), λ_i can be derived as Equation (24). Based on Equations (22) and (24), the final solution for pixel membership can be derived (Equation (25)).

$$M_{i,j} = [\frac{m\|x_i - w_j\|^2}{\lambda_i}]^{\frac{1}{1-m}} \tag{22}$$

$$\sum_{j=1}^{c} M_{i,j} = 1 \tag{23}$$

$$\lambda_i = (m \sum_{j=1}^{c} (\|x_i - w_j\|^{\frac{2}{1-m}}))^{1-m} \tag{24}$$

$$M_{i,j} = \frac{\|x_i - w_j\|^{\frac{2}{1-m}}}{\sum_{k=1}^{c} (\|x_i - w_k\|)^{\frac{2}{1-m}}} \tag{25}$$

In a similar fashion, the centroid of the FCM objective function is subject to Equation (26) and the solution is derived as Equation (27).

$$\frac{\partial J_{FCM}}{\partial w_j} = 0 \tag{26}$$

$$w_j = \frac{\sum_{i=1}^{n} M_{i,j}^m x_i}{\sum_{i=1}^{n} M_{i,j}^m} \tag{27}$$

With the above mathematical derivation, the numerical scheme in minimizing the FCM objective function can be summarized as follows.

1. Manually select a set of initial centroids w to start the FCM minimization.
2. Employ Equation (25) to calculate the membership function.
3. Update class centroids with Equation (27).
4. Evaluate the convergence of the objective function by checking the maximum change (absolute value) of the membership functions. If it is bigger than a preset threshold ϵ, return to step 2 otherwise stop the minimization.
5. Assign the class type of each pixel to its highest membership.

Since the total image pixel number is limited, the FCM objective function ensures the existence of a global minimum (i.e., there exists a single configuration where the energy function is minimized). However, in numerical form, FCM may converge to a non-optimized local minimum for its seed-dependent property. To make sure that this undesired property of FCM has minimal effects on classification results, a reasonably selected initial centroid set is usually needed.

5.2.2 Spatially Penalized Fuzzy C-Means Classification

From the previous section, it can be seen that only intensity information is utilized during the FCM classification. The lack of spatial information makes this technique highly sensitive to noise. To suppress the noise, pre-classification smoothing and post-classification majority filtering could be applied to reduce the misclassification error. An alternative approach of including spatial penalty terms in the objective function were shown to mitigate this problem more efficiently while preserving small features in the images [58, 72].

In the current research, a spatially penalized FCM (SPFCM) technique [72] was adapted and modified for the purpose of plaque classification. In the SPFCM technique, an additional spatial constraint term is introduced to FCM objective function to yield Equation (28).

$$J_{SPFCM} = \sum_{j=1}^{c}\sum_{i=1}^{n} M_{i,j}^{m}\|x_i - w_j\|^2 + \alpha \sum_{j=1}^{c}\sum_{i=1}^{n} M_{i,j}^{m} \sum_{t=1\ldots c, t\neq j} \sum_{l\in Neighbor(i)} M_{l,t}^{m} \tag{28}$$

In this equation, the first term of the function is the traditional FCM objective function, which groups the pixels relying only on their intensity similarity. The second term, restricted by spatial relationships, reduces the membership function $M_{i,j}$ when the neighboring pixels of pixel i have a large sum of memberships in classes other than class j. This configuration makes the FCM more noise resistive, though there is a tradeoff between noise suppression and small feature preservation.

Following similar minimization approach as FCM algorithm, the updating scheme for membership function is derived as equations (29). The centroid updating function stays the same as Equation (27).

$$M_{i,j} = \frac{(\|x_i - w_j\|^2 + \alpha \sum_{t=1\ldots c, t\neq j} \sum_{l\in Neighbor(i)} M_{l,t}^{m})^{\frac{1}{1-m}}}{\sum_{k=1}^{c}(\|x_i - w_k\|^2 + \alpha \sum_{t=1\ldots c, t\neq k} \sum_{l\in Neighbor(i)} M_{l,t}^{m})^{\frac{1}{1-m}}} \tag{29}$$

Because of the inclusion of spatial constraint in the objective function, SPFCM gives much better classification results than FCM in the presence of noise. An example is shown to illustrate this point. Figure 14(A) shows a synthetic image with 4 intensities symbolizing 4 different tissues. Gaussian noise was added to the synthetic image to generate a corrupted image Figure 14(B). The classification results of FCM and SPFCM are shown in Figures 14(C) and (D), respectively. From the results, SPFCM shows apparent advantages over FCM for its noise resistance.

In applying SPFCM classification to multiple slice MR data of plaques, the three dimensional version of this algorithm (3D-SPFCM) incorporating both in-plane and longitudinal

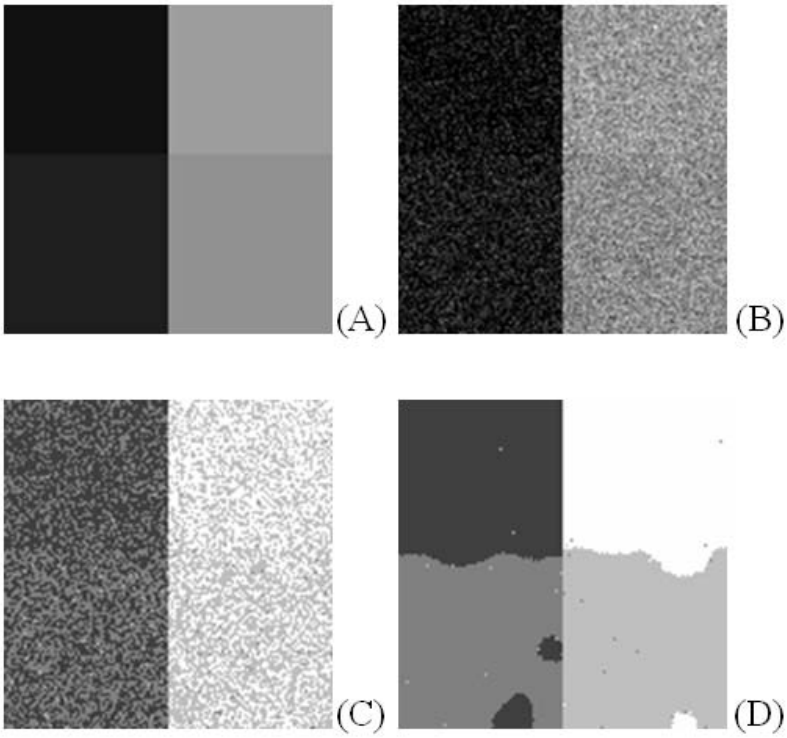

Figure 14: Comparison of the SPFCM and FCM results of a noise corrupted synthetic image. (A) a synthetic image with 4 intensities symbolizing 4 different tissues, (B) Gaussian noise corrupted version of (A), (C) and (D) are the FCM and SPFCM classification results, respectively.

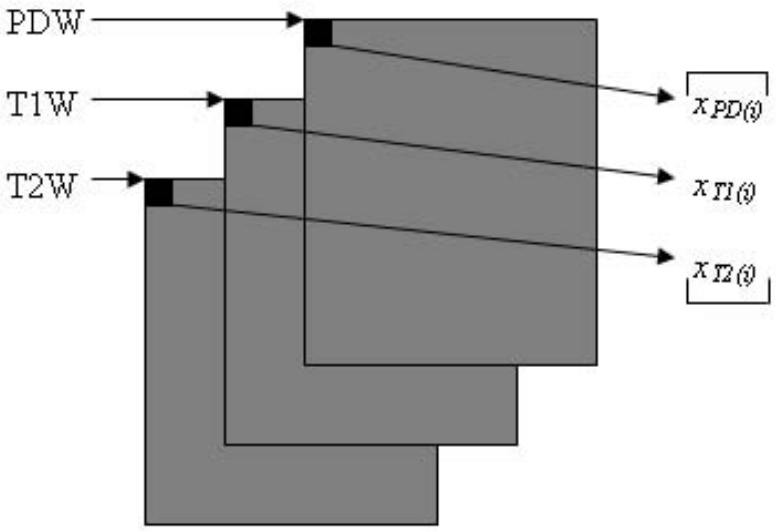

Figure 15: schematic drawing illustrating multicontrast data.

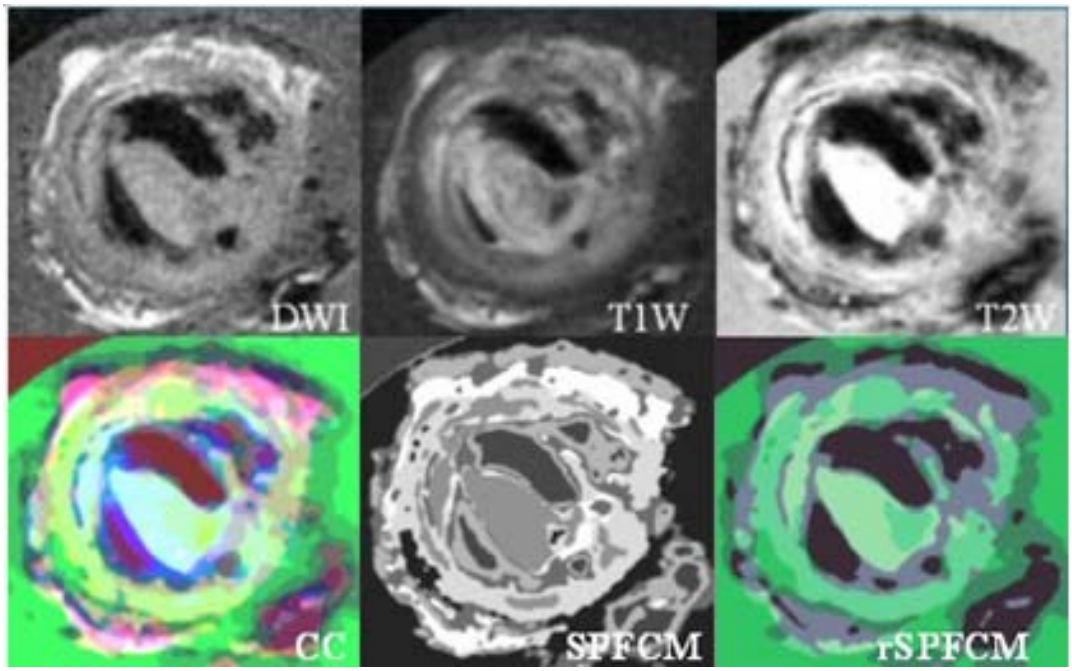

Figure 16: Example shows the superiority of regularized SPFCM (rSPFCM) to SPFCM in avoiding local minimum. Direct RGB color composition (CC) of DWI, T1W and T2W are shown for comparison.

spatial constraints can be used. 3D-SPFCM follows the same procedure as SPFCM but change the $Neighborhood(i)$ from 2D to 3D. In applying the 3D-SPFCM, smaller weighting was assigned to spatial constraint on the longitudinal direction than in-plane in compensating for the non-isotropic size of the MR image voxels.

The MR images were intentionally over classified first to avoid any merging of different tissues. Then the resulting n centroids of SPFCM algorithm were evaluated to inspect whether they are well separated. If the Euclidian distance between any two centroids is less than a preset threshold, the SPFCM algorithm will be recalculated with $(n-1)$ initial centroids.

When SPFCM is applied to multicontrast MR images, the pixel intensity and centroid should be replaced by vectors, i.e. $x_i = [x_{PD(i)}, x_{T1(i)}, , x_{T2(i)}]^T$, $w_j = [w_{PD(j)}, w_{T1(j)}, , w_{T2(j)}]^T$. A schematic drawing shown in Figure 15 illustrates this idea.

For multicontrast MR data, the seed dependent problem worsened because of the increased data dimensionality. To ameliorate the local minimum problem prevalent in multicontrast classification, a regularization step can be employed. Regularized SPFCM is

conducted by first classifying the MR images of each contrast separately. And then, each of these images is regularized by averaging the intensities of the pixels that have been labeled as the same class in the previous classification results. Lastly, the regularized images are fed to the SPFCM objective function to generate the final classification result. In Figure 16, a sample multicontrast dataset with diffusion, T1 and T2 weighted images is shown. The SPFCM and regularized SPFCM classification results reveals the improved performance attribute to regularization. The flow chart of the regularized 3D-SPFCM algorithm is shown in Figure 17.

5.2.3 Map Guided Intensity Correction Fuzzy C-Means

Unfortunately, noise is not the only source of error in MR image classification. A very common image quality problem for MRI is caused by intensity variations. Intensity variations in MR images can arise from stationary (B_0) and/or excitatory (B_1) magnetization inhomogeneity, partial volume effect (PVE), gibbs ringing artifact, ghosting artifact from motion, etc. Some of these signal non-uniformities are hardware related and are inevitable during the acquisition process. A thorough review of intensity variations in MR images can be found in reference [18].

Generally, these intensity variations degrade the performance of FCM and other intensity based segmentation algorithms, and thus lead to erroneous results. In order to reduce the influence from intensity variations, either modeling of the corruption process, or separating out the variations based on their specific properties is needed.

As shown previously, noise, a special kind of intensity variation, can be successfully suppressed by the SPFCM. The correction of other intensity variations, however, appears to be more difficult. To correct the corrupted images with no additional information available, an assumption needing to be met is that the corrupted images have more information than uncorrupted ones.

Numerous inhomogeneity correction schemes have been reported in literature [4, 12, 21, 45, 59, 64, 73, 84, 90, 92, 103, 104, 111]. One of the most investigated techniques is applying the field map estimated from reference scans to correct the inhomogeneities [4, 84, 104]. The

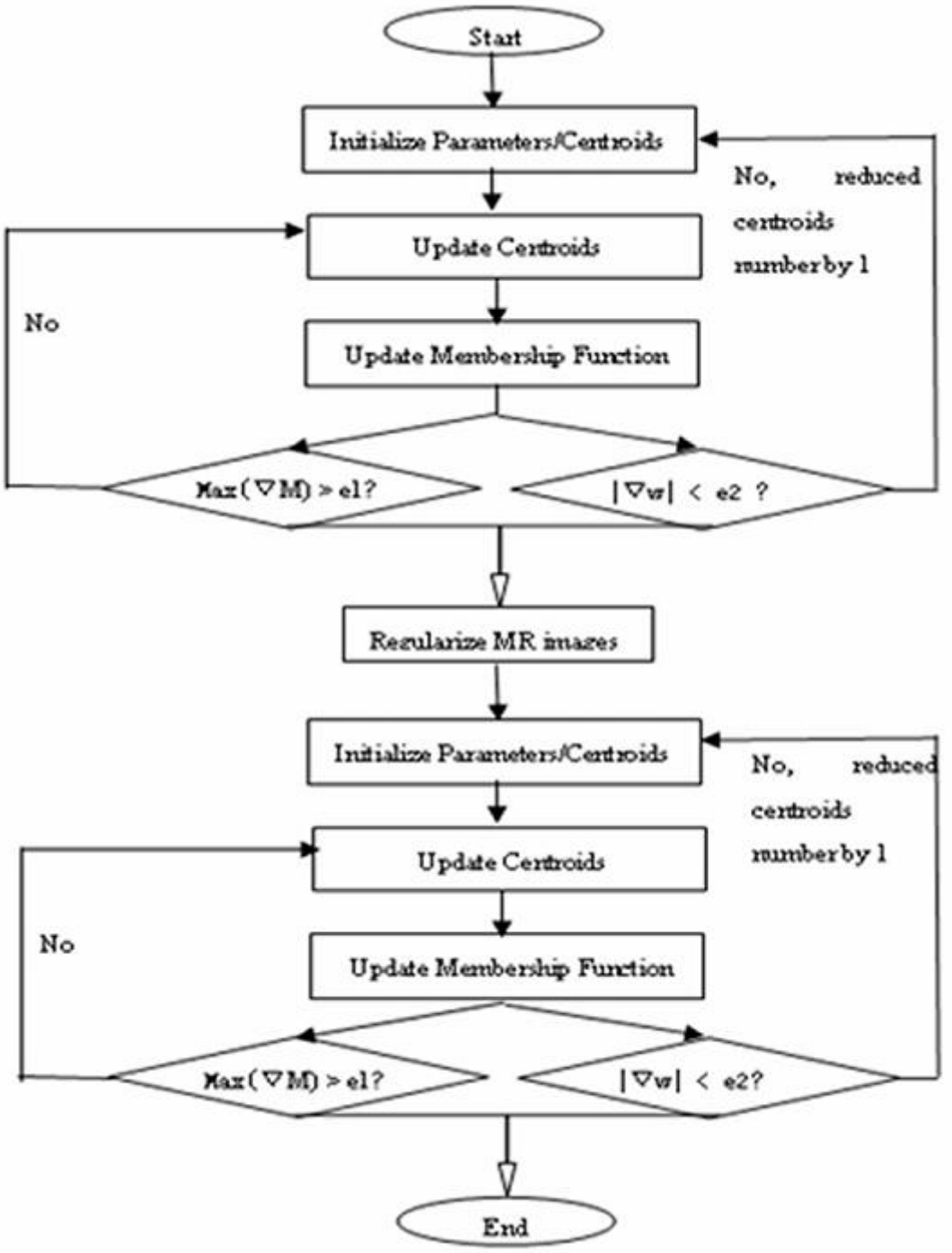

Figure 17: Flow chart of the regularized SPFCM algorithm.

drawback of this approach lies in the fact that reference scans are needed for all the imaging parameter sets. Moreover, the field inhomogeneity pattern differs, in general, between the reference and subject scans because of their coil loading difference. Another commonly used technique in practice is homomorphic filtering [12, 45]. This approach, despite comparative ease of use, was reported to worsen the classification in some cases [12]. Several authors proposed a polynomial fitting based inhomogeneity correction algorithm [64, 92]. Wells et al. [103] reported an adaptive classification algorithm based on a combination of EM algorithm and iterative homomorphic filtering, which corrects inhomogeneity better than its precursors. The adaptive fuzzy c-means algorithm proposed by Pham and Prince [73], which models the inhomogeneity field as a slowly varying field, reduces the inhomogeneity effect on fuzzy c-means clustering. This method gives promising results, but the necessity of solving an elliptic PDE greatly increases the processing time. In addition, small, local intensity variations appear abruptly in the images, contradicting the assumption that inhomogeneity is changing slowly. More importantly, this technique does not have a unique solution and may converge to non-optimal solutions. An alternative approach in correcting inhomogeneity in FCM, proposed by Zhu and Jiang [111], alleviates the intensity variation problem by doing segmentation/classification in unoverlapped sub-regions in the images and fusing the results based on the intensity deviation of each sub-region. In this method, estimation of the weighting factor when fusing the sub-regions is still an unsolved issue.

In this thesis, we developed a novel MAp Guided Intensity Correction (MAGIC) FCM algorithm which shows promise in dealing with the intensity variation problem in FCM clustering. The idea of this technique is based on constructing an adaptive field that reflects the intensity variations in MR images with intensity non-uniformity. This estimated intensity variation field is then subtracted from the corrupted image to recover the original image and facilitate the classification.

5.2.3.1 Intensity Variation Field Modeling

It has been shown by previous research that the inhomogeneity in MR images can be modeled as a slowly varying, multiplicative field. Since the multiplicative field can be changed

to additive by simply taking a logarithm transformation, the following discussion first assumes the additive field, and then extends the method to a multiplicative field assumption on the corrupted image. Furthermore, we model this field as comprised of a local intensity variation part and a global intensity variation (inhomogeneity) part.

The global intensity variation mainly refers to the stationary and radio frequency (RF) magnetic field inhomogeneity that corrupts the whole image and is spatially variant. On the other hand, the local intensity variation reflects the more unpredictable intensity corruption that is only locally dependent, including noise, PVE, ghosting etc.

Following assumptions of previous research, the MR images corrupted by intensity variations are assumed as follows:

$$I_{corrupted} = I_{original} \cdot G + L \tag{30}$$

, where $I_{corrupted}$ symbolizes the corrupted image, G is the global inhomogeneity, $I_{original}$ is the original image and L symbolizes the local intensity variations. This model can be reformulated as

$$I_{corrupted} = (I_{original} + L') \cdot G \tag{31}$$

Following a simple logarithm transformation, the equation is then expressed to be

$$\ln I_{corrupted} = \ln(I_{original} + L') + \ln G \tag{32}$$

To recover the original image, the global inhomogeneity can be removed first, and then the result can be exponentially transformed so that the local intensity variations can be removed in a similar fashion. Therefore, both the global and local intensity variation fields can be removed in an additive means. An additive global intensity variation cases is shown in Figure 18 to symbolize the relationship. Multiplicative case can be adapted in a similar manner following previous discussions.

Based on this corrupted model, a process that counteracts the corruption is proposed in the present study to include an intensity variation adaptation in the intensity-based classification techniques in order to generate correct results. Specifically, we include an intensity adaptation map that is proportional to the intensity variations yet has opposite signs in the classification process to counteract the corruption process.

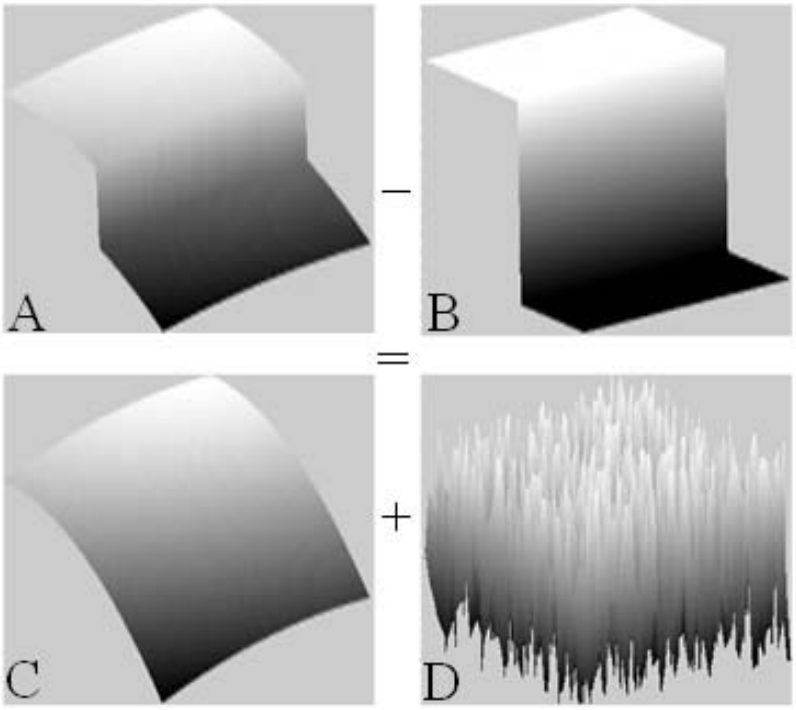

Figure 18: Relationship between original image, corrupted image, local intensity variation and global intensity variation. The difference between corrupted image (A) and original image (B) can be viewed as a global intensity variation (C) plus a local intensity variation field (D).

5.2.3.2 MAGIC-FCM Objective Function

Based on the adaptive field modeling, we introduced additional terms to the basic form of SPFCM classification to achieve the goal of correcting intensity variations. Specifically, the following objective function was proposed to be minimized:

$$J_{MAGIC-FCM} = \sum_{j=1}^{c}\sum_{i=1}^{n} M_{i,j}^{m}\|x_i - w_j - v_i\|^2 + \alpha\sum_{j=1}^{c}\sum_{i=1}^{n} M_{i,j}^{m}$$

$$\sum_{t=1\ldots c, t\neq j}\ \sum_{l\in Neighbor(i)} M_{l,t}^{m} + \eta\sum_{i=1}^{n}\|\nabla\underline{x_i} - \nabla\underline{v_i}\|^2 + \lambda\sum_{i=1}^{n}\|v_i\|^2 + \gamma\sum_{i=1}^{n}\|\Delta v_i\|^2 \qquad (33)$$

Here, v_i is the intensity adaptive factor for pixel i. Adaptive factors of all pixels comprise an adaptive surface that counteracts the intensity variation. η is a constant restricts adaptive surface, λ is the dwelling force term that settles the adaptive surface, and γ assigns the weighting of the smoothness in the adaptive surface.

The first term of the function is a modified version of the traditional FCM objective function, which groups the pixels according to their intensity similarity with adaptation to intensity variation. In this term, the adaptive factor v_i helps to counteract the intensity deviation from the expected value. The second term, introduced in the above section, makes the FCM more noise resistive. The third term constricts the gradients of the adaptive surface ($\nabla \underline{v_i}$) to be similar to the treated gradient field of the original image ($\nabla \underline{x_i}$). With this restriction, the desired adaptive field can be constructed. In the application of intensity variation removal, the expected adaptive field is low frequency dominated which means only small gradients in the original image should be reflected in the adaptive field. To achieve this goal, the gradient field of the original image can be treated in multiple ways that will be discussed later. The adaptive surface, restricted by term three, however, does not have a mathematically unique solution. Because of this, the fourth term is added so that an optimal solution can be found. Another more important purpose this term serves is to differentiate between the local and global intensity variations. The last term in the objective function minimizes the Laplacian of the adaptive field. This term serves the purpose of making the adaptive field piecewise continuous.

In practice, an eight-directional gradient is used in the third term. It is defined at each pixel as the summation of the intensity differences between the current pixel and each of its eight neighborhood pixels. Theoretically, this term restricts the contrast of the adaptive field to be the same as the image. This can be understood by assuming an arbitrary pixel x in the original image and its corresponding pixel x' in the adaptive surface. Without losing generality, the following relationship is assumed: $x = x' + c$, where c is a constant. Since the objective function restricts the gradient from pixel x to its eight neighborhood Ω same as those of pixel x', Equation (34) holds.

$$i_{x \in \Omega(x)} = i'_{x' \in \Omega(x)} + c \tag{34}$$

Following this analysis, the adaptive field equals to the original image plus a constant value. By treating the gradient filed of the original image, the abrupt change in gradient, mainly caused by edge, is not reflected in the adaptive surface. A one-dimensional example

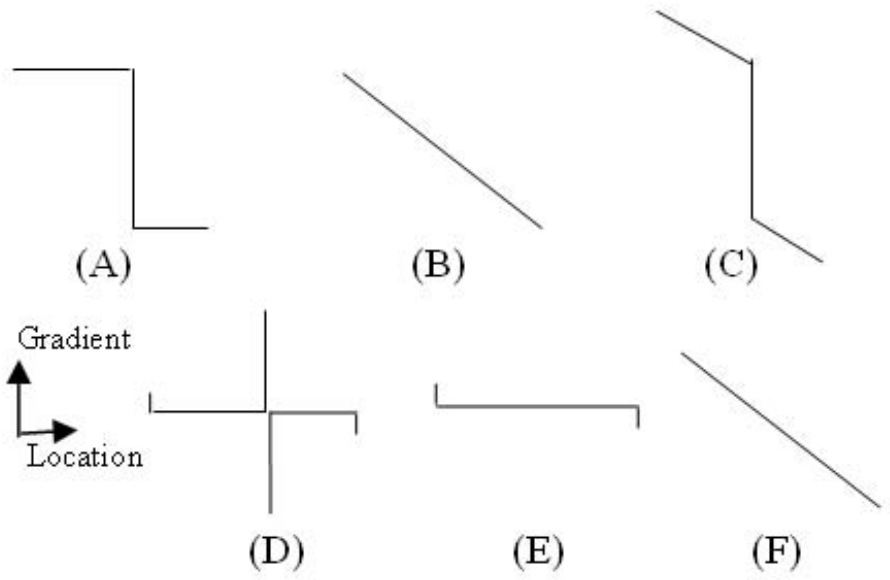

Figure 19: One dimensional example illustrating MAGIC intensity variation correction. (A) original image, (B) intensity variation field, (C) corrupted image by adding (B) to (A), (D) two dimensional gradient field of (C), (E) thresholded gradient field and (F) estimated gradient field using term 3 of MAGIC-FCM.

is shown in Figure 19 to help understand this. Here, we assume a one dimensional corrupted image (C) resulting from the summation of (A) and (B); (D) is the gradient field of (C), which is defined by $v_i = (v_i - v_{i-1}) + (v_i - v_{i+1})$; (E) is the thresholded version of (D); and (F) is the estimated intensity variation based on (E) using the third term in the MAGIC-FCM objective function.

This restriction, however, does not yield a unique solution, since constant c can be any real number. The dwelling term helps to settle the surface to an optimal solution, which makes the mean value of the adaptive field, theoretically, equal to zero.

In the same fashion, the second order derivative in the fifth term is defined as the second order eight-directional derivative. Based on this, Equation (33) is reformulated as Equation (35).

$$J_{MAGIC-FCM} = \sum_{j=1}^{c}\sum_{i=1}^{n} M_{i,j}^{m}\|x_i - w_j - v_i\|^2 + \alpha \sum_{j=1}^{c}\sum_{i=1}^{n} M_{i,j}^{m} \sum_{t=1\ldots c, t\neq j} \sum_{l\in Neighbor(i)} M_{l,t}^{m} +$$

$$\eta \sum_{i=1}^{n} \sum_{k \in \Omega} \|(x_i - x_k) - (v_i - v_k)\|^2 + \lambda \sum_{i=1}^{n} \|v_i\|^2 + \frac{\gamma}{9} trace(\|A * V_i\|^2) \tag{35}$$

In this equation, V_i is the matrix form of the adaptive surface; and matrix A is calculated as

$$A = \begin{bmatrix} -0.125 & -0.25 & -0.375 & -0.25 & -0.125 \\ -0.25 & 1.75 & 1.5 & 1.75 & -0.25 \\ -0.375 & 1.5 & -9 & 1.5 & -0.375 \\ -0.25 & 1.75 & 1.5 & 1.75 & -0.25 \\ -0.125 & -0.25 & -0.375 & -0.25 & -0.125 \end{bmatrix} \tag{36}$$

The combination of the last three terms, namely MAGIC terms, has basically two configurations. On one hand, when the ratio of λ to η is comparatively large and γ is zero, this MAGIC part reflects local intensity variations yet penalizes global intensity inhomogeneity and primary image information. This is because local intensity variations have a higher cumulative sum of the L2 norm (the fourth term of MAGIC-FCM) than those of the 8-directional gradient between corrupted image and adaptive surface. As a result, the adaptive surface only reflects the local intensity variations. On the other hand, when the ratio of λ to η is small and a weighting is assigned to smoothness factor γ, the adaptive surface is able to reflect both global and local intensity variations. In such a case, nearly no information is left when subtracting this adaptive field from the corrupted image. Therefore, treatment is needed for the 8-directional gradient field of the corrupt image in order to neglect the edge in the adaptive surface. A simple way of treating the gradient field is to suppress (threshold) large gradients so that the edge is not reflected. Alternatively, some advanced edge detection algorithm can be used to suppress the gradient only at the detected edge regions. A detailed description about gradient field treatment will be discussed later in the following sessions.

Similar to FCM/SPFCM minimization, by taking the partial derivative of the MAGIC-FCM objective function with respect to w_j, v_i and $M_{i,j}$ under the constraint that the membership of each pixel is summed to one, we can find a numerical scheme for updating the centroids, adaptive surface and the membership function. The updating process can be terminated at specific convergence criteria.

5.2.3.3 Numeric Derivation

Minimization of the objective function needs evaluation of the membership function, centroids and adaptive field following a gradient descent procedure. Since the total pixel number is limited, the objective function ensures the existence of a global minimum. Similar to FCM/SPFCM, the MAGIC-FCM may converge to a non-optimized local minimum for its seed-dependent property.

Similar to Equation (21), the membership function can be derived with the following PDE.

$$\frac{\partial J_{MAGIC-FCM}}{\partial M_{i,j}} + \sum_{i \in \Omega} \lambda_i (1 - \sum_{j=1}^{c} M_{i,j}) = 0 \tag{37}$$

Solving Equation (37), the numerical updating scheme for the membership function is found as follows.

$$M_{i,j} = \frac{(\|x_i - w_j - v_i\|^2 + \alpha \sum_{t=1...c, t \neq j} \sum_{l \in Neighbor(i)} M_{l,t}^m)^{\frac{1}{1-m}}}{\sum_{k=1}^{c} (\|x_i - w_k - v_i\|^2 + \alpha \sum_{t=1...c, t \neq k} \sum_{l \in Neighbor(i)} M_{l,t}^m)^{\frac{1}{1-m}}} \tag{38}$$

The centroid is solved by solving the PDE of Equation (39) and is shown in Equation (40).

$$\frac{\partial J_{MAGIC-FCM}}{\partial w_j} = 0 \tag{39}$$

$$w_j = \frac{\sum_{i=1}^{n} M_{i,j}^m (x_i - v_i)}{\sum_{i=1}^{n} M_{i,j}^m} \tag{40}$$

The last parameter that needs to be updated is the adaptive surface. This is done by taking the partial derivative of $J_{MAGIC-FCM}$ with respect to v_i.

$$\frac{\partial J_{MAGIC-FCM}}{\partial v_i} = 0 \tag{41}$$

The solution is shown in Equation (42).

$$v_i = \frac{\eta \sum_{k \in \omega} (v_k + x_i - x_k) + \gamma \sum_{t \in \Psi} (b_t v_t) + \sum_{j=1}^{c} M_{i,j}^m (x_i - w_i)}{\eta + 8\lambda + 9\gamma + \sum_{j=1}^{c} M_{i,j}^m} \tag{42}$$

Here, Ψ symbolizes the 5 by 5 pixel matrix around pixel i, and b is the weighting factor. The weights for these neighboring pixels are the same as those specified in Equation (36), with zero weighting of the center pixel. As mentioned above, a global minimum exists for the objective function, and the numerical scheme provided here ensures convergence.

5.2.3.4 MAGIC-FCM Algorithm

A major difficulty in minimizing the proposed MAGIC-FCM objective function is the adjustment of parameters. The complicated form of the objective function also worsens the local minimum problem. In practice, all these can be circumvented by fulfilling the objective function in two steps, which increases the flexibility in applying the MAGIC-FCM algorithm.

Reformulating the objective function (33), the MAGIC-FCM function can be broken down into two parts:

$$J_{MAGIC-FCM} = J_{MAGIC} + J_{SPFCM} \tag{43}$$

, where J_{SPFCM} is the same as described previously and J_{MAGIC} equals

$$J_{MAGIC} = \eta \sum_{i=1}^{n} \|\nabla \underline{x_i} - \nabla \underline{v_i}\|^2 + \lambda \sum_{i=1}^{n} \|v_i\|^2 + \gamma \sum_{i=1}^{n} \|\Delta v_i\|^2 \tag{44}$$

Specifically, MAGIC-FCM is more likely to achieve ideal classification if J_{MAGIC} and J_{SPFCM} are minimized sequentially. In this sense, the first function works as a preprocessing step for intensity variation correction and the second step becomes the fuzzy c-means algorithm with spatial penalization. The separation, at the same time, enables the application of MAGIC algorithm in other image processing tasks as well. The two objective functions are minimized in the same fashion as Equation (33).

The detailed SPFCM algorithm can be referred to previous sections. For MAGIC, since global and local intensity variations are manifested differently in the corrupted image, they

need to be removed separately. First, we will describe how to use the MAGIC algorithm to remove the global intensity variations. As already mentioned, gradient fields need to be treated in order to keep the edge information in this configuration.

The easiest way to treat the gradient field to make it only reflected global inhomogeneity is to threshold the eight-directional gradient field. The thresholding, for an additive inhomogeneity field, is performed in the manner that the gradients in all directions that are greater than the threshold are replaced by zeros. Gradients that have been replaced with zeros, it is given smaller weighting than those below the threshold. In our application, only one tenth of the weighting for untouched gradients were assigned to the replaced zeros.

When the inhomogeneity is multiplicative, the logarithm transformation can be performed on the corrupted image to make it additive. Since this is a non-linear transformation, the thresholding has to be non-linear as well. Different from linear thresholding, the nonlinear thresholding depends on the intensity of the pixel. For a pixel with intensity i in the corrupted image, if the linear threshold is set to be th, the nonlinear thresholding will have a lower threshold of $\ln(i-th)-\ln(i)$ and an upper threshold of $\ln(i+th)-\ln(i)$. Despite the theoretical soundness of such an approach, it may introduce additional difficulties to the proposed algorithm because the gradient field resulting from this process makes the gradient field at lower intensity be given more addresses than those at high intensity. This can be easily understood by a trivial example of comparing $a = \ln(2) - \ln(1)$ and $b = \ln(255) - \ln(254)$. Clearly, $a = 0.6931 >> b = 0.0039$. As a result, numerical solution becomes highly unsatisfactory.

To overcome this difficulty, an alternative approach was proposed for the multiplicative field case. In the first step, the global intensity variation field is estimated purely based on an adaptive field assumption. Then, the multiplicative version of this field is calculated by dividing the corrupted image by the corrected image. In this multiplicative field, there is a constant displacement ζ at the boundaries between different tissue types. These discontinuities, corresponding to the points where the gradients have been set to zero in the first step, can be removed following the same procedure in step one by replacing the gradient field at these discontinuities with zero. This ensures that the constant offsets in the multiplicative

field are removed.

After the MAGIC process, only contrast lower than the threshold is reflected in the adaptive surface. To avoid the discontinuity of the adaptive surface, a weighting is assigned to the smoothness (the third term in J_{MAGIC}) so that the adaptive surface is piecewise continuous.

Another approach to preserve the edge and small features in the global variation removal process can be done with the aid of an edge detection algorithm such as the canny edge detector [24]. This kind of optimized edge detector best separates edges from noise. We can just null the gradients at edge locations identified by this kind of edge detector. Detailed treatment can be realized in 3 steps:

1. Calculate the edgemap using the canny edge detector.

2. Dilate the edgemap by one to ensure the edge region is covered.

3. Calculate from this edgemap where in all 8-directional gradient fields the gradient should set to zero. This is done by taking the expanded edgemap as an image and calculating its 8-directional field. The identified non-zero points in the gradient field along with those in the edgemap are the calculated edge locations in the original image.

Although a canny edge detector is used here, other edge detectors can be applied in the same spirit. It should be noted that this process may not generate satisfactory results for images with too many boundaries because of the information loss resulting from a dilated edgemap.

In removing the local intensity variations, a high η value is assigned to the MAGIC equation to penalize the image information and global inhomogeneity. Under this configuration, it is not necessary to treat the gradient field. The previously mentioned edge detector-based nulling scheme, however, can be combined to the local intensity variation removal process to better keep the edges and small features while removing local intensity variations.

After the above theoretical analysis, we can derive the updating scheme of Equation

(44) based on a gradient descend technique, which yields:

$$v_i = \frac{\eta \sum_{k \in \omega} (v_k + x_i - x_k) + \gamma \sum_{t \in \Psi} (b_t v_t)}{\eta + 8\lambda + 9\gamma} \tag{45}$$

Iterating Equation (45), an adaptive surface with intensity variation estimation can be constructed.

The detailed MAGIC-FCM algorithm to remove both local and global intensity variations is described as follows. Although both global and local variations removals were included in the algorithm, they can be performed separately.

1. Initialize parameters, centroids, membership function and adaptive surface.

2. Set λ to be zero, η, γ to be specified values, and then iterate Equation (45) on the corrupted image with thresholded/treated gradient field until convergence. Although there is no unique solution theoretically for the objective function, numerically it does yield the closest optimal solution to the initial adaptive surface. This step estimates the global inhomogeneity. For multiplicative intensity variation fields, the multiplicative field is estimated by dividing corrupted image to corrupted image minus estimated additive field. The discontinuities in this multiplicative field are removed by taking the multiplicative back to the MAGIC function with proper settings of parameters and treated gradient field, which is simply retrieved by nulling the gradients at locations that were set to zero during the additive field estimation.

3. Subtract/divide (additive/multiplicative field assumption) the global adaptive surface from the corrupted image and estimate the local intensity variation using Equation (45). The field may be treated with an edge detect algorithm such as canny; γ is set to be zero; and a high ratio of λ to η is chosen to reflect the local intensity variation but suppress small features and edges in the adaptive surface.

4. Remove the global and local intensity variation adaptive surfaces from the corrupted image to recovered the original image.

5. Perform SPFCM as described previously.

6. Stop the algorithm when the maximum change in the membership functions of all pixels is smaller than the preset stopping factor e.

Since only the ratio of η to λ and γ affects the MAGIC result, η can be set to be 1 all the time. The value λ, when chosen to be zero in estimating the global inhomogeneity, has a slow convergence rate. To speed up processing, the algorithm can be applied to the down-sampled version of the corrupted image. The final global adaptive surface is then acquired by up-sampling the estimated result back to original size. This treatment increases the processing efficacy and seldom degrades the performance of the MAGIC algorithm since the global intensity variation is a slowly changing field with no abrupt changes.

In local adaptive surface estimation, the big value of λ accelerates the convergence, so it completes in less than 20 steps in most cases.

5.2.3.5 Parameter Selection and Algorithm Initiation

In our application of the MAGIC-FCM algorithm, all the parameters were fixed. The fuzzification parameter m was set to 2. The selection of α, according to reference [72], can be evaluated based on a cross-validation scheme. Since MAGIC itself helps suppress noise, which is included in the local intensity variations a small value 10 (it is usually set to be around 200) was set for α. η was set to be 1 all the time; λ was set to be 5 for local intensity correction with edge nulling and 0 for global intensity correction; the smooth weighting γ was set to be 0.01 for additive field estimation. For multiplicative estimation, the smoothness factor was set to zero in the additive field estimation and 0.01 when retrieving the multiplicative field based on this additive field result.

The stopping criteria for MAGIC is fulfilled when the overall change of the adaptive surface is less than a preset threshold; while the stopping criteria for SPFCM is fulfilled when the maximum change of membership function is less than a specific value. In our application, the stopping factors chosen were 1 for local and additive global for the MAGIC step and 0.05 for the SPFCM step.

Initial selection of the adaptive surface is vital in the accuracy and efficacy of the MAGIC-FCM algorithm. For global intensity variations, the starting guess should have

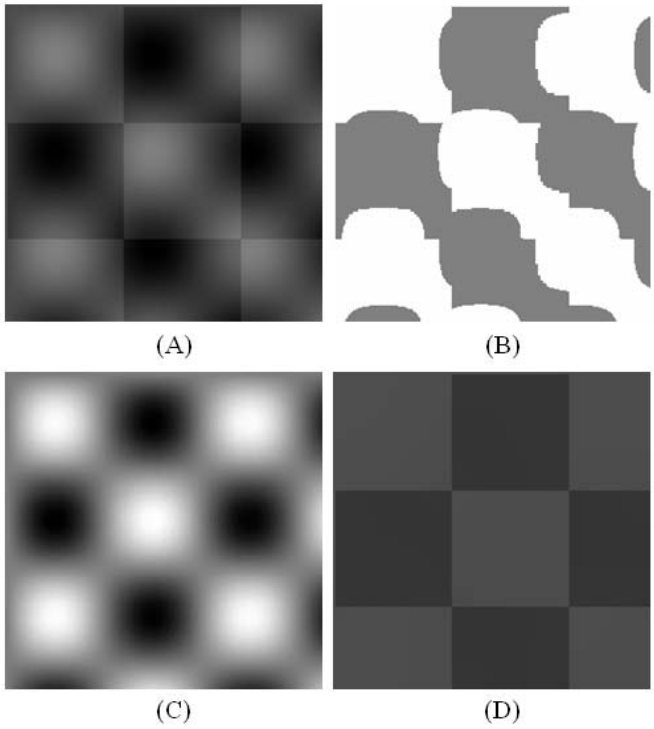

Figure 20: Application of MAGIC algorithm on sinusoidal inhomogeneity corrupted checker board image. (A) Corrupted image (B) FCM classified result (C) Estimated global intensity variation field using MAGIC (D) Recovered image.

similar contrast as the corrupted image. However, since the numerical solution of the adaptive surface has zero mean, the initial adaptive surface was chosen to be the corrupted image minus its mean value. For local intensity variations, the initial adaptive surface was chosen to be zero.

Initial centroids were chosen manually and initial membership estimation was calculated based on the following equation:

$$M_{i,j} = \frac{(\frac{1}{d_{i,j}^2})^{1/m-1}}{\sum_{j=1}^{c}(\frac{1}{d_{i,j}^2})^{1/m-1}} \tag{46}$$

, where $d_{i,j}$ is the Euclidean distance.

5.2.3.6 Performance of MAGIC-FCM

The performance of the MAGIC-FCM algorithm was first evaluated on a checker board image corrupted by sinusoidal intensity variations (Fig. 20). The images represent two

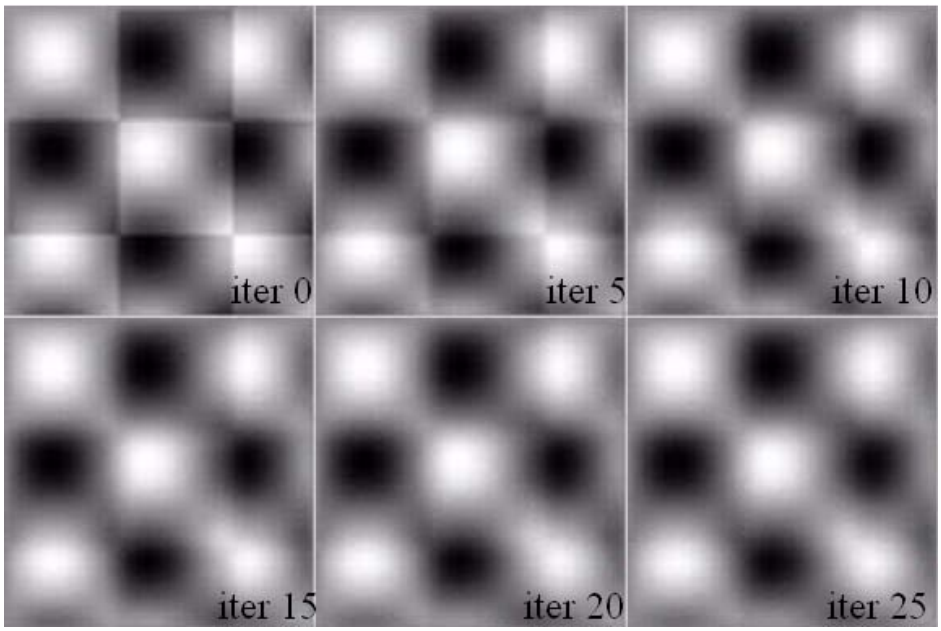

Figure 21: MAGIC estimation of the inhomogeneity field of the corrupted image shown in Figure 20.

tissue classes with different intensities. The two tissues, originally separated perfectly were corrupted by additive sinusoidal field. This was done by an adding specific sinusoidal fields to the original images. There are no local intensity variations in the images, so only step 2 in the MAGIC-FCM algorithm was used to remove the global inhomogeneity. These two images were constructed so that it is difficult for a homomorphic filter to correct the inhomogeneity. SPFCM classification is shown in Figure 20(B); (C) shows the estimated global intensity variation by the MAGIC procedure and the final MAGIC recovered image is shown in Figure 20(D). It is can be readily appreciated that the inhomogeneity field is removed completely by subtracting (C) from (A). The SPFCM classification on the recovered image (D) then becomes trivial.

The estimation of the inhomogeneity field in this case took less than 50 iterations. The estimation process of the inhomogeneity field is illustrated in Figure 21.

MAGIC-FCM algorithm was tested on another synthetic corrupted image shown in Figure 22(A). The SPFCM result is shown in (B). The estimated adaptive surface and classified result by MAGIC-FCM are shown in (C) and (D), respectively. In Figure 22(C), the sinusoidal field running from head to bottom can be readily inspected. From these

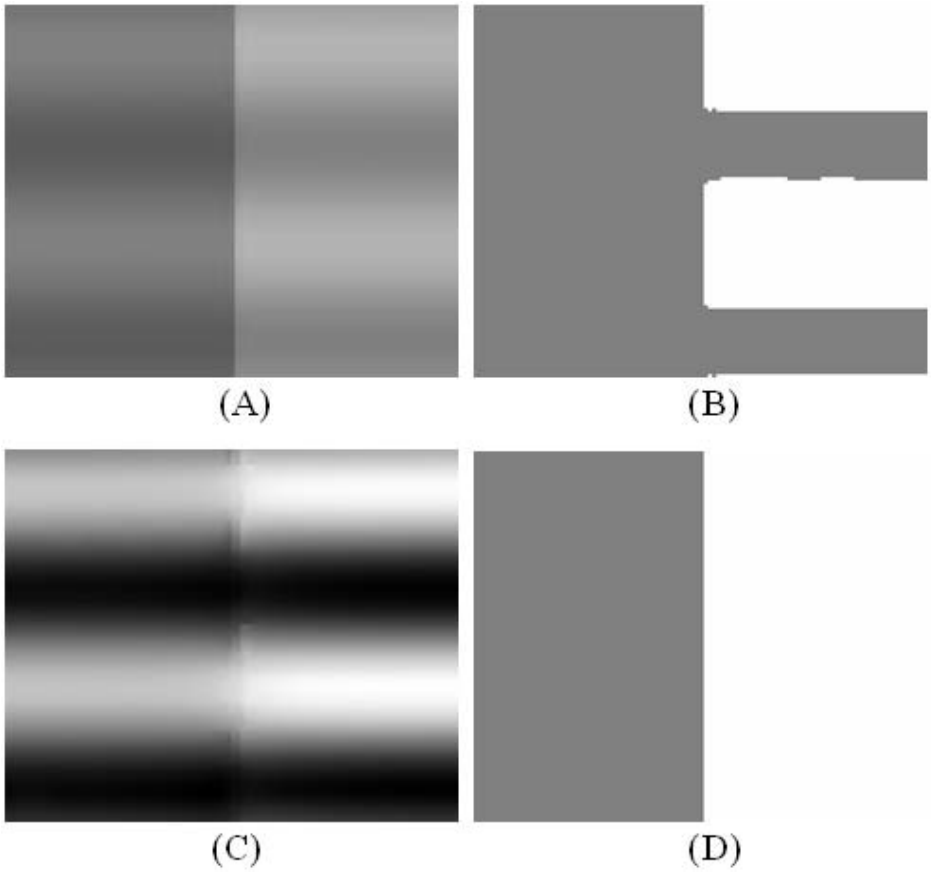

Figure 22: Comparison of MAGIC-FCM and SPFCM classification results on sinusoidal inhomogeneity corrupted image. (A) Corrupted image (B) SPFCM classified result (C) Estimated global intensity variation field using MAGIC (D) Classified result from MAGIC-FCM.

two ideal examples with different patterns of intensity variations, we showed the ability of the MAGIC procedure in restoring the original images and then facilitating SPFCM classification.

To quantitatively evaluate the performance of MAGIC-FCM on MR images, the ground truth of the corrupted image has to be known. This can be facilitated by the brain MRIs obtained from simulated brain database at the McConnell Brain Imaging Center of the Montreal Neurological Institute, McGill University [50]. The advantage of using this database is that the prototypical model of the simulated brain is known and the inhomogeneity level and noise level, acquired from real MR images, are adjustable.

The noise in the simulated images has Rayleigh statistics in the background and Rician

statistics in the signal regions. Noise level is defined by percent ratio of the standard deviation of the white Gaussian noise versus the signal for a reference tissue. The inhomogeneity field is modeled as multiplicative, and its level is defined as the ratio of variation range to one, e.g. 40% inhomogeneity means the pixel intensity can be multiplied by a factor of 0.8 to 1.2.

First, we test MAGIC-FCM on a degraded T1 weighted image (60% inhomogeneity, 3% noise) for both additive and multiplicative assumptions shown in Figure 23.

It is clearly visualized that the intensity variations existing in the corrupted image are removed by the MAGIC correction based on both of these two assumptions. This can be also seen from the histograms shown. Before MAGIC correction, the white matter and gray matter form a broad peak in the histogram. This peak splits into two after the MAGIC correction, which facilitates the classification. The misclassification region pointed by the white arrow shown in Figure 23(F) is corrected in both multiplicative (G) and additive (H) MAGIC-FCM. However, in the additive field assumption, additional intensity error was introduced and some part of the CSF region was classified as the background (pointed by dark arrow in Fig. 23(H)). This is caused by the constant offsets between tissue boundaries. Since in the simulated brain images, the inhomogeneities were introduced by the multiplicative model, this misclassification is expected.

The MAGIC step, comparing with most previous inhomogeneity correction methods, has the advantage of being able to suppress local intensity variations including noise. In the following example shown in Figure 24, we performed MAGIC along with two successful and widely used inhomogeneity correction methods N3 [85] and Entropy Minimization on a simulated brain image corrupted by 60% inhomogeneity and 10% noise. All these corrected images were then SPFCM classified and compared.

Since MAGIC corrects both global and local (here it is only noise) intensity variations, it yields better classification results than the classification results of the image after N3 and Entropy Minimization correction, visually. Comparable performance was acquired for N3 correction when an edge-preserving anisotropic filtering was applied to the N3 corrected result prior to the classification.

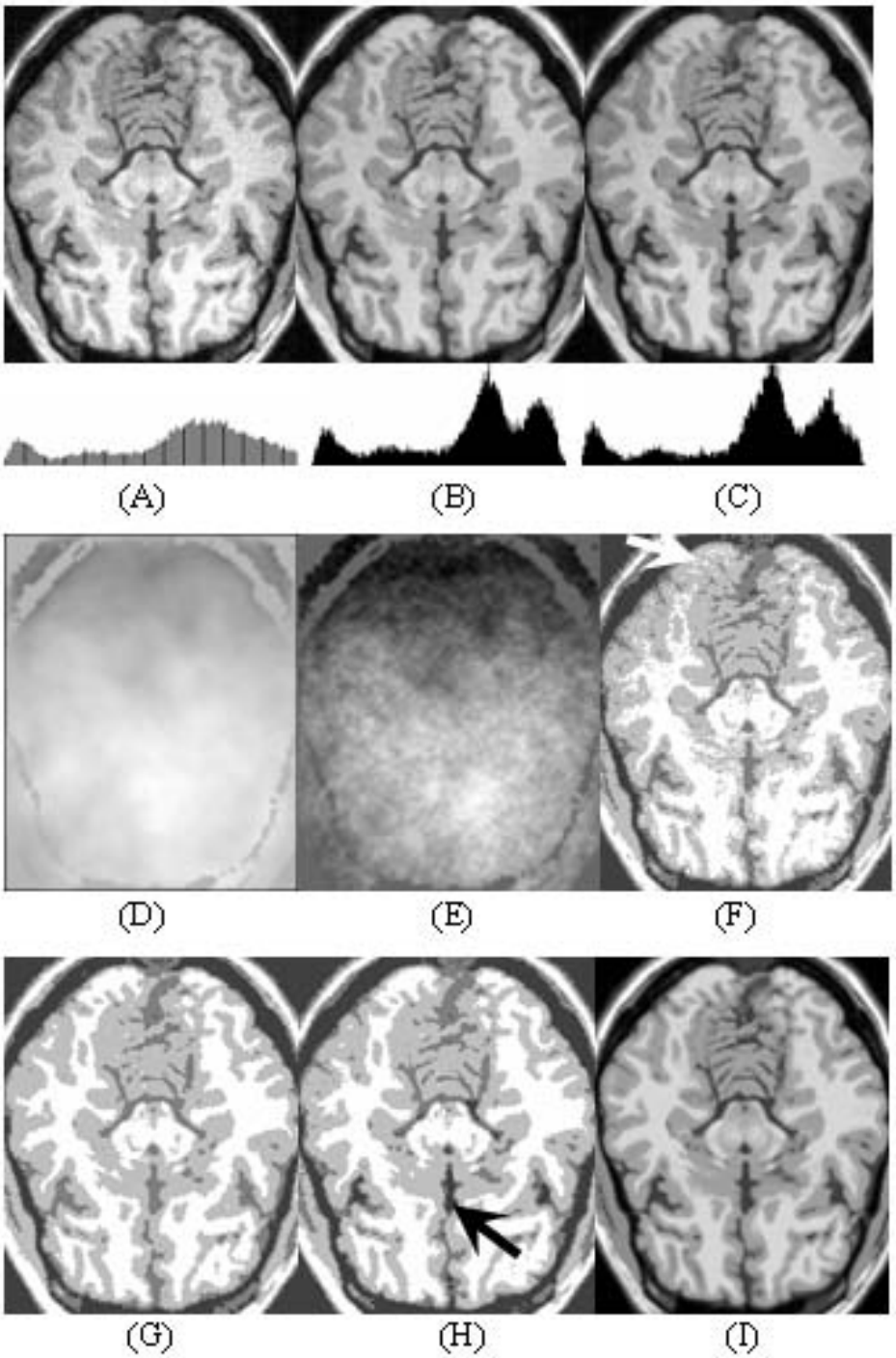

Figure 23: MAGIC-FCM on T1 weighted simulated brain image based on both multiplicative and additive inhomogeneity assumptions. (A) Corrupted, (B) MAGIC corrected based on multiplicative inhomogeneity assumption, and (C) MAGIC corrected image based on additive inhomogeneity assumption images with histogram. (D) and (E) show the estimated multiplicative and additive adaptive surfaces, respectively. (F), (G) and (H) show the classification results from the FCM, MAGIC-FCM (multiplicative) and MAGIC-FCM (additive) algorithms, respectively. Arrows show misclassification region. (I) shows the noise and inhomogeneity free phantom model.

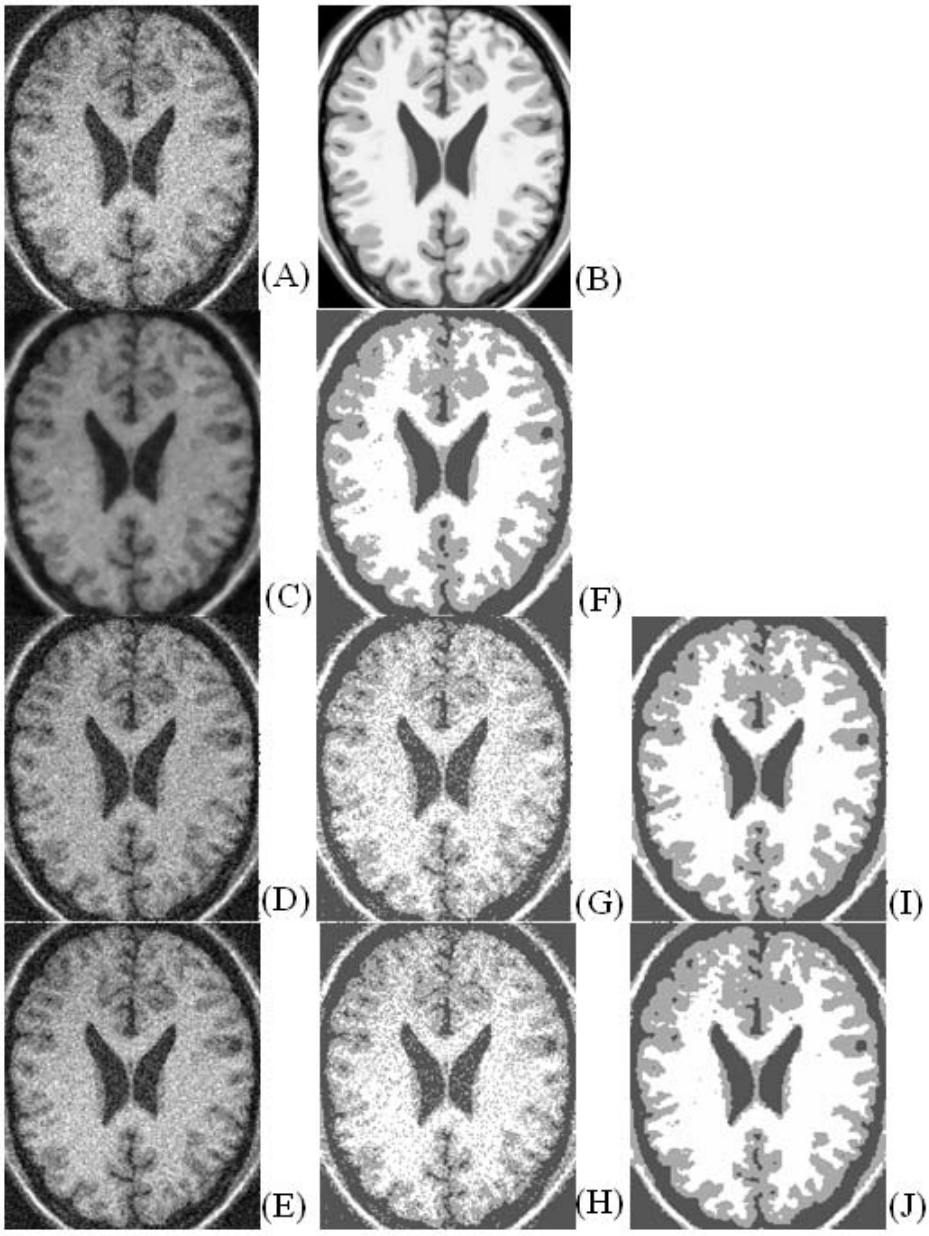

Figure 24: Comparison of MAGIC-FCM with N3 and Entropy Minimization algorithms in intensity variation correction on T1 weighted simulated brain image. (A) Corrupted and (B) Uncorrupted images; (C) MAGIC corrected, (D) N3 corrected and (E) Entropy Minimization corrected images. (F), (G) and (H) are SPFCM results of (C), (D) and (E), respectively. (D) and (E) were then anisotropically filtered to denoise, classified using SPFCM and shown in (I) and (J), respectively.

Table 4: Misclassification Rate of White Matter for SPFCM and MAGIC-FCM

Inhomogeneity	**Noise**	**Misclassification Rate**	
		SPFCM	**MAGIC-FCM**
20%	1%	2.7	1.8
	3%	4.2	3.2
	5%	5.9	5.7
	7%	9.5	7.4
	9%	15.7	8.4
40%	1%	5.4	2.1
	3%	6.5	4.0
	5%	8.5	6.5
	7%	10.6	7.8
	9%	16.5	8.7

In order to systematically evaluate the MAGIC-FCM under various conditions, the algorithm was tested on MR images with different corruption levels. In this example, we chose a simulated MR brain image corrupted by 20%-40% global intensity variation and 1%-9% noise (Fig. 25).

Misclassification rate, an evaluating criterion, is defined as the ratio of misclassified pixels to total number of pixels of this class. It is formulated in Equation (47).

$$e(i) = \frac{fp + fn}{n} \tag{47}$$

Here, $e(i)$ is the misclassification rate of tissue i; fp is the false positive responses (pixel belongs to tissue i but classified as other tissues); fn is the false negative responses (pixel doesn't belong to tissue i but classified as tissue type i) and n is the total number of pixels of tissue type i.

Limited by space, the classification results are not shown here. The performance of the MAGIC-FCM is summarized in Table 4, which listed the misclassification rate of white matter using both MAGIC-FCM and SPFCM algorithms. To simplify the comparison, defuzzification was performed prior to the calculation of the mislabeling rate. From the statistics in Table 4, one can see that MAGIC-FCM outperforms SPFCM, especially when the noise and inhomogeneity levels are high. In addition, MAGIC-FCM results appear to be

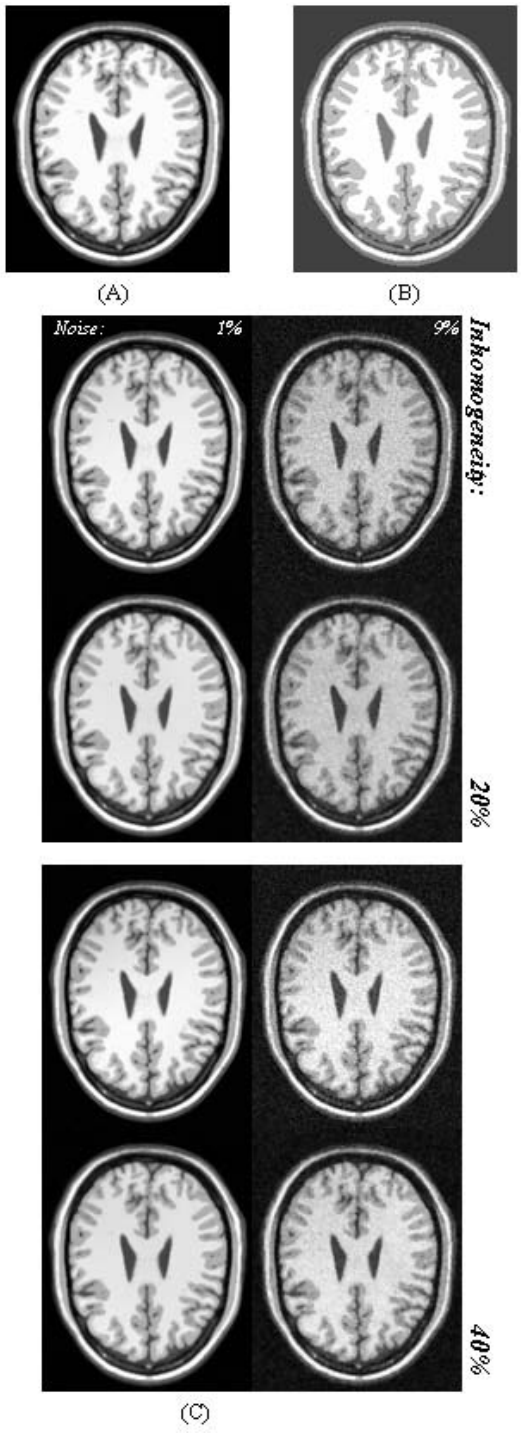

Figure 25: MAGIC correction of simulated brain image at different corruption levels. (A) Prototypical brain phantom. (B) SPFCM classification result of (A). (C) shows the corrupted version of (A) at 20%-40% inhomogeneity, 1%-9% noise (upper row) and MAGIC corrected results (lower row).

only slightly dependent on global inhomogeneity indicating the effectiveness of the MAGIC procedure in removing intensity inhomogeneity.

After quantitative evaluation of the MAGIC-FCM algorithm on simulated brain images, we applied it to the plaque images we acquired that were corrupted by intensity variations. Figure 26 presents a comparison of SPFCM and MAGIC-FCM classifications applied to two images acquired during the same scan. There are different patterns of intensity variations on the two images. In both cases, MAGIC-FCM gives results not deteriorated by intensity variations. Compared with the N3 algorithm, MAGIC correction appears to be more robust to the patterns of intensity variation field.

Local inhomogeneity, other than noise, also includes PVE and Gibbs ringing. These kinds of artifact are prevalent in high-resolution MR images. A case of this category is shown in Figure 27. In this example, edge-detector based gradient treating described in the methods section was performed in both global and local intensity variation removal procedures. It can be seen in 27(B) that some pixels belonging to hyperpiesia and fat (pointed by arrows) were misclassified. By comparing the FCM and MAGIC-FCM results in 27(B) and 27(F), it is demonstrated that the MAGIC process effectively removes the PVE and ringing artifact marked by the arrow signs.

In Figure 28, a T2 weighted plaque image was tested on both SPFCM and MAGIC-FCM algorithms. Despite significant inhomogeneity in the image, MAGIC-FCM was shown to be able to recover the image and to generate much better results than the SPFCM classification. The dark ring-like signal inside the vessel lumen comes from the cannula used for mounting the vessel.

5.2.3.7 Discussion and Conclusion

The MAGIC-FCM classification results on synthetic images, simulated brain images and high resolution vessel wall images demonstrate its ability to accurately segment MR images in the presence of field inhomogeneity. For multicontrast image classification, since the MAGIC procedure behaves as a preprocessing step, applying the MAGIC procedure to images of all contrast mechanisms helps ensure the correct classification using the SPFCM.

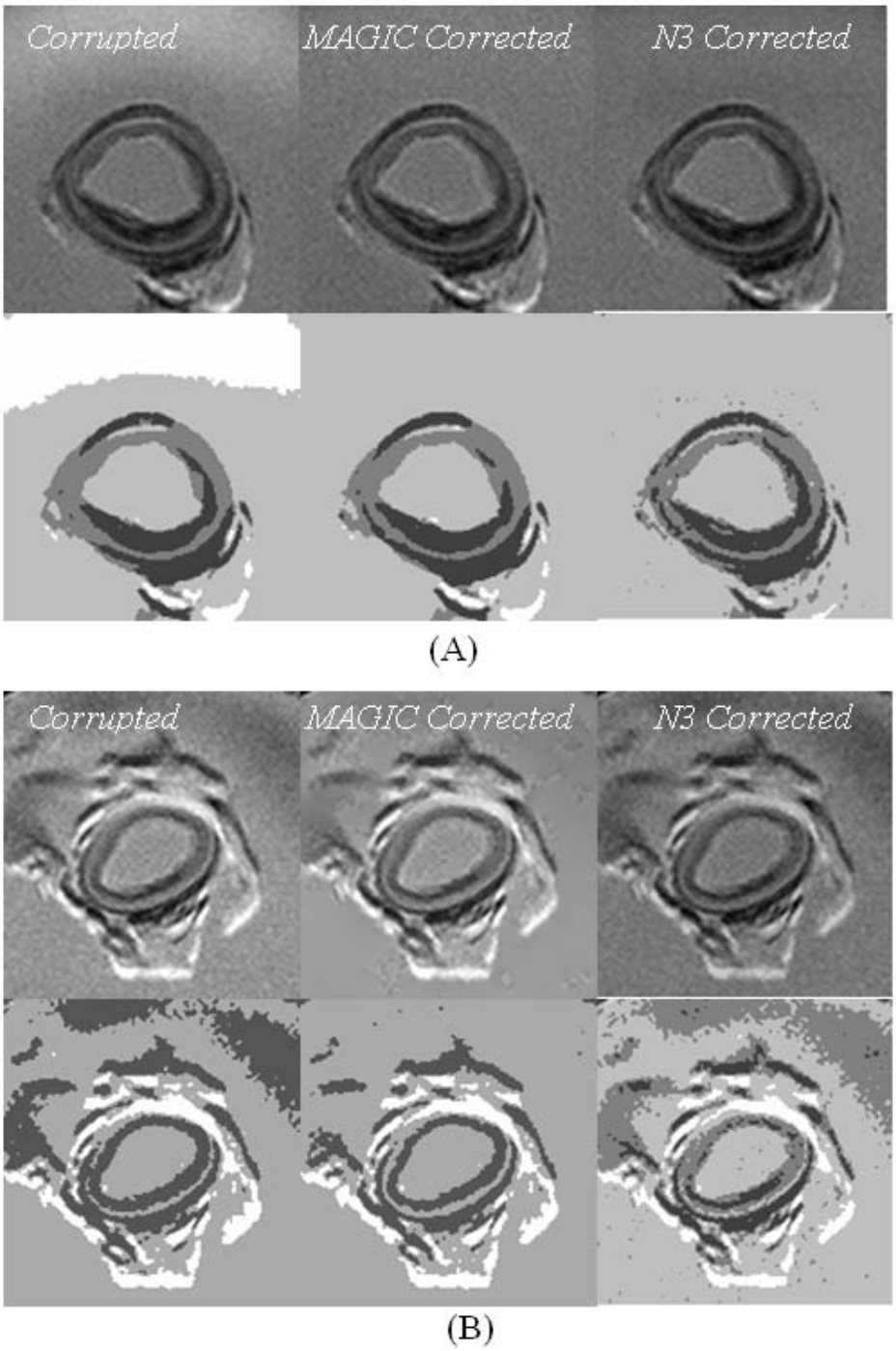

Figure 26: Comparison of MAGIC-FCM and SPFCM classification results on corrupted high resolution vessel wall images of different intensity variation patterns. (A) Corrupted, MAGIC corrected, N3 corrected images (upper row) and the corresponding SPFCM results. (B) Corrupted by another kind of intensity variation, MAGIC corrected, N3 corrected images (upper row) and the corresponding SPFCM results.

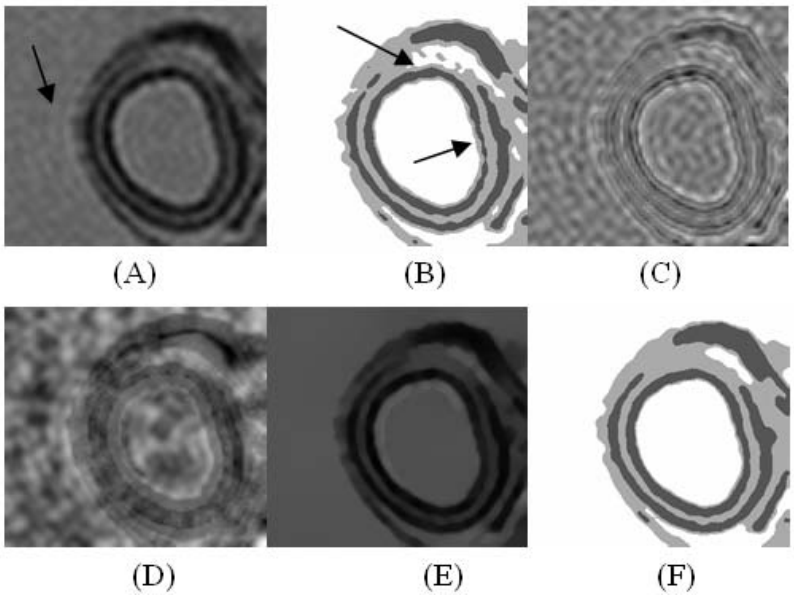

Figure 27: Comparison of MAGIC-FCM and FCM classification results on high resolution vessel wall image corrupted by global inhomogenneity, PVE and gibbs ringing. (A) Corrupted image, arrow shows the gibbs ringing artifact (B) SPFCM classified result, arrows show PVE (C) MAGIC estimated local intensity variation with the aid of edge detector (D) MAGIC estimated global intensity variation with the aid of edge detector (E) Recovered image (F) MAGIC-FCM result.

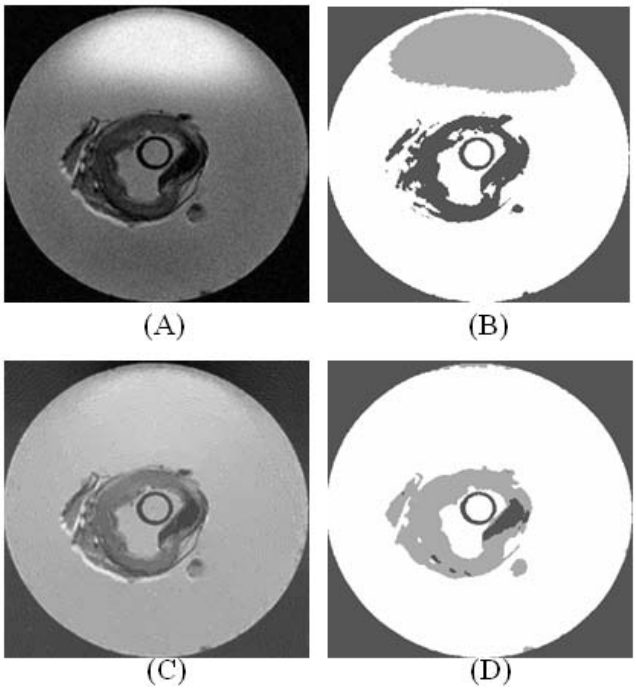

Figure 28: Comparison of MAGIC-FCM and FCM classification results on high resolution vessel wall image when huge amount of intensity variation is present. (A) Corrupted image; (B) FCM classified result; (C) Recovered image after MAGIC procedure; (D) Classified result from MAGIC-FCM.

The MAGIC-FCM algorithm was implemented on MATLAB (*Mathworks, Natick, MA USA*). Currently, for 181 by 217 images, performing the completed MAGIC-FCM algorithm (reduce to half the size when estimating global inhomogeneity) needs about 1 minute on Windows operating system installed a 2.0GHz Intel Pentium 4 CPU with 512Mb ram. This situation may be ameliorated with optimized code in compiled languages. Also, the increment in the down sampling rate in global inhomogeneity estimation can greatly speed up the processing time since most of the time is used in this step. Better numerical schemes provide additional possibilities in accelerating the algorithm. The key factor in determining the convergence rate of the MAGIC function is the size of the adaptive surface since every pixel on the surface depends on all other pixels. In this sense, adding control points, whose values can be fixed in the MAGIC calculation, in the adaptive surface is also a feasible means to accelerate the development of the adaptive surface.

In some of the cases, the MAGIC-FCM algorithm reduces the contrast between components. This is mainly caused by blurred edge appearance in the corrupted image. This, however, does not degrade the classification results in general. This problem can be avoided by setting a smaller threshold during gradient field treatment.

To conclude, MAGIC-FCM overcomes the misclassification issue encountered by FCM when segmenting inhomogeneity corrupted MR images. It is a promising technique for multicontrast MRI classification.

5.2.4 Summary

The FCM based clustering techniques developed in this section have been shown to be able to successfully classify/segment plaque components in the presence of noise (SPFCM) and inhomogeneity (MAGIC-FCM). The classification result of multicontrast MR images for a specific slice is a segmented image. Each tissue class in this image is assigned a characteristic intensity. The intensity levels are related to the final centroids of the classification and are insufficient by themselves to label the tissue types. The following section will focus on techniques that relying on additional information to label plaque constituents.

Table 5: Intensity Patterns of Typical Vessel Wall Components

	Calcification†	**Adipose Fat‡**	**Media**	**Fibrous**	**Necrotic Core**	**Fibrocellular**	**Fresh thrombus**
T1W	0	+++	+/-	-to+/-	-to+/-	+/-to+	-
T2W	0	++	+/-	-	-	+/-to+	-
PDW	0	+++	+/-	-	+/-to-	+/-to+	-
DWI	0	+++	+/-	+/-to-	+/-	+/-	-

†Calcification has nearly no MR signal.
‡Adipose fat appears to be the most hyper-intense region in all the images.
+, +/- and - were used to symbolize hyper-, iso- and hypo-intense signal.

5.3 Plaque Component Labeling

Accurate labeling of classification results is critical in plaque characterization. Generally speaking, specific patterns (e.g. intensity, contrast and etc.) for each tissue class need to be evaluated and recognized to identify its type. In manual plaque characterization, component labeling is based on tissues' comparative contrasts. For instance, calcium appears hypo-intense on MR images of all contrast, and fibrous tissue appears hypo-intense on proton density and T2 weighted images but iso-intense on T1 and diffusion weighted images. Although a single T2 weighted image can not positively separate calcium and fibrous tissues, the combination of intensity patterns on multicontrast MRI data offers enough information to differentiate the two tissues. The intensity patterns of plaque components on multicontrast MR images are usually listed in a table. Based on the MR images we acquired (see previous chapter) and previous research [27, 43, 83, 91], an intensity pattern table (Tab. 5) was constructed.

5.3.1 Automatic Plaque Labeling Employing Intensity Pattern Table

The majority of unsupervised plaque characterization techniques [27, 43, 83, 91] directly borrow the "intensity pattern table" approach used in manual labeling. Taking FCM based technique as an example, the resulting centroids for tissue clusters are labeled based on the logic in the intensity pattern table. The segmented clusters can then be labeled with regard

to their corresponding centroids.

5.3.1.1 Comparison of Multicontrast MRI on Fresh and Preserved Plaques Employing Intensity-Pattern-Table Labeling Based Characterization

As an extension of the comparison between fresh and preserved multicontrast MRI in chapter III, "intensity pattern table" labeling was used in combination with classification to characterize the multicontrast MR data acquired under both fresh and preserved conditions. SPFCM/MAGIC-FCM (when inhomogeneity exists) was applied first to classify the multicontrast MRI data. Then the resulting centroids were evaluated in order to assign proper tissue types to the classified clusters. Because of the mentioned variable intensity issue with thrombus, its characterization is done manually. Additionally, given the intensity similarity (as well as MR properties) between fibrous tissue and necrotic core (refer to Chapter IV), an additional logic is included in the labeling process to differentiate them: tissues adjacent to dense fibrous tissue or calcium were labeled as fibrous; otherwise, they were labeled as necrotic core. Manual segmentation was performed on the histological sections to provide references in evaluating the characterization results. Details about histological preparation can be referred to Chapter IV.

Figure 29 exhibits the characterization results of the multicontrast MRI shown in Figure 11. In this figure, characterization results for fresh scan, preserved scan and the corresponding histological slice are compared. Calcification, dense fibrous tissue and necrotic core regions are color-coded in black, blue and yellow, respectively. The grey level intensity shows tissues with different MR contrast that were grouped by the SPFCM algorithm and probably represent tissues with different ratios of smooth muscle cells to collagen. Visually, results corresponds well with histology in extent as well as spatial locations.

To evaluate how characterization of plaque constituents compares between fresh, preserved and histological specimens, we used a component ratio introduced by previous study [43].

$$ComponentRatio = \frac{ComponentArea}{OverallArea}\% \tag{48}$$

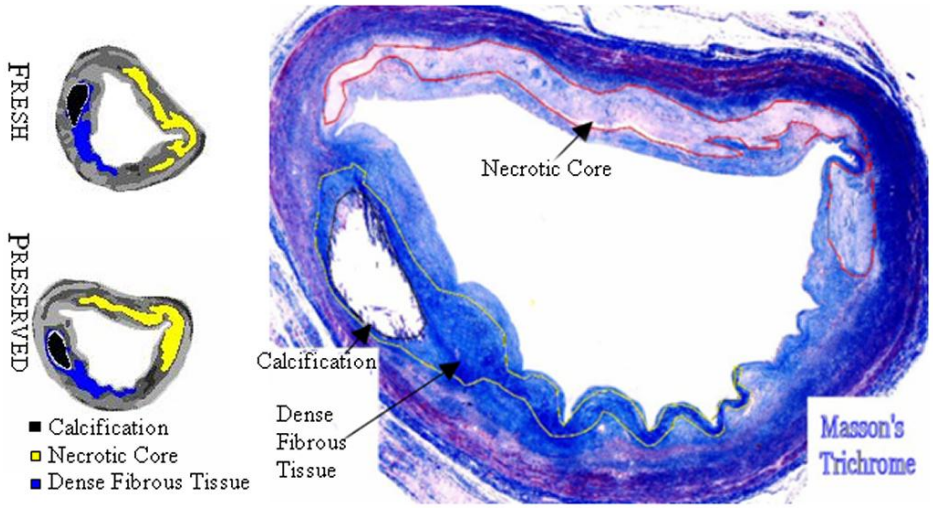

Figure 29: Plaque characterization results (employing intensity-pattern-table labeling) from multicontrast MRI under fresh and preserved conditions compared with manual segmentation of the Mason's Trichrome stain.

This comparison overcomes the registration difficulties caused by morphological deformation during histological processing, but has the drawback of sacrificing positional information of the plaque constituents. Pearson's correlation coefficient and paired-sample student's t-test was used to compare component ratios between fresh and preserved scans, between histology and fresh scans, and between histology and preserved scans.

Since the histological slice ($5\mu m$) is 200 times thinner than that of MRI ($1mm$), we used a component ratio averaged from 1 to 4 histological slices (depending on the variability of plaque geometry and composition across adjacent histological slices) that aligned with the corresponding MR slice to perform the comparison. A single slice was used if the plaque was primarily concentric intimal hyperplasia. Multiple slices were used if the plaque was complex. To compare the component ratios yielded by fresh and preserved characterization and histological results, we evaluated the percent difference in component ratio between two results as:

$$P_{ComponentRatio}(1v.s.2) = \frac{ComponentRatio(1) - ComponentRatio(2)}{ComponentRatio(ref)}\% \qquad (49)$$

For example, if comparing fresh and preserved scans, $fresh = 1$ and $preserved = 2$. The value $P(1vs.2)$ gives the relative difference between component ratios for fresh and preserved scans. $ComponentRatio(ref)$ was set to be the component ratio calculated from

Table 6: Mean and Standard Deviation of Component Ratio Percent Difference for Plaque Constituents

	Fresh*v.s.*Preserved	**Histology*v.s.*Fresh**	**Histology*v.s.*Preserved**
Ca(n=6)	5.01%±27.12%	-6.72%±35.82%	-1.70%±23.72%
FT(n=11)	7.37%±15.86%	-0.47%±12.94%	6.91%±19.57%
NC(n=7)	16.54%±27.17%	-10.71%±31.47%	5.84%±32.34%
Fi(n=2)	-6.29%±8.89%	13.93%±7.40%	7.64%±1.49%
Th(n=1)	-6.49%	-2.60%	-9.09%

Ca-calcification, FT-Fibrous Tissue, NC-Necrotic Core, Fi-Fibrocellular and Th-thrombus. n is the number of ROIs.

Table 7: Paired, Two-tailed t-statistics of Grouped Component Ratio

	Fresh*v.s.*Preserved	**Histology*v.s.*Fresh**	**Histology*v.s.*Preserved**
Component Ratio Difference	-1.13%±3.38%	-0.65%±2.96%	-1.77%±4.60%
r	0.98	0.98	0.97
95% CI for r	0.9579to0.9913	0.9724to0.9944	0.933to0.986
t	-1.731	-1.137	-2.006
p	9.53%	26.58%	5.54%
t critical(d.f.=26)	2.056	2.056	2.056
95% CI for mean	-2.46%to0.20%	-1.82%to0.52%	-3.59%to0.04%

d.f.: dimension of freedom; r: Pearson's correlation; CI: confidence interval.

histology. A paired t-test and a confidence interval analysis were performed to compare differences between fresh and preserved scans.

When component ratios from each of the five plaque constituents (necrotic core, fibrocellular, fibrous tissue, thrombus and calcification) were grouped over all slices, excellent correlation was acquired between fresh and preserved conditions ($r = 0.98$). Similarly, excellent correlation was found between 1) histology and fresh conditions and 2) histology and preserved conditions with Pearson's correlation coefficient of 0.98 and 0.97, respectively. The percent difference (as defined in Eq. 49) in component ratio between the characterization results from fresh and preserved conditions for each plaque component were calculated and are summarized in Table 6. Percent differences in component ratios varied from -6.5% (thrombus) to 16.5% (necrotic core) for fresh vs. preserved scans. Component ratios of all tissue types were grouped together. Then, the two-tailed, paired-sample student t-test was calculated at 95% confident level. They are summarized in Table 7. Based on the t-statistics, there is no significant difference in component ratios between fresh and preserved samples. The 95% confidence intervals were calculated for the paired t-test. From the calculation, it is 95% confident that the paired mean difference between "fresh" and "preserved" characterization results falls in the interval of [-2.46%, 0.20%], which is narrow given the variability of component ratios between tissues.

The result supports our claim in the previous chapter that preservation does not affect the characterization techniques relying on tissues' comparative contrasts.

5.3.1.2 Limitations

From the above characterization results, it can be seen that combining FCM based clustering and "intensity pattern table" labeling provide a promising approach to automatically characterize atherosclerotic plaques. However, there are issues hindering the usage and performance of this approach. The foremost problem is the imaging parameter dependent issues described previously. Usually, the changing of imaging parameters is coupled with the changing of comparative image contrast and thus the intensity pattern table. The hurdle of

generating intensity pattern table for changed imaging parameter greatly reduces the flexibility and robustness of "intensity pattern table" labeling. Moreover, the existence of over and under classification during the classification step makes the interpretation of labeling based on intensity table ambiguous. As a result, significant user interaction is needed for this approach.

5.3.2 Automatic Plaque Labeling Employing Quantitative MR Properties

In previous sections, we have indicated that the solution to the mentioned difficulties associated with plaque characterization lies in the development of a new labeling step to substitute the "intensity pattern table" approach. To achieve this goal, we sought a method based on the fundamental determinant of the MR image contrast - the tissues' MR properties.

Tissues' MR properties can be extracted from MR images and synthesized to generate quantitative maps that have the fundamental information to characterize plaque components. Specifically, previous research [5, 81, 94] has shown that the T2 values of atherosclerotic tissues can be used to differentiate all typical plaque components. This indicates that plaque characterization may benefit from using quantitative T2 maps because tissues' T2 values are independent of the imaging parameters and rely only on temperature and magnetic field strength. In this aspect, quantitative T2 maps may be superior to multicontrast MR images for plaque characterization. However, quantitative maps usually suffer from poor SNR, which often prevents accurate automatic plaque characterization.

We propose a solution to this dilemma by using SPFCM/MAGIC-FCM to classify the *multicontrast MR data* first and then relying on *quantitative T2 maps* to label the classification results. We named this approach as *a Priori* Information Enhanced Clustering (PIEC). The classification step relies on the already described SPFCM and MAGIC-FCM algorithms. In the labeling step, the classified result is labeled by relying on the *a priori* knowledge of each constituent's T2 distribution using a quantitative map. We hypothesize that the PIEC technique will provide accurate plaque characterization results with minimal user interactions.

5.3.2.1 Quantitative T2 Map Calculation

The T2 distributions of coronary plaque components at 4.7T were measured and are listed in the previous chapter (Tab. 2). It should be noted that these values were acquired only from a subset of the coronary images (7 of 15). The T2 distribution for each plaque constituent was estimated with the assumption that it is Gaussian distributed (of the measured mean and standard deviation). The assumption of a Gaussian distribution was justified by visual inspection of the T2 values during measurement and it is also verified by previous research [15]. These T2 distributions servers the purposes of providing "templates" for labeling the plaque constituents.

Each pixel in the quantitative T2 map can then be evaluated against the T2 distribution "templates" to recognize its type (label). It may first seem that additional data are needed besides the multicontrast MRI to calculate quantitative T2 maps, proper acquisition of multicontrast MRI data resolves this inflexibility. Based on Equation (12), the T2 map can be generated easily with a proton density weighted and a T2 weighted image of the same repetition time TR. In other words, quantitative MRI is implicitly included inside the multicontrast MRI dataset. In our acquisition, we conform this restriction and additionally, we restrict the echo time TE to be the same for proton density and T1 weighted images. This scheme ensures the T1, T2 and proton density maps can be easily generated based on the T1, T2 and proton density weighted images.

5.3.2.2 Bayesian Labeling

Given the basic idea of labeling employing quantitative T2 maps, an appropriate scheme is needed to match each pixel's T2 value to the T2 "templates". In the current thesis, the matching was conducted based on Bayesian labeling.

Specifically, SPFCM/MAGIC-FCM was applied to multicontrast MR data first to classify plaque constituents. After the classification, pixels of similar intensity and spatial location are grouped into the same class. Theoretically, given the T2 value of a pixel, its tissue type can be determined based on the *a priori* knowledge about T2 distributions in

the various tissues that comprise the plaque. In practice, it is appropriate to employ a statistical T2 model in plaque labeling given the presence of noise and variable T2 component of each specific tissue.

If we consider the known T2 distributions of plaque components as a conditional probability and estimate the "probability of occurrence" for each plaque constituents, the posterior probability of occurrence given measured T2 values can be easily derived employing a Bayesian approach. Specifically, this process can be formularized as Equation (50), where t describes the T2 value of a specific pixel, c symbolizes the tissue type of a specific pixel, i is used as the tissue type index and p defines the probability function. In this equation, the denominator on the right hand side is a constant, so it is usually ignored.

$$p(c = C_j|t = T) = \frac{p(t = T|c = C_j)p(c = C_j)}{\sum_i p(t = T|c = C_i)p(c = C_i)} \tag{50}$$

In Equation (50), the left hand side is the posterior probability defined as the possibility of a specific tissue belongs to type C_j under the condition that its T2 value equals T. The numerator of the right hand side is the multiplication of the conditional probability (probability of T2 value being T given tissue type is C_j) and the prior probability (probability of tissue' type being C_j). In our application, the conditional probabilities (T2 distributions of each plaque constituents) have already been calculated in the T2 quantification section. The prior probabilities can be assumed to be equal for all the constituents initially, meaning all tissues have equal probability of presence in plaques. After calculating the first slice, the prior probability of the adjacent slice can be updated to be the posterior probability of the previous slice to increase the calculation accuracy. The prior probability for the first slice could be approximated with the calculated posterior probability (for the same slice) as well to improve the labeling accuracy. For most cases, however, equivalent prior probability assumption works well enough for the first slice.

Based on this Bayesian model, the detailed scheme of our proposed plaque labeling is as follows:

1. Calculate a quantitative T2 map using proton density and T2 weighted images.

2. Compute the posterior tissue probabilities of being among all the tissue types, employing Eq. (50) for each pixel

3. determine the overall posterior probability for each segmented class (of the classified results) by summing up the posterior probabilities of all the pixels belonging to this region

4. Label each segmented region using the tissue type with maximum posterior probability

5.3.2.3 Evaluation of PIEC on Computationally Simulated Data

The performance of PIEC characterization was evaluated on the computational phantom based on pixel-by-pixel comparison between the actual tissue type and the characterization results. The computational phantom (Fig. 30(A)) is generated manually based on the histology of a typical advanced plaque. To be consistent with the analyzed MR data, which have an effective in-plane resolution of $30\mu m \times 30\mu m$, the matrix size of the computational phantom was chosen to be 256×256 and the outer diameter of diseased vessel was chosen as $8mm$.

The signal intensity for the multicontrast MR images of this phantom was computed by employing Eq. 12 in the spatial domain. For each pixel of a specific tissue component in the plaque phantom, the T1, T2 and proton density values were assigned randomly based on means and standard deviations of the fresh tissue's T1, T2 and proton density to approximate the MR property distribution. T2 distributions for fibrocellular (fibrous cap), media, necrotic tissue and adipose fat (including excellular lipid) were obtained from a subset of our vessel samples (7 of 15) and described previously. Since the necrotic and fibrous tissues have nearly no signal separation (in multicontrast MR images) and are similar in composition, they are group to be the same tissue - necrotic tissue/core. Besides simulation, T2 distributions also serve the purpose of providing prior knowledge that is needed in plaque characterization. In the computational simulation, T1 and proton density are less critical than the T2 distributions since they are not used in the labeling step of PIEC. The T1 distributions for these tissues were derived from published values [94]. The proton density distributions were assumed to be 1 ± 0.1 for all the tissues except for adipose fat (2 ± 0.1)

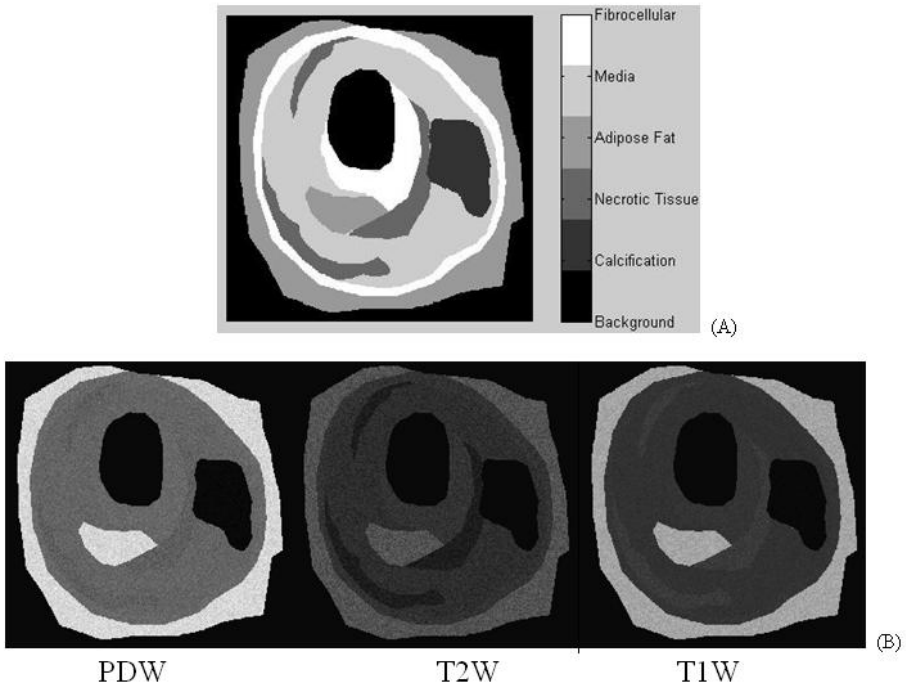

Figure 30: (A) The simulated plaque phantom. The phantom was created manually based on a representative plaque sample from a coronary artery. (B) The simulated proton density, T2 and T1 weighted images based on the phantom.

and calcium (0.1 ± 0.1). The MR properties used in multicontrast MR data simulation are listed in Table 8. In our simulation, two sets of imaging parameters were used. For the first parameter set, TR/TE was chosen to be $900ms/15ms$ for T1 weighted image, $3500ms/15ms$ for proton density weighted image and $3500ms/60ms$ for T2 weighted images. For the second parameter set, TR/TE was chosen to be $1200ms/10ms$ for T1 weighted image, $3000ms/10ms$ for proton density weighted image and $3000ms/50ms$ for T2 weighted image. The phantom and simulated multicontrast MRI data (parameter set 1) are shown in Fig. 30B.

Similar to previous studies [17], we utilized sensitivity, specificity and true positive rate as criteria in evaluating the performance of PIEC. Specifically, sensitivity was calculated as true positives (PIEC was correct in labeling a pixel as a specific tissue type) over the summation of true positives and false negatives (PIEC was wrong in not labeling a pixel as a specific tissue type). Specificity was calculated as true negatives (PIEC was correct

Table 8: Plaque Properties for Multicontrast MRI Simulation

Tissues	**T2**(ms)	**T1**(ms)	**Proton Density**
Media	49.7±9.7	1892±27	1.0±0.1
Necrotic Tissue/Core	30.6±7.0	1114±56	1.0±0.1
Fibrocellular	54.7±10.7	1834±132	1.0±0.1
Adipose Fat	43.2±6.3	636±50	1.0±0.1
Calcification	30.0±7.0	1000±100	0.1±0.1

The MR properties of calcification are roughly estimated.

in not labeling a pixel as a specific tissue type) over the summation of true negatives and false positives (PIEC was wrong in labeling a pixel as a specific tissue type). The true positive rate was calculated as true positives over the summation of true positives and false positives.

The PIEC characterization results of the simulated MR datasets of the two sets of imaging parameters are shown in Fig. 31. Characterization sensitivity, specificity and true positive rate for the two situations are summarized in Table 9. PIEC demonstrates excellent characterization accuracy on both of these two simulated datasets. Since imaging parameters affect the image contrast and thus the fuzzy c-means classification results, there are differences in PIEC's performance on the two datasets. The performance of PIEC on these two simulated datasets demonstrated that PIEC is viable over a range of parameter settings. The comparatively lower accuracy for fibrocellular and media tissues is caused by the low contrast between them since their compositions are similar.

Comparing the characterization results in Fig. 31 with the computational phantom in Fig. 30, we can see that all the tissue types are correctly labeled. The Bayesian quantitative T2 labeling function of PIEC characterization works well even in case of marginal separation (fibrocellular, media and adipose fat). Moreover, from the comparison, it can be seen that segmentation errors in the classification step are the main contributor to mischaracterization.

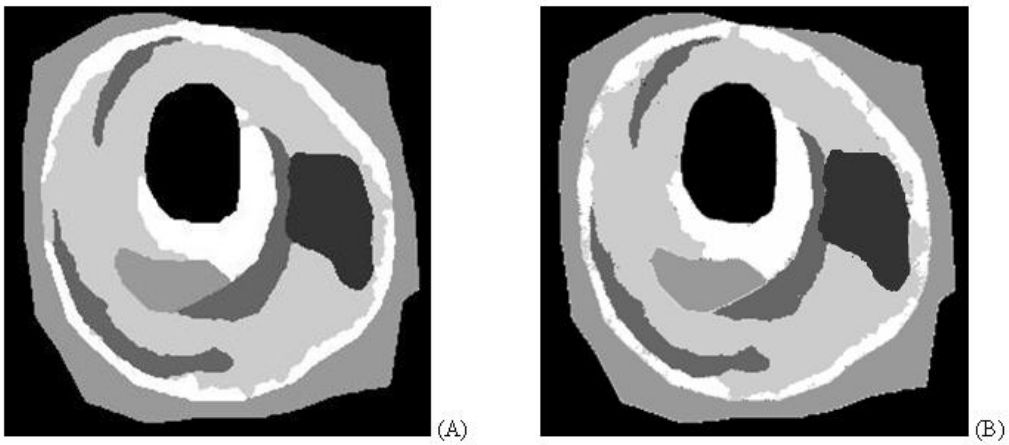

Figure 31: (A) PIEC characterization result of the simulated multicontrast MR dataset 1; (B) PIEC characterization result of the simulated multicontrast MR dataset 2.

Table 9: Sensitivity, Specificity and True Positive Rate of PIEC Characterization

Tissues	**Sensitivity(1‖2)**	**Specificity(1‖2)**	**True Positive Rate(1‖2)**
Media	96.9%‖94.8%	98.4%‖97.4%	94.9%‖92.2%
Necrotic Tissue	98.7%‖97.9%	99.7%‖99.3%	95.8%‖90.5%
Fibrocellular	90.2%‖81.2%	99.4%‖99.2%	95.9%‖93.5%
Adipose Fat	99.8%‖99.7%	99.6%‖99.9%	98.4%‖99.8%
Calcification	99.8%‖99.5%	99.9%‖99.9%	99.7%‖99.8%

Totally 65536 pixels were analyzed for each characterized image.

5.3.2.4 Evaluation of PIEC on Multicontrast MRI Acquired Under Fresh Conditions

PIEC characterization was then applied to multicontrast MRI data acquired on the coronary artery samples (all 15 vessels acquired under fresh conditions). The characterization results were evaluated based on histological results being the gold standard. Both classification and labeling contribute to the mischaracterization in the final result. Since the classification accuracy of the FCM based algorithm on *ex-vivo* scans has already been evaluated in previous studies [43, 91], we only assessed the performance of the labeling step of PIEC characterization for the coronary scans. To evaluate the performance of PIEC labeling, the histological results were manually segmented and labeled by our histology colleagues, resulting in a number of separate tissue segments. Histological segments were aligned with PIEC characterization results based on the morphological landmarks. For each tissue segment of the PIEC characterized results, its tissue type label was checked against that of the characterized histological images to inspect whether the PIEC response is correct. The true positive rate of the labeling step, as defined above, was used as the evaluating criterion. Here, the false positive of a specific tissue was the summation of all isolated segments that belong to this tissue according to PIEC but not labeled as it by histology. The true positive for a specific tissue is the number of segments where PIEC labeled tissue correctly according to histology.

A typical PIEC result on a slice containing calcium, fibrocellular, media, necrotic tissue as well as adipose fat result is shown in Figure 32. Visually, the PIEC result identifies various plaque tissues consistent with histological stains. The chemical shift artifact causes minor mischaracterization near the outside boundary (arrow). The tissue culture media M199 has a much greater T2 value ($> 500ms$) than plaque tissues. It is classified and labeled as background. In Figure 33, another example is shown. In this example, the five angle star marked a region of adipose fat that is mislabeled as media.

Out of the fifteen vessel samples, two vessels contain two distinct atherosclerotic plaques; the others contain only one plaque. For each of the seventeen plaques, a single MRI slice that was well aligned with histology was selected and used to measure the true positive rate of the Bayesian labeling to assess the labeling accuracy. The measured true positive

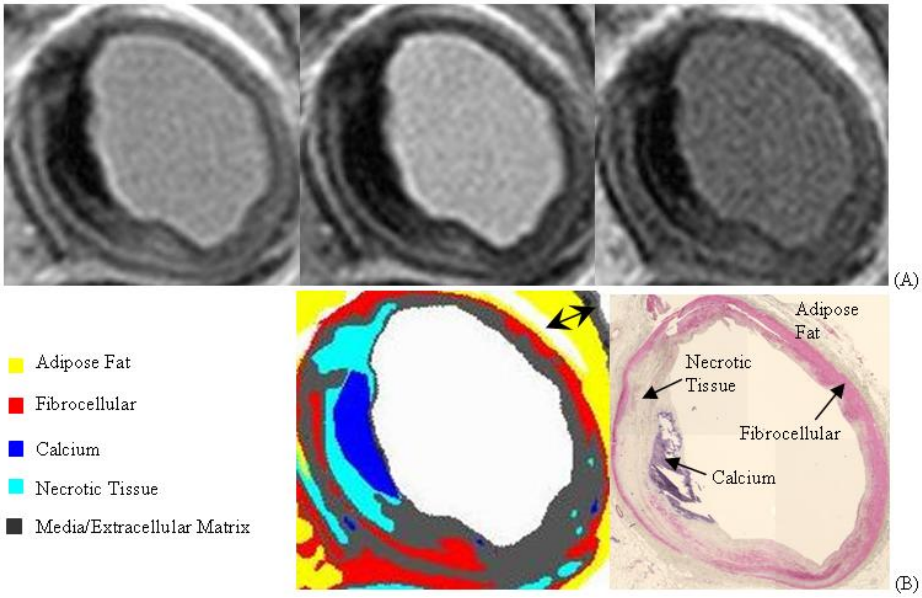

Figure 32: (A) Multicontrast MRI of coronary plaque tissue (from left to right: proton density, T2 and T1 weighted), and (B) Color coded PIEC characterized result (left) and corresponding smooth muscle actin stain (right).

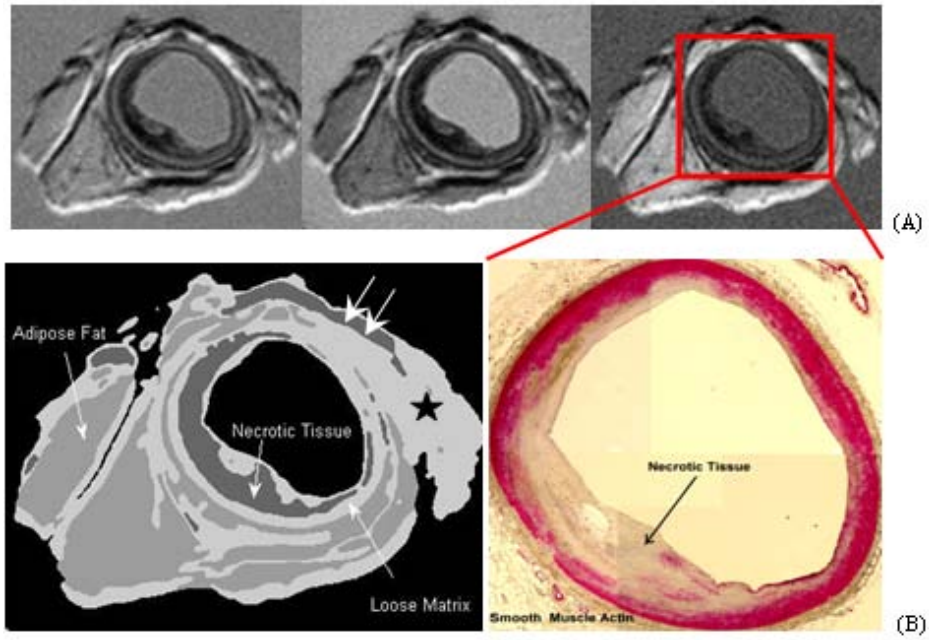

Figure 33: (A) Multicontrast MRI of coronary plaque tissue (from left to right: proton density weighted, T2 weighted and T1 weighted), and (B) PIEC characterized result (left) and smooth muscle actin stain (right) corresponding to the region contained in the rectangular box.

rates ranged from 69% to 100%. Specifically, the true positive rates are 88.9%, 70.6%, 69.2%, 94.7%, 75.0%, 100.0% for calcification, adipose fat, media(loose matrix), necrotic tissue, fibrocellular, M199, respectively. Since the fibrocellular, media and adipose fat's T2 distributions are not well separated, it was not surprising that their true positive rates are lower than those of calcium and necrotic tissue.

5.3.2.5 Discussion

Most previous investigations on automated plaque characterization have relied on using multicontrast MR data alone. Itskovich et al. [43], Adame et al. [2] and Sun et al. [91] employed various FCM based algorithms in combination with the intensity patterns on multicontrast MR images to characterize plaque constituents. The main advantage of these unsupervised techniques is that no training is required. However, they are usually susceptible to over or under classification issues and require user interactions to resolve the logic ambiguity when interpreting the intensity table. Alternatively, Clarke et al. [16, 17] developed a maximum likelihood classifier that relies on the actual intensities of plaque tissues on multicontrast MR data, and Liu et al. [61] used a Bayesian approach that relies on tissue intensity on multicontrast MR images and morphological knowledge. Both these two supervised techniques avoid the under and over classification problem mentioned above but need repetitive training, which makes them more dependent on imaging parameters and scanner systems.

The PIEC technique described in the thesis incorporates the advantages of both supervised and unsupervised techniques by separating characterization into classification and labeling. The unsupervised classification part operates on high SNR multicontrast MRI data to segment different tissue groups, while the supervised labeling part operates on the lower SNR quantitative T2 maps to label the classified tissue groups.

The main benefit of using quantitative MR properties for tissue labeling is that the quantitative property distributions only need to be measured once for a specific magnetic field strength. It should also be noted that no additional data acquisition is needed for quantitative MRI labeling since a rough T2 map, calculated based on the proton density

and T2 weighted MR images (with the same TR) of the multicontrast MR dataset, are used to determined posterior probability. In the current thesis, we focus on employing the quantitative T2 distributions of plaque tissues to label classification result based on a Bayesian approach because it has been shown in many studies that each plaque component has a characteristic T2 distribution. Based on our experiments, plaque labeling based on T2 distributions is sufficient in most cases. However, instances of false PIEC labeling occurred in some cases where the T2 distributions are only marginally separated (Tab. 8). To reduce the false labeling rate under this situation, the Bayesian labeling could be generalized to utilize MR properties other than T2. For example, it can be seen that although media/loose matrix and adipose fat have similar T2 values, their proton densities are quite different. To take advantage of this, the conditional probability density can be generalized from a 1-dimensional Gaussian distribution to a multiple joint Gaussian distribution (Eq. (51)) in the Bayesian formulation (Eq. (50)).

$$p(t1 = T1, t2 = T2, pd = PD...|c = C_j) = \frac{e^{-\frac{1}{2}[x-\mu_x]^T C^{-1}[x-\mu_x]}}{(2\pi det(C))^{\frac{n}{2}}} \tag{51}$$

In Equation 4, x symbolizes the vector form of tissues' MR properties (T1, T2, PD); μ_x and C are the expectation and covariance matrix, respectively. By assuming all the MR properties are independent from each other, the covariance matrix can be approximated as diagonal matrix with its eigen values equal to the standard deviations of the tissues' MR properties. The multiple joint Gaussian distribution potentially improves the performance of PIEC by providing more separation of different tissue groups and minimizing the false labeling. An example using this generalized PIEC technique is shown in Figure 34. From this figure, the advantage of adding other MR properties in labeling provide much better separation for plaque components.

Another MR property that may add value to plaque tissue labeling is the ADC value. This property may help to better label the thrombus tissue, which has a variable T2 but constant ADC, according to previous studies [5, 95]. Besides MR properties, other a priori knowledge can be included in the multiple joint Gaussian probability of the Bayesian labeling formulation. One example is the morphological information proposed by Liu et al

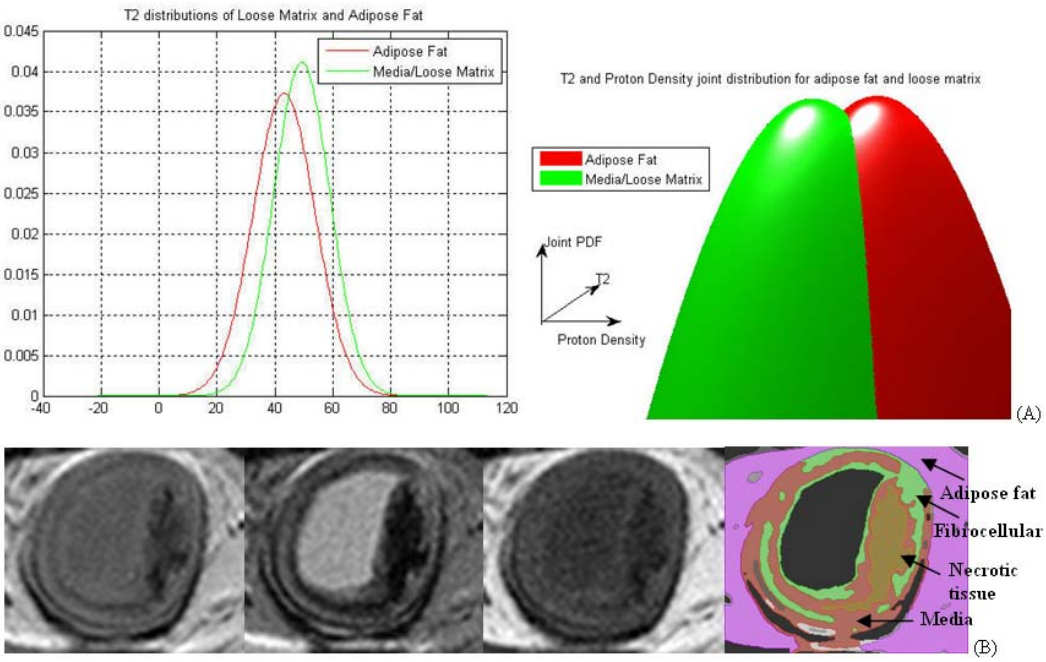

Figure 34: (A) T2 distributions (left) and T2-PD joint distributions (right) of adipose fat and media. (B) Multicontrast MRI of coronary plaque tissue (from left to right: proton density weighted, T2 weighted and T1 weighted) and PIEC characterization result employing T2-PD joint distributions.

[61]. Similarly as with the MR properties, this a priori information is system and imaging parameter independent and requires no repeated training.

Accurate measurements of plaque tissues' MR biophysical properties are necessary in order to utilize them for tissue labeling. The *in-vivo* measurements of plaque tissues' T2 distributions under operating magnetic field strengths are essential for PIEC to be used clinically. A database containing T2 distributions under different conditions may facilitate this practice.

As pointed out earlier in this chapter, a common issue with FCM based techniques is under or over classification of plaques because the number of tissues present in the plaques is unknown. In PIEC, this problem is handled by always over classifying the plaque constituents in the clustering step; and the over classified groups of the same tissue are identified as the same type in the labeling step. The other potential advantage from over classification is that the initial centroid dependent issue of the clustering technique could be alleviated.

Just as additional MR properties can improve the accuracy and reliability of plaque

labeling, additional contrast mechanisms provide more separation between tissues on MR images and thus generate better classification results. For example, Hatsukami et al. [41] reported that three dimensional MOTSA sequence can be used to better distinguish thick fibrous tissues from the thin rupture-prone caps. Given the trade-off between more contrast mechanisms and acquisition time, one of the future needs in MR plaque characterization is to determine the optimal number and type of MR acquisitions.

One of the limitations of the current research is that both the simulated and *ex-vivo* MR data were not deteriorated by motion. Moreover, the resolution/SNR of these scans is not achievable for *in-vivo* scans. Therefore, PIEC's performance is expected to degrade when applying to *in-vivo* data. Additionally, our coronary sample size is limited. Most vessels we harvested from heart transplant patients were highly fibrotic and none contained intra-plaque/mural thrombi. Nevertheless, inclusion of new tissue types should be readily supported by PIEC characterization theoretically. As mentioned earlier, thrombus has non-uniform T1 and T2 values and may cause problems during classification and labeling. Potentially, it could be mitigated by including the ADC in the joint Gaussian probability density function.

5.4 Conclusion

Throughout the chapter, efforts were made to develop an automatic plaque characterization routine that is viable over a range of imaging conditions and system imperfections. The characterization, often regarded as a single step processing, was further divided into classification and labeling. This separation provides a lot of flexibility for plaque characterization.

The classification relies on FCM based clustering technique to segment different tissue groups. Taking into consideration of noise and inhomogeneity, SPFCM and MAGIC-FCM techniques were developed to improve the classification accuracy in the presence of system imperfection. A new labeling approach utilizing quantitative MR properties was proposed. Combining this labeling technique with SPFCM/MAGIC-FCM, an automatic plaque characterization called PIEC was developed. The main contribution of PIEC comes from this labeling process, which makes it unique and superior to existing plaque characterization

techniques. The Bayesian labeling renders plaque characterization independent of imaging parameters. Moreover, this labeling step overcomes the over and under classification issues of the FCM clustering, which require significant amount of user interactions. It should be emphasized that all these benefits attributes to the inclusion of quantitative MR maps in plaque characterization. To the best of our knowledge, PIEC is the first technique that utilizes quantitative MR maps in characterizing plaque components. Since the quantitative maps could be reconstructed from multicontrast MR data easily with proper selection of imaging parameters, PIEC requires no additional image acquisition. The evaluations on simulated and *ex-vivo* multicontrast MRI data demonstrate that PIEC is robust and accurate thus is a very promising candidate for automated plaque characterization.

CHAPTER VI

ACCELERATING THE ACQUISITION OF MULTICONTRAST MRI

6.1 Introduction

Lengthy acquisition time is one of the major barriers in the clinical utility of multicontrast MRI in atherosclerotic plaque imaging. Economically, long acquisition time increases the diagnosis expenses. Technically, long acquisition time inevitably introduces patient motion, which degrades the image quality and increases the difficulties in registering the multicontrast MR images.

Generally, the majority of fast MR imaging techniques involve one or combinations of the following approaches: fast k-space coverage scheme, short repetition time, segmenting the longitudinal magnetization. These techniques achieve the reduced imaging time at the expenses of image resolution and SNR. Such schemes have many applications. However, since resolution and SNR are critical in plaque characterization, these techniques are often not viable for multicontrast MRI acquisitions.

To increase the temporal resolution of dynamic imaging (i.e. MRI acquisitions are required for the same location after administration of the contrast agent) a unique k-space sharing scheme can be applied to accelerate the MRI acquisitions. This type of approach relies on the fact that all the images from the same location contain similar information (edge and other detailed information). From MR physics, it is known that this edge information resides in the outer edges of k-space. With this information, "shared k-space" techniques were proposed based on the idea of acquiring the outer k-space for all the dynamic images only once. These techniques accelerate the MRI acquisition without sacrificing the image resolution and SNR. Generally, they reduce the acquisition time for a single MR image 2-8 fold.

Although the k-space sharing schemes are used mainly for dynamic imaging, they have the potential of helping multicontrast MR image acquisition in the same fashion. In this

chapter, the feasibility of using "shared k-space" techniques in fast multicontrast image acquisitions are investigated. Specifically, we hypothesize that "shared k-space" reconstructed multicontrast MRI data can provide similar plaque characterization results as "full k-space" reconstructed data.

6.2 MR Image Formation

Before introducing "shared k-space" reconstruction, the general image formation of MRI need to be introduced. For better understanding, it is helpful to review the essential MRI physics covered in Chapter III. In Equation (7), it is shown that the acquired MR signal represents the frequency information (k_x, k_y, k_z) of the spatial data (x, y, z). Reconstruction of the MR images, based on this relationship, is just a simple inverse Fourier transformation of the acquired MRI signal.

Besides inverse Fourier transformation, there are other MR image reconstruction techniques for specific applications. For instance, filtered back-projection scheme similar to CT image reconstruction is usually employed for radial sampled k-space acquisition. An example is the Periodically Rotated Overlapping ParallEL Lines with Enhanced Reconstruction (PROPELLER) technique [74], which is a promising technique in motion suppression.

Because of the Fourier relationship between k-space and spatial data, all the Fourier transform properties can be applied to MR image reconstruction. These properties include: linearity, convolution, conjugation, scaling, time reversal, time shift, modulation, Parseval's theorem, etc. If the MR image is real, the Hermitian symmetry property (Eq. (52)) of the k-space can be utilized to reduce the acquisition. This technique, also known as half Fourier MRI reconstruction, is an example showing how reduced k-space coverage can be used to speed up the MR data acquisitions. Assuming there are 128 phase encoding steps in a full k-space acquisition, the half Fourier reconstruction requires acquisition of only 64 phase encoding steps. For most spin echo and gradient echo based sequences, this reduces the data acquisition by half. In practice, because of the system imperfections, the Hermitian relationship is only approximated. Therefore, usually more than 50% of the full k-space is collected for better SNR.

$$k(m,n) = k^*(m,-n) \tag{52}$$

It is worthwhile to mention that parallel imaging, an alternative approach for fast MR data acquisition, involves reconstruction techniques from multiple channels of data acquired from receivers in different spatial locations. For details on reconstruction techniques such as Sensitivity Encoding (SENSE) [76], Simultaneous Acquisition of Spatial Harmonics (SMASH) [86] and GeneRalized Autocalibrating Partially Parallel Acquisitions (GRAPPA) [38], the reader is referred to more specific literature.

6.3 "Shared K-space" Reconstruction

After the brief introduction about MR image reconstruction, "shared k-space" techniques can now be better understood. Keyhole [46, 97] and reduced-encoding imaging by general-series reconstruction (RIGR) [54] are "shared k-space" techniques developed for dynamic imaging.

As mentioned above, the key idea of these techniques is to reconstruct dynamic MR images relying only on the center k-space of the current frame. The outer k-space will be retrieved from reference images acquired previously. The underlying reason for doing this is because there is data redundancy in dynamic images. When comparing a series of dynamic frames, the edge and morphological information is comparable in all the images despite the change of image contrast. The fact that this redundant information resides in outer k-space enables us to substitute the outer k-space of dynamic images with that of the reference image, which requires less k-space coverage. In the keyhole technique, direct replacement of the outer k-space is applied to achieve this goal. This approach, however, does not ensure the continuity of the k-space data. As a result, direct substitution usually introduces Gibbs ringing. This problem can be overcome in the RIGR technique by constrained reconstruction.

The theories of keyhole and RIGR reconstructions are briefly covered in the following two sections. Generally speaking, both techniques acquire the full k-space of a reference image and only the center k-space of the objective images. The objective images are then

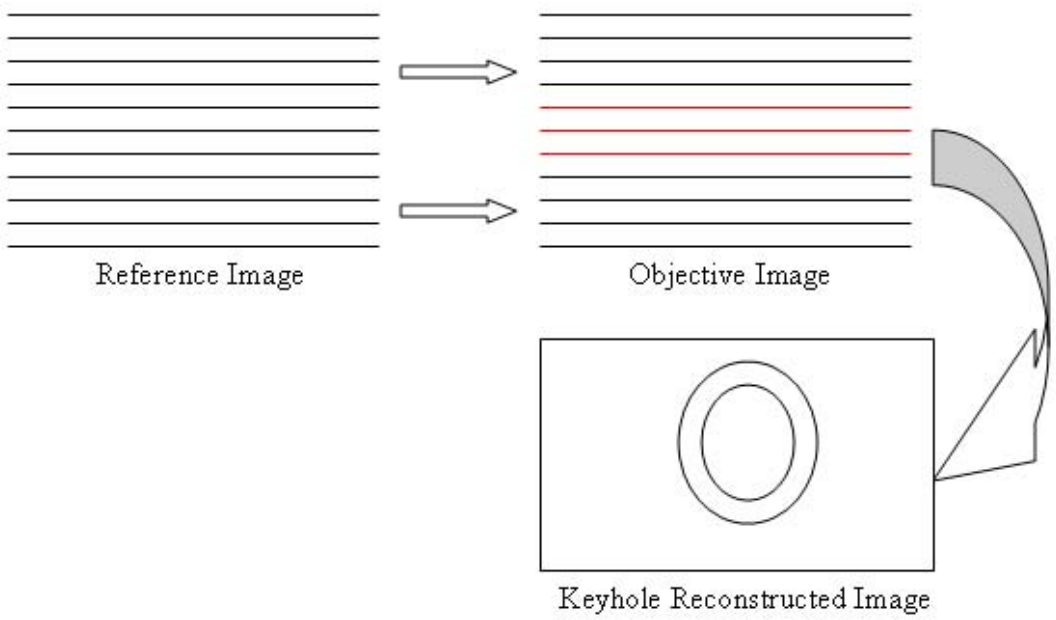

Figure 35: The schematic drawing showing keyhole reconstruction. In the objective image, the red k-space lines symbolize acquired center k-space, black lines symbolize k-space data borrowed from the reference image.

reconstructed using both the acquired center k-space and high frequency information from the reference image. Because the same amount of k-space as reference image is used for objective image reconstruction implicitly, "shared k-space" reconstruction does not sacrifice resolution and SNR, theoretically.

6.3.1 Keyhole Reconstruction

Keyhole reconstruction was independently proposed by Van et al. [97] and Jones et al. [46]. In this technique, the outer k-space of the reference image is combined with the acquired center of k-space from the objective image to reconstruct the full objective image. Figure 35 schematically illustrates the direct k-space replacement approach of keyhole reconstruction.

Because the k-space used in keyhole reconstruction is synthetic, the magnitude and phase are not continuous. This k-space inconsistency introduces Gibbs ringing artifacts, which manifests as false edges on the reconstructed MR images. The ringing artifact can get very serious when the borrowed k-space portion is large or when the contrast between reference image and objective images is great. This artifact could potentially mimic the

plaque tissues and may degrade the plaque characterization.

6.3.2 RIGR Reconstruction

The k-space inconsistency issue in the keyhole reconstruction is overcome by the constrained reconstruction of RIGR, which was developed by Liang and Lauterbur [54].

The mathematical framework for RIGR is based on generalized series (GS) model. With the GS model, the reconstructed image I_{GS} is expressed as the weighted summation of basis functions (Eq. (53)).

$$I_{GS} = \sum_n c_n \varphi_n \tag{53}$$

In Equation (53), c_n is the weighting factor and φ_n is the basis function. In case the basis function is sinusoidal functions, the equation becomes a Fourier series expression. In RIGR, the basis function are chosen to be the family of constrained complex sinusoids (Eq. (54)).

$$\varphi_n = T e^{i2\pi n \Delta k x} \tag{54}$$

, where T is a constraint function containing the *a priori* information. The GS reconstruction function, accordingly, can be reformulated as Equation (55).

$$I_{GS} = T \sum_n c_n e^{i2\pi n \Delta k x} \tag{55}$$

The constraint function in Equation (55) can be derived from the magnitude of reference image, $|I_{ref}|$. With this substitution, the GS function becomes:

$$I_{GS} = |I_{ref}| \sum_n c_n e^{i2\pi n \Delta k x} \tag{56}$$

Under this framework, the problem of reconstruction is converted to the calculation of the weighting factors. In RIGR, the weighting factors can be computed with the constraint that the k-space of reconstructed image should equal to the corresponding acquired k-space of the objective image. Assuming there are totally $2N + 1$ phase encoding lines (from $-N$ to N) acquired for the objective image, Equation (56) becomes the following:

$$I_{GS} = |I_{ref}| \sum_{n=-N}^{N} c_n e^{i2\pi n \Delta k x} \tag{57}$$

$$k_{acq}(m) = \int_{-\infty}^{\infty} I_{GS} e^{-i2\pi m \Delta kx} dx \tag{58}$$

The constraint discussed above is formulated in Equation (58), where $k_{acq}(m)$ is the acquired center k-space of the objective image. Substituting I_{GS} with Equation (57), the constraining functions is reformulated as (59).

$$k_{acq}(m) = \int_{-\infty}^{\infty} |I_{ref}| \sum_{n=-N}^{N} c_n e^{i2\pi n \Delta kx} e^{-i2\pi m \Delta kx} dx \tag{59}$$

Substantiating the Fourier transform of $|I_{ref}|$ with k_c, (59) is converted to a set of linear equations illustrated in (60).

$$k_{acq}(m) = \sum_{n=-N}^{N} c_n k_c(m-n), \qquad -N \leq m \leq N \tag{60}$$

These linear equations can be solved more efficiently in the matrix form shown in (61):

$$Hc = k \tag{61}$$

, where H is the matrix shown in 63, c is the weighting vector $[c_{-N}, c_{-N+1}, c_{-N+2}, ..., c_{N-2}, c_{N-1}, c_N]^T$, and k is the acquired k-space data $[k_{acq}(-N), k_{acq}(-N+1), k_{acq}(-N+2), ..., k_{acq}(N-2), k_{acq}(N-1), k_{acq}(N)]^T$.

$$H = \begin{bmatrix} k_c(0) & k_c(-1) & k_c(-2) & ... & k_c(-2N) \\ k_c(1) & k_c(0) & k_c(-1) & ... & k_c(-2N+1) \\ k_c(2) & k_c(1) & k_c(0) & ... & k_c(-2N+2) \\ . & . & . & ... & . \\ . & . & . & ... & . \\ . & . & . & ... & . \\ k_c(2N) & k_c(2N-1) & k_c(2N-2) & ... & k_c(0) \end{bmatrix} \tag{62}$$

Many numerical schemes such as Levinson algorithm can be used to solve Equation (61). Since the matrix H may be rank-deficient in practice, it is suggested [54] that perturbation be introduced by replacing H with $H + \mu I$ to solve the problem. Here, μ is determined based on the SNR [53] and I is the identity matrix.

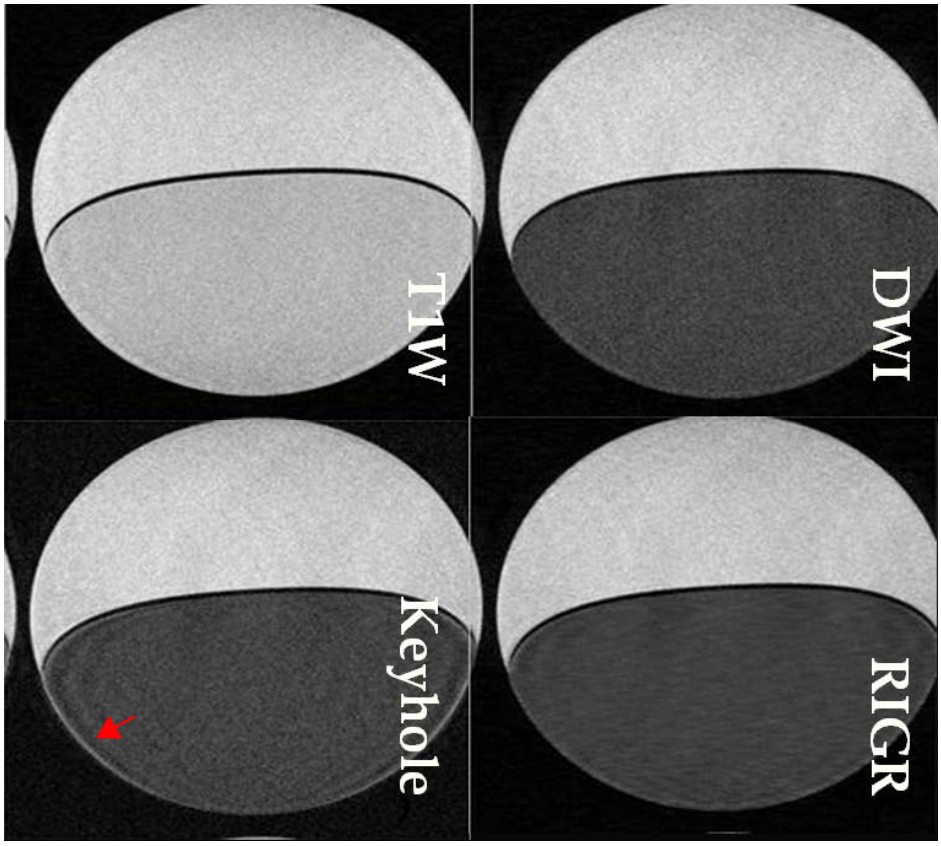

Figure 36: "Shared k-space" reconstruction on water-fat phantom. The upper row shows the full k-space reconstruction of T1 (left) and diffusion (right) weighted images. If using T1 weighted image as reference image, and with 1/8 original k-space of the diffusion weighted image, the "shared k-space" results can be reconstructed with keyhole (lower left) and RIGR (lower right) scheme. It can be seen that both keyhole and RIGR reconstruction results approximate the full k-space results very well. In the keyhole result, Gibbs ringing artifact (marked by arrow) is seen near the boundary location.

The constraint function, T, can contain phase *a priori* information besides magnitude. Under this situation, T is replaced by $|I_{ref}|e^{i\theta}$. It is suggested [54], however, that including phase constraints, in most cases, gives inferior result than using magnitude alone in RIGR reconstruction.

The advantage of RIGR over keyhole technique is the k-space data consistency. It can be easily verified that the extrapolated k-space data (outer k-space) are continuous at least to the $2N^{th}$ order at the merging boundaries [54]. Because of this, the Gibbs ringing artifacts are maximally suppressed.

6.4 "Shared K-space" Reconstruction in Multicontrast MRI

6.4.1 Preliminary Study

For multicontrast MRI, "shared k-space" techniques share the outer k-space for MR images of different contrast mechanisms rather than dynamic images. The keyhole and RIGR techniques developed for dynamic imaging are readily applicable to multicontrast MR data. This idea is first tested on a water-fat phantom acquired with regular spin echo sequence (4.7T small bore scanner, birdcage coil). The result is shown in Figure 36. It can be seen that both keyhole and RIGR reconstruction results approximate the "full k-space" reconstructed diffusion weighted image very well. In the keyhole result, Gibbs ringing artifact, as expect, is seen near the boundary location (arrow on Figure 36).

The "shared k-space" techniques were then tested on the atherosclerotic vessel images retrieved from 1.5T Siemens clinical scanner. The MR images were acquired with a 4-element phased-arrayed coil using turbo spin echo sequence (TSE, turbo factor = 25). From the results, we found that although 1/8 k-space reconstruction provides reasonable results, it missed some fine details in some cases. This indicates the necessity of increasing k-space coverage. We, therefore, tested on using 1/4 k-space to perform the reconstruction, which gave more accurate approximations.

"Shared k-space" reconstruction techniques, based on the preliminary results, show promises in accelerating multicontrast MRI acquisition. The following study is conducted for more systematic evaluation of the techniques.

6.4.2 Experiment Setup

Five atherosclerotic aortas from cadavers were obtained from the morgue at Emory University Hospital. The study was approved by the institutional review board of Emory University. The vessels were cut open and immersed in formalin prior to the MR scanning.

All MRI scans were conducted on a Siemens MAGNETOM Avanto 1.5T scanner (*Siemens Medical Solutions, Erlangen, Germany*) using a 2-channel carotid coil (*CAD Sciences, White Plains, NY*) at room temperature ($\sim 20^{\circ}C$). After identifying the plaque(s) on

Table 10: Imaging Protocol and Parameters for "Shared K-space" Reconstruction Experiment

	PD Weighted	**T1 Weighted**	**T2 Weighted**	**Partial T2 Weighted**
TR(ms)	2000	500	2000	2000
TE(ms)	9.8	12	81	58

TSE factor = 11 for all sequences.

the survey image(s), two-dimensional multi-slice TSE sequences were used for all the multicontrast MRI acquisitions. The MRI protocol and parameters are summarized in Table 10. For all acquisitions, the FOV was $8cm \times 8cm$ and the slice thickness was $2mm$. The acquisition matrix was 512×264, which yields the in-plane resolution of $0.16mm(Readout) \times 0.3mm(Phase)$. Five slices were acquired per vessel. For each slice, the number of excitations (NEX) was three.

6.4.3 "Shared K-space" Reconstructed Data Analysis

To perform the "shared k-space" reconstruction for multicontrast MRI, proton density weighted images were set as reference images. Images of other contrast mechanisms were reconstructed with: 1) fully acquired k-space using regular inverse Fourier transform, and 2) 25% k-space (65 out of 264 lines) employing "shared k-space" approaches.

Quantitative T2 values calculated employing "full k-space" and "shared k-space" reconstructed multicontrast MR images were quantitatively compared. In order to evaluate the effect of "shared k-space" reconstructions on plaque characterization, the PIEC methodology described in the previous chapter was applied to both "full k-space" and "shared k-space" reconstruction results. Specifically, PIEC results from "shared k-space" reconstructed multicontrast MRI were compared against PIEC results from "full k-space" reconstructed images, which serve as the gold standard. Pixel-wise characterization accuracy (K), defined in Equation (63), was used as the evaluation criterion.

$$K = \frac{number\ of\ pixels\ correctly\ characterized\ according\ to\ gold\ standard}{total\ number\ of\ pixels}\% \qquad (63)$$

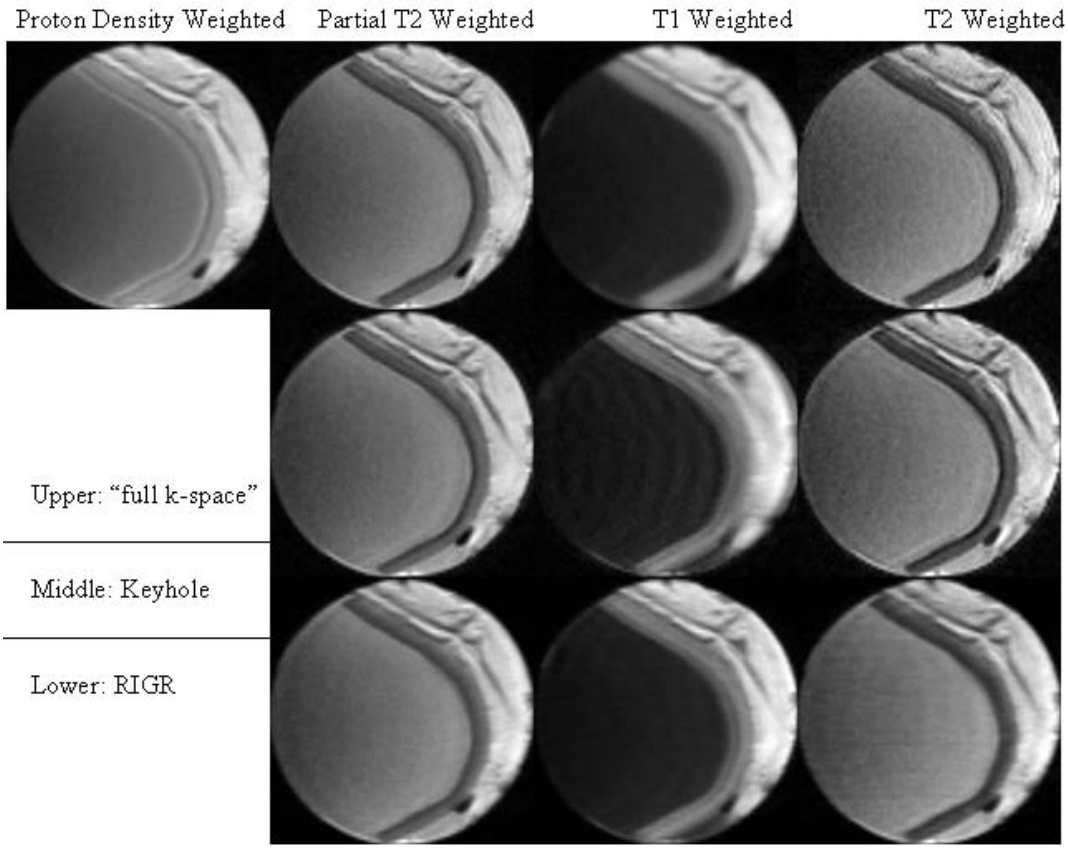

Figure 37: Visual comparison between "full k-space" and "shared k-space" reconstructions. The upper, middle and lower rows show the "full k-space", keyhole and RIGR reconstructed results, respectively. The "shared k-space" reconstruction results appear to approximate the "full k-space" reconstruction results quite accurately. As expected, RIGR reconstruction exhibits better suppression of the Gibbs ringing artifact than keyhole (see T1 weighted image). However, for all the vessel samples, the RIGR reconstruction results appear blurry and possess reduced contrast compared to keyhole results (see T2 weighted images).

6.4.4 Results and Discussion

6.4.4.1 Qualitative Comparison

In general, the "shared k-space" reconstructed results approximate the "full k-space" reconstructed results very well.

A typical example is shown in Figure 37. As expected, RIGR reconstruction exhibits better suppression of the Gibbs ringing artifact than keyhole reconstruction. However, for all the vessel samples, the RIGR reconstruction results visually appear blurry and possess reduced contrast compared to the keyhole reconstruction results. For this specific example,

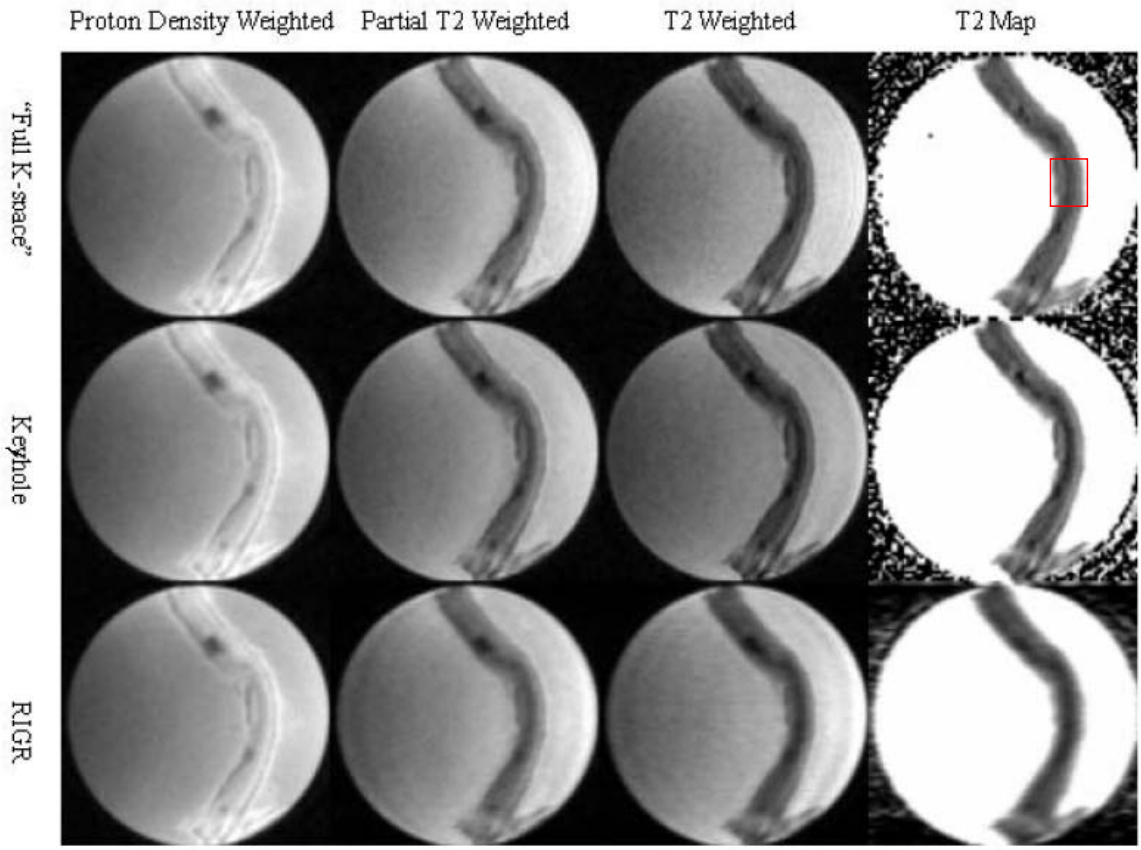

Figure 38: T2 maps of "full k-space" and "shared k-space" reconstructed MRI. The upper, middle and lower rows show the "full k-space", keyhole and RIGR reconstructed MRI data and its corresponding T2 map, respectively. It is apparent that T2 map from keyhole reconstructed MR images approximates the "full k-space" T2 map much better than that from RIGR data. Note: the three proton density weighted images shown here are identical.

the sharpness of the transition between fibrous tissue and media, defined as the slope of the transition in 1D profile, are 6.9 and 2.5, and the contrast to noise ratio (CNS), defined as the difference between SNR(media) and SNR(fibrous), are 7.2 and 2.3, respectively. The smoothing and reduced contrast of RIGR reconstructed images are the byproducts of Gibbs ringing suppression.

6.4.4.2 Quantitative T2 Map Comparison

For each vessel sample, quantitative T2 maps were calculated employing "full k-space", keyhole and RIGR reconstructed MRI data (specifically, proton density, partial T2 and T2 weighted images) separately. Details about T2 map calculation were presented in Chapters III. Figure 38 illustrates a typical example of T2 maps calculated from the MRI dataset

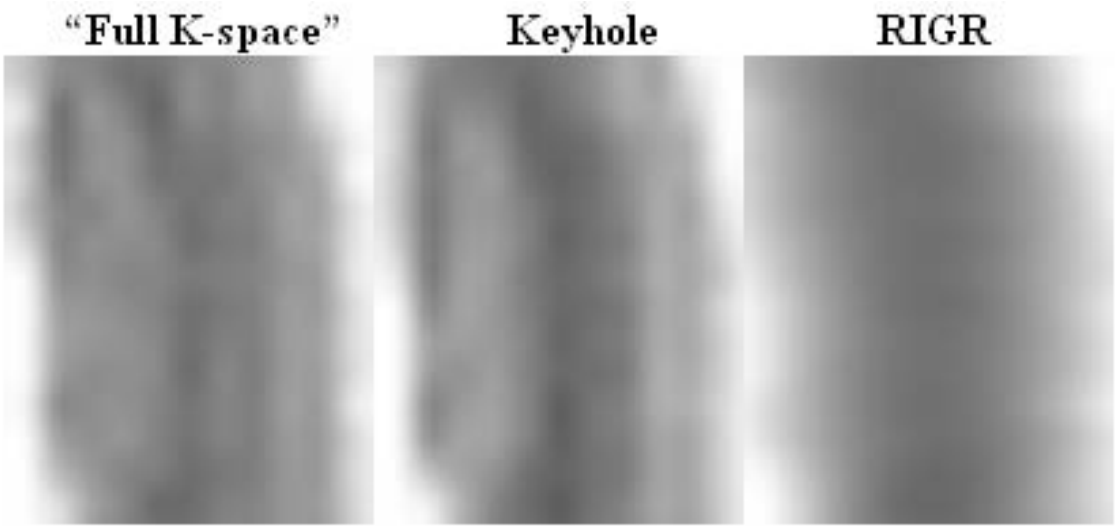

Figure 39: Enlarged view of the region marked by the red rectangular shown in Figure 38.

reconstructed using the three schemes. The computational T2 maps calculated based on keyhole data appear to approximate the "full k-space" T2 maps more accurately than those from RIGR data. A enlarged view of the region marked by the red rectangular in Figure 38 is shown in Figure 39.

In the vessel tested, atherosclerotic plaques are predominately composed by media, fibrous tissue and adipose fat. Their T2 values were measured on T2 maps from "full k-space", keyhole and RIGR reconstructed MR data. To avoid observer bias, the same pixel locations were chosen in measuring the T2 values for a specific tissue type across all three T2 maps. T2 values for media, fibrous tissue and adipose fat measured on "full k-space", keyhole and RIGR T2 maps were summarized in Table 11.

The T2 values additionally exhibit the problem of RIGR reconstruction in multicontrast MRI. Pair two-tailed student t-test with 95% confidence level was performed to statistically compare the T2 values. For "full k-space" and keyhole comparison, the p values are 0.90, 0.34 and 0.16 for adipose fat, media and fibrous tissue, respectively. For "full k-space" and RIGR comparison, all the p values are smaller than 10^{-18}. It demonstrates that the T2 values calculated using "full k-space" reconstructed MR data are similar to those on keyhole reconstructed data, but statistically very different from those calculated on RIGR data.

Table 11: T2 Values Calculated Using "Full K-space", Keyhole and RIGR Reconstructed MR Data

	Adipose Fat (ms)	**Media** (ms)	**Fibrous Tissue** (ms)
"Full K-space"	89.6±7.3	52.8±5.5	44.7±6.1
Keyhole	89.7±7.1	53.1±6.3	43.9±6.6
RIGR	84.9±7.6	49.4±5.7	45.5±7.6

Moreover, as shown in Table 11, the T2 values calculated using RIGR data are poorly separated (media and fibrous cap) due to the smoothing effect of RIGR reconstruction. This observation, along with the visual inspections described previously, indicates potential inferior PIEC characterization on RIGR data to keyhole data.

6.4.4.3 Characterization Comparison

To study the effect of "shared k-space" on plaque characterization more systematically, the PIEC methodology was applied to "full k-space", keyhole and RIGR reconstructed multicontrast MR data separately. Five typical slices (one slice per vessel) were chosen for this comparison.

Because the MR data were acquired with phased-arrayed surface coil, there exists significant amount of inhomogeneity on the multicontrast MR images. The inhomogeneity is explicitly suppressed in the MAGIC-FCM classification step of PIEC. As an example, Figure 40 illustrates MAGIC inhomogeneity correction of the MR images.

When applying PIEC to "full k-space", keyhole and RIGR reconstructed data, corresponding T2 distributions were used in the labeling process as shown in Table 11 that plaque tissues' T2 distributions are different for the three reconstruction schemes.

Generally, PIEC results on keyhole and RIGR data both correlate well with the PIEC results on "full k-space" reconstructed MRI. A typical example is shown in Figure 41. In this figure, it is apparent that the PIEC result on keyhole reconstructed data is very similar to the "reference" (PIEC result on "full k-space" reconstructed multicontrast MRI). Pixel-wise characterization accuracies (PIEC result on "full k-space" reconstructed data was chosen as gold standard), defined in Equation (63), were 96.2% and 87.9% for keyhole

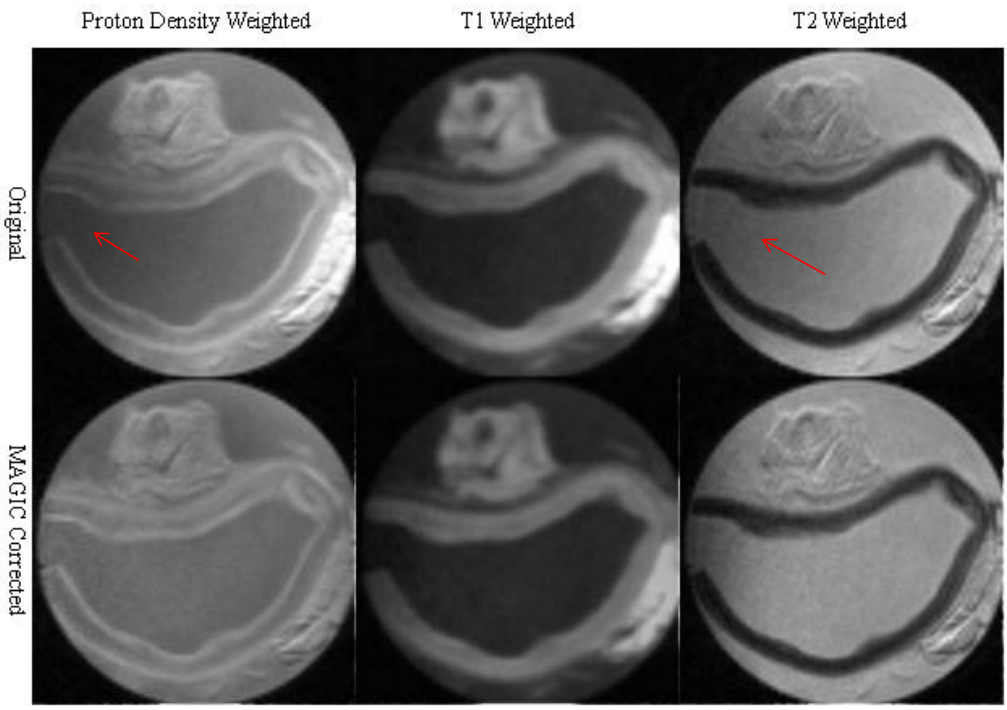

Figure 40: MAGIC-FCM was used in PIEC to perform the segmentation because of the inhomogeneity residing in the MR images. It is shown in this example that MAGIC procedure helps remove the inhomogeneity (arrows) prior to classification.

and RIGR reconstructed data, respectively. This demonstrates the feasibility of "shared k-space" reconstruction in MRI plaque characterization. The better characterization accuracy of PIEC on keyhole data additionally verifies the claim that keyhole reconstruction is more appropriate in accelerating the multicontrast MRI acquisition.

6.4.5 Discussions and Conclusion

In the current chapter, "shared k-space" techniques were interrogated for the possibility of MRI acquisition acceleration. Different from pulse sequence based fast acquisition schemes, these techniques reduce the acquisition time by minimizing the redundant data used in reconstruction. This approach enables "shared k-space" techniques to accelerate the acquisition without sacrificing image resolution and SNR.

The MRI scans were conducted on a 1.5T clinical scanner with phased-arrayed carotid coils. Clinical TSE based sequences were used to acquire the multicontrast MR data. Results from this study show that PIEC on both keyhole and RIGR reconstructed data yields

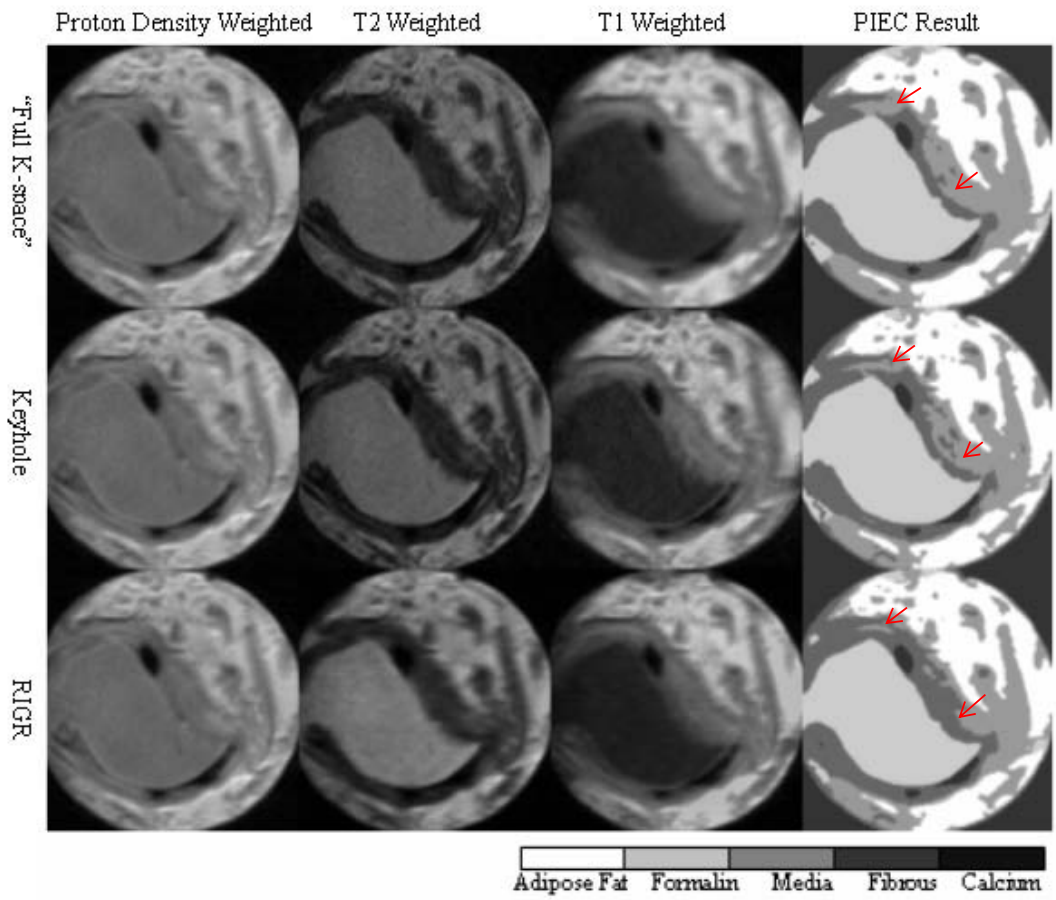

Figure 41: PIEC characterization of "full k-space" (upper row), keyhole (middle row) and RIGR (lower row) reconstructed multicontrast MR images. It appears that PIEC characterization is more accurate (see locations marked by arrow) on keyhole reconstructed data than RIGR reconstructed data.

very accurate characterization results. RIGR reconstruction appears superior to keyhole in suppressing the Gibbs ringing artifact caused by k-space inconsistency. Quantitative comparisons of T2 maps, however, suggest keyhole data are superior to RIGR data in terms of measuring tissues' T2 distributions. Specifically, it was observed that the T2 values of plaque components calculated from RIGR data are poorly separated and deviate significantly from the expectations. On the other hand, T2 values calculated from keyhole data are not statistically different from the true values. Finally, our results show that PIEC characterization is more accurate on keyhole data than RIGR data. One of the major implications of these results is that keyhole is more suitable than RIGR in "shared k-space" multicontrast MRI reconstruction.

Despite multicontrast MRI acquisition is apparently time consuming, there are not a lot of investigations done to mitigate the situation. This is partly due to the fact that multicontrast MRI plaque characterization is still mainly an *ex-vivo* research tool. Another more possible cause is the technical difficulties associated with reducing the acquisition time while keeping reasonably good SNR and resolution for plaque characterization. Most previous studies [30] use very long echo train length (ETL) TSE to expedite acquisition. Recently, Koktzoglou et al. [47] investigated the substitution of steady-state free procession (SSFP) for TSE in MR plaque imaging aiming at improve the acquisition efficiency. Compared to these techniques, "shared k-space" reconstruction evaluated in the current study treats fast multicontrast MRI acquisition from a totally different perspective. The sharing of information across contrast mechanisms makes it possible to combine "shared k-space" approach with other techniques to achieve even more expedited multicontrast MRI acquisition.

Fast acquisition will facilitate the clinical utility of multicontrast MRI, it may benefit the clinical acquisition of DWI as well. Because of the high sensitivity of DWI to bulk water motion, including DWI in multicontrast MRI has foreseeable difficulties in clinical application. This is especially true given the high resolution required for plaque imaging. The reduced k-space coverage in "shared k-space" reconstruction could minimize the effect of physiological motions and make DWI possible under clinical settings.

One of the major limitations of this experiment is the limited number of vessels studied. Therefore, more thorough assessment is needed for further verification. To approximate the clinical conditions as much as possible, the MRI scanning was performed on a patient scanner using clinical pulse sequences. However, since there were no physiological motions associated with the vessels during our data acquisition, "shared k-space" reconstruction techniques may encounter additional difficulties (e.g. misregistration between images of different contrast mechanisms) in patient scans. The current study chose proton density weighted image as the reference image because of its high SNR. Despite the seemingly validity of this choice, it would be interesting to evaluate the performance of "shared k-space" reconstruction using other contrast mechanisms as references. Furthermore, "shared

k-space" reconstruction on diffusion weighted images is also an imperative future work.

In conclusion, "shared k-space" reconstruction is a viable solution in reducing the multicontrast MRI acquisition without sacrificing the image SNR and resolution. Moreover, keyhole reconstruction is more suitable than RIGR in multicontrast MRI because it provides: 1) more accurate quantitative T2 maps, and 2) better tissue characterization and labeling for tissue components.

CHAPTER VII

CONCLUSION AND FUTURE WORK

7.1 The Problem Revisited

Before summarizing the key findings, it is appropriate to revisit the purpose of the current thesis. Overall, this thesis intends to study the feasibility of multicontrast MRI in atherosclerotic plaque characterization. The technical limitations, including resolution, SNR as well as motion, make *in-vivo* plaque characterization, at least in coronary arteries, inapplicable. Therefore, multicontrast MR plaque characterization heavily relies on *ex-vivo* studies. This fact renders plaque characterization routines developed for *ex-vivo* scans questionable for *in-vivo* application. For this reason, the effect of vessel preservation on multicontrast MRI appearance need to be assessed first. After that, automatic plaque characterization algorithm can be developed based on simulated *in-vivo* studies. Finally, fast acquisition schemes are sought to accelerate multicontrast MRI acquisition, which will bring this technique closer to clinical applications.

7.2 Summary of Major Findings

The experiments and theoretical developments are covered from Chapter IV to VI. In Chapter IV, the detailed experiment setup and MRI protocol were described. The comparisons between simulated *in-vivo* scans (fresh) and *ex-vivo* scans (preserved) yielded the following findings:

- The multicontrast MR images of both fresh and preserved vessels correlate well with histology.
- For most plaque tissues except thrombus, the MR signal is virtually unchanged visually. In Chapter V, it is additionally verified that automatic plaque characterization algorithm based on comparative contrast suggests no significant differences between characterization results on fresh and preserved vessels.

- For all typical plaque constituents, quantitative MR properties including T2 and ADC values show small, yet significant, change after the preservation.

The most important inference from the comparisons is that multicontrast MR plaque characterization algorithms developed under *ex-vivo* conditions still apply for *in-vivo* studies.

In Chapter V, an automatic plaque characterization routine, PIEC, combining MAGIC-FCM/SPFCM and Bayesian labeling was developed and evaluated. The evaluation of PIEC on simulated and multicontrast MR coronary images shows that it is a promising technique to replace manual characterization.

Chapter VI investigates the feasibility of "shared k-space" reconstruction in accelerating the multicontrast MRI acquisition. The major findings here include:

- "Shared k-space" reconstruction could be a viable solution in reducing the multicontrast MRI acquisition without sacrificing the SNR and resolution.

- Keyhole reconstruction is more suitable than RIGR in multicontrast MRI because it provides: 1) more accurate quantitative T2 maps, and 2) better tissue characterization and labeling for tissue components.

7.3 Future Work

There are several areas of future work that may extend the current research. First of all, efforts should be spent on investigating new contrast mechanisms to better differentiate plaque components. This includes the developments of both new pulse sequences and new MR contrast agents. At the same time, in order to reduce the data redundancy, it is equally important to find the most efficient combination of MR contrast mechanisms for proper plaque characterization. By addressing the two aspects at the same time, a more effective and efficient multicontrast MRI protocol can be developed.

Second, it is critical to perform more thorough evaluation on both "shared k-space" reconstruction and PIEC characterization employing a bigger dataset. The current research is based on limited data and thus needs more careful inspection before being used clinically.

Third, the theoretical framework of PIEC and "shared k-space" reconstruction can be

advanced. As already indicated, PIEC can include more MR properties and other morphological information to improve the labeling accuracy. Moreover, "shared k-space" techniques can be combined with half Fourier technique to additionally reduce the acquisition time.

7.4 Final Thoughts

Recently, several groups have begun evaluating MR plaque characterization clinically on carotid arteries. Readers interested in a thorough review of these clinical trials is referred to a manuscript published by Yuan et al. [108]. It is likely that this practice will become more widespread with the maturity of both acquisition and analysis techniques. Furthermore, it is anticipated that these results will further research into clinical practices on coronary plaques. The combination of multicontrast MRI and automatic plaque characterization techniques makes this particular area of research fruitful.

REFERENCES

[1] "Heart disease and stroke statistics 2005 update. dallas, tex.: American heart association," 2004.

[2] Adame, I. M., van der Geest, R. J., Wasserman, B. A., Mohamed, M. A., Reiber, J. H., and Lelieveldt, B. P., "Automatic segmentation and plaque characterization in atherosclerotic carotid artery mr images," *Magma*, vol. 16, no. 5, pp. 227–34, 2004. 0968-5243 Clinical Trial Controlled Clinical Trial Journal Article.

[3] Altbach, M. I., Mattingly, M. A., Brown, M. F., and Gmitro, A. F., "Magnetic resonance imaging of lipid deposits in human atheroma via a stimulated-echo diffusion weighted technique," *Magn Reson Med*, vol. 20, no. 2, pp. 319–26, 1991. 0740-3194 Journal Article.

[4] Axel, L., Costantini, J., and Listerud, J., "Technical note - intensity correction in surface-coil mr imaging," *American Journal Of Roentgenology*, vol. 148, no. 2, pp. 418–420, 1987.

[5] Berg, A., Sailer, J., Rand, T., and Moser, E., "Diffusivity- and t2 imaging at 3 tesla for the detection of degenerative changes in human-excised tissue with high resolution: atherosclerotic arteries," *Invest Radiol*, vol. 38, no. 7, pp. 452–9, 2003. 0020-9996 Journal Article.

[6] Bernstein, M. A., King, K. F., and Zhou, Z. J., *Handbook of MRI pulse sequences*. Burlington, MA: Elsevier Academic Press, 2004.

[7] Bezdek, J. C., Ehrlich, R., and Full, W., "Fcm - the fuzzy c-means clustering-algorithm," *Computers & Geosciences*, vol. 10, no. 2-3, pp. 191–203, 1984.

[8] Bezdek, J. C., Hall, L. O., and Clarke, L. P., "Review of mr image segmentation techniques using pattern-recognition," *Medical Physics*, vol. 20, no. 4, pp. 1033–1048, 1993.

[9] Bloembergen, N., Purcell, E. M., and Pound, R. V., "Relaxation effects in nuclear magnetic resonance absorption," *Physical Review*, vol. 73, pp. 679–712, April 1948.

[10] Botnar, R. M., Stuber, M., Kissinger, K. V., Kim, W. Y., Spuentrup, E., and Manning, W. J., "Noninvasive coronary vessel wall and plaque imaging with magnetic resonance imaging," *Circulation*, vol. 102, no. 21, pp. 2582–7, 2000. 1524-4539 Clinical Trial Controlled Clinical Trial Journal Article.

[11] Botnar, R. M., Stuber, M., Lamerichs, R., Smink, J., Fischer, S. E., Harvey, P., and Manning, W. J., "Initial experiences with in-vivo right coronary artery human mr vessel wall imaging at 3 tesla," *J Cardiovasc Magn Reson*, vol. 5, no. 4, pp. 589–94, 2003. 1097-6647 Journal Article.

[12] Brinkmann, B. H., Manduca, A., and Robb, R. A., "Optimized homomorphic unsharp masking for mr grayscale inhomogeneity correction," *Ieee Transactions On Medical Imaging*, vol. 17, no. 2, pp. 161–171, 1998.

[13] Cai, J. M., Hatsukami, T. S., Ferguson, M. S., Small, R., Polissar, N. L., and Yuan, C., "Classification of human carotid atherosclerotic lesions with in-vivo multicontrast magnetic resonance imaging," *Circulation*, vol. 106, no. 11, pp. 1368–73, 2002. 1524-4539 Clinical Trial Journal Article.

[14] Casscells, W., Naghavi, M., and Willerson, J. T., "Vulnerable atherosclerotic plaque: a multifocal disease," *Circulation*, vol. 107, no. 16, pp. 2072–5, 2003. 1524-4539 Journal Article Review Review, Tutorial.

[15] Chen, G., Jespersen, S. N., Pedersen, M., Pang, Q., Horsman, M. R., and Stodkilde-Jorgensen, H., "Intravenous administration of gd-dtpa prior to dwi does not affect the apparent diffusion constant," *Magn Reson Imaging*, vol. 23, no. 5, pp. 685–9, 2005. Journal Article United States.

[16] Clarke, S. E., Beletsky, V., Hammond, R. R., Hegele, R. A., and Rutt, B. K., "Validation of automatically classified magnetic resonance images for carotid plaque compositional analysis," *Stroke*, vol. 37, no. 1, pp. 93–7, 2006. Journal Article United States.

[17] Clarke, S. E., Hammond, R. R., Mitchell, J. R., and Rutt, B. K., "Quantitative assessment of carotid plaque composition using multicontrast mri and registered histology," *Magn Reson Med*, vol. 50, no. 6, pp. 1199–208, 2003. 0740-3194 Journal Article.

[18] Condon, B. R., Patterson, J., Wyper, D., Jenkins, P. A., and Hadley, D. M., "Image nonuniformity in magnetic-resonance-imaging - its magnitude and methods for its correction," *British Journal Of Radiology*, vol. 60, no. 709, pp. 83–87, 1987.

[19] Corti, R., Osende, J. I., Fayad, Z. A., Fallon, J. T., Fuster, V., Mizsei, G., Dickstein, E., Drayer, B., and Badimon, J. J., "In-vivo noninvasive detection and age definition of arterial thrombus by mri," *J Am Coll Cardiol*, vol. 39, no. 8, pp. 1366–73, 2002. 0735-1097 (Print) Evaluation Studies Journal Article.

[20] Dalager-Pedersen, S., Falk, E., Ringgaard, S., Kristensen, I. B., and Pedersen, E. M., "Effects of temperature and histopathologic preparation on the size and morphology of atherosclerotic carotid arteries as imaged by mri," *J Magn Reson Imaging*, vol. 10, no. 5, pp. 876–85, 1999. 1053-1807 Journal Article.

[21] Dawant, B. M., Zijdenbos, A. P., and Margolin, R. A., "Correction of intensity variations in mr-images for computer-aided tissue classification," *Ieee Transactions On Medical Imaging*, vol. 12, no. 4, pp. 770–781, 1993.

[22] de Korte, C. L., van der Steen, A. F., Cepedes, E. I., Pasterkamp, G., Carlier, S. G., Mastik, F., Schoneveld, A. H., Serruys, P. W., and Bom, N., "Characterization of plaque components and vulnerability with intravascular ultrasound elastography," *Phys Med Biol*, vol. 45, no. 6, pp. 1465–75, 2000. 0031-9155 Journal Article.

[23] Demarco, J. K., Rutt, B. K., and Clarke, S. E., "Carotid plaque characterization by magnetic resonance imaging: review of the literature," *Top Magn Reson Imaging*, vol. 12, no. 3, pp. 205–17, 2001. 0899-3459 Journal Article Review Review, Tutorial.

[24] Deriche, R., "Using canny criteria to derive a recursively implemented optimal edge detector," *International Journal Of Computer Vision*, vol. 1, no. 2, pp. 167–187, 1987.

[25] Falk, E., Shah, P. K., and Fuster, V., "Coronary plaque disruption," *Circulation*, vol. 92, no. 3, pp. 657–71, 1995. 0009-7322 Journal Article Review Review, Tutorial.

[26] Fayad, Z. A., "Noncoronary and coronary atherothrombotic plaque imaging and monitoring of therapy by mri," *Neuroimaging Clin N Am*, vol. 12, no. 3, pp. 461–71, 2002. 1052-5149 Journal Article Review.

[27] Fayad, Z. A. and Fuster, V., "Characterization of atherosclerotic plaques by magnetic resonance imaging," *Ann N Y Acad Sci*, vol. 902, pp. 173–86, 2000. 0077-8923 Journal Article Review Review, Tutorial.

[28] Fayad, Z. A. and Fuster, V., "Clinical imaging of the high-risk or vulnerable atherosclerotic plaque," *Circ Res*, vol. 89, no. 4, pp. 305–16, 2001. 1524-4571 Journal Article Review Review, Tutorial.

[29] Fayad, Z. A., Fuster, V., Fallon, J. T., Jayasundera, T., Worthley, S. G., Helft, G., Aguinaldo, J. G., Badimon, J. J., and Sharma, S. K., "Noninvasive in-vivo human coronary artery lumen and wall imaging using black-blood magnetic resonance imaging," *Circulation*, vol. 102, no. 5, pp. 506–10, 2000. 1524-4539 Journal Article.

[30] Fayad, Z. A., Nahar, T., Fallon, J. T., Goldman, M., Aguinaldo, J. G., Badimon, J. J., Shinnar, M., Chesebro, J. H., and Fuster, V., "in-vivo magnetic resonance evaluation of atherosclerotic plaques in the human thoracic aorta: a comparison with transesophageal echocardiography," *Circulation*, vol. 101, no. 21, pp. 2503–9, 2000. 1524-4539 Journal Article.

[31] Franzen, D., Sechtem, U., and Hopp, H. W., "Comparison of angioscopic, intravascular ultrasonic, and angiographic detection of thrombus in coronary stenosis," *Am J Cardiol*, vol. 82, no. 10, pp. 1273–5, A9, 1998. Clinical Trial Journal Article United states.

[32] Fuster, V., "Transcript of dr. fuster's presentation at the 2nd vulnerable patient symposium held by aeha on march 6th in conjuction with the annual conference on american college of cardiology 2004," 2004.

[33] Giddens, D. P., Zarins, C. K., and Glagov, S., "The role of fluid-mechanics in the localization and detection of atherosclerosis," *Journal of Biomechanical Engineering-Transactions of the Asme*, vol. 115, no. 4, pp. 588–594, 1993. Part B Mk818 Times Cited:150 Cited References Count:31.

[34] Glagov, S., Bassiouny, H. S., Giddens, D. P., and Zarins, C. K., "Pathobiology of plaque modeling and complication," *Surg Clin North Am*, vol. 75, no. 4, pp. 545–56, 1995. 0039-6109 Journal Article Review Review, Tutorial.

[35] Glagov, S., Weisenberg, E., Zarins, C. K., Stankunavicius, R., and Kolettis, G. J., "Compensatory enlargement of human atherosclerotic coronary arteries," *N Engl J Med*, vol. 316, no. 22, pp. 1371–5, 1987. 0028-4793 Journal Article.

[36] Glagov, S., Zarins, C., Giddens, D. P., and Ku, D. N., "Hemodynamics and atherosclerosis - insights and perspectives gained from studies of human arteries," *Archives of Pathology & Laboratory Medicine*, vol. 112, no. 10, pp. 1018–1031, 1988. Q3246 Times Cited:460 Cited References Count:159.

[37] Griendling, K. K. and Alexander, R. W., "Oxidative stress and cardiovascular disease," *Circulation*, vol. 96, no. 10, pp. 3264–5, 1997. 0009-7322 Comment Editorial Review Review, Tutorial.

[38] Griswold, M. A., Jakob, P. M., Heidemann, R. M., Nittka, M., Jellus, V., Wang, J., Kiefer, B., and Haase, A., "Generalized autocalibrating partially parallel acquisitions (grappa)," *Magn Reson Med*, vol. 47, no. 6, pp. 1202–10, 2002. Journal Article United States official journal of the Society of Magnetic Resonance in Medicine / Society of Magnetic Resonance in Medicine.

[39] Haacke, E. M., "Magnetic resonance imaging : physical principles and sequence design," 1999.

[40] Hall, L. O., Bensaid, A. M., Clarke, L. P., Velthuizen, R. P., Silbiger, M. S., and Bezdek, J. C., "A comparison of neural network and fuzzy clustering-techniques in segmenting magnetic-resonance images of the brain," *Ieee Transactions On Neural Networks*, vol. 3, no. 5, pp. 672–682, 1992.

[41] Hatsukami, T. S., Ross, R., Polissar, N. L., and Yuan, C., "Visualization of fibrous cap thickness and rupture in human atherosclerotic carotid plaque in-vivo with high-resolution magnetic resonance imaging," *Circulation*, vol. 102, no. 9, pp. 959–64, 2000. R01-hl-60213/hl/nhlbi R29-hl-56874/hl/nhlbi Clinical Trial Journal Article United states.

[42] Hong, X. L. and Dixon, W. T., "Measuring diffusion in inhomogeneous systems in imaging mode using antisymmetric sensitizing gradients," *Journal of Magnetic Resonance*, vol. 99, no. 3, pp. 561–570, 1992. Ju677 Times Cited:31 Cited References Count:8.

[43] Itskovich, V. V., Samber, D. D., Mani, V., Aguinaldo, J. G., Fallon, J. T., Tang, C. Y., Fuster, V., and Fayad, Z. A., "Quantification of human atherosclerotic plaques using spatially enhanced cluster analysis of multicontrast-weighted magnetic resonance images," *Magn Reson Med*, vol. 52, no. 3, pp. 515–23, 2004. 0740-3194 Journal Article.

[44] Jang, I. K., Tearney, G. J., MacNeill, B., Takano, M., Moselewski, F., Iftima, N., Shishkov, M., Houser, S., Aretz, H. T., Halpern, E. F., and Bouma, B. E., "in-vivo characterization of coronary atherosclerotic plaque by use of optical coherence tomography," *Circulation*, vol. 111, no. 12, pp. 1551–5, 2005. 1524-4539 Journal Article.

[45] Johnston, B., Atkins, M. S., Mackiewich, B., and Anderson, M., "Segmentation of multiple sclerosis lesions in intensity corrected multispectral mri," *Ieee Transactions On Medical Imaging*, vol. 15, no. 2, pp. 154–169, 1996.

[46] Jones, R. A., Haraldseth, O., Muller, T. B., Rinck, P. A., and Oksendal, A. N., "K-space substitution: a novel dynamic imaging technique," *Magn Reson Med*, vol. 29, no. 6, pp. 830–4, 1993. Journal Article Research Support, Non-U.S. Gov't United states official journal of the Society of Magnetic Resonance in Medicine / Society of Magnetic Resonance in Medicine.

[47] Koktzoglou, I., Chung, Y. C., Carroll, T. J., Simonetti, O. P., Morasch, M. D., and Li, D., "Three-dimensional black-blood mr imaging of carotid arteries with segmented steady-state free precession: initial experience," *Radiology*, vol. 243, no. 1, pp. 220–8, 2007. Evaluation Studies Journal Article Research Support, Non-U.S. Gov't United States.

[48] Koktzoglou, I., Simonetti, O., and Li, D., "Coronary artery wall imaging: initial experience at 3 tesla," *J Magn Reson Imaging*, vol. 21, no. 2, pp. 128–32, 2005. 1053-1807 Journal Article.

[49] Ku, D. N., Zarins, C. K., Giddens, D. P., and Glagov, S., "Shear-stress oscillation and plaque localization at the carotid bifurcation," *Circulation*, vol. 68, no. 4, pp. 301–301, 1983. Rj593 Times Cited:3 Cited References Count:0.

[50] Kwan, R. K. S., Evans, A. C., and Pike, G. B., "Mri simulation-based evaluation of image-processing and classification methods," *Ieee Transactions On Medical Imaging*, vol. 18, no. 11, pp. 1085–1097, 1999.

[51] Langheinrich, A. C., Bohle, R. M., Greschus, S., Hackstein, N., Walker, G., von Gerlach, S., Rau, W. S., and Holschermann, H., "Atherosclerotic lesions at micro ct: feasibility for analysis of coronary artery wall in autopsy specimens," *Radiology*, vol. 231, no. 3, pp. 675–81, 2004. Comparative Study In Vitro Journal Article United States.

[52] Lauterbu.Pc, "Image formation by induced local interactions - examples employing nuclear magnetic-resonance," *Nature*, vol. 242, no. 5394, pp. 190–191, 1973. P0317 Times Cited:1132 Cited References Count:6.

[53] Liang, Z. P. and Lauterbur, P. C., "A generalized series approach to mr spectroscopic imaging," *Ieee Transactions on Medical Imaging*, vol. 10, no. 2, pp. 132–137, 1991. Fm228 Times Cited:46 Cited References Count:19.

[54] Liang, Z. P. and Lauterbur, P. C., "An efficient method for dynamic magnetic-resonance-imaging," *Ieee Transactions on Medical Imaging*, vol. 13, no. 4, pp. 677–686, 1994. Pz976 Times Cited:39 Cited References Count:20.

[55] Liang, Z.-P., Lauterbur, P. C., in Medicine, I. E., and Society., B., *Principles of magnetic resonance imaging : a signal processing perspective*. IEEE Press series in biomedical engineering, Bellingham, Wash. New York: SPIE Optical Engineering Press ; IEEE Press, 2000. 99027706 Zhi-Pei Liang, Paul C. Lauterbur. ill. ; 24 cm. "IEEE Engineering in Medicine and Biology Society, sponsor." Includes bibliographical references (p. 391-407) and index.

[56] Libby, P., "Molecular bases of the acute coronary syndromes," *Circulation*, vol. 91, no. 11, pp. 2844–50, 1995. Journal Article Review United states.

[57] Libby, P., "Inflammation in atherosclerosis," *Nature*, vol. 420, no. 6917, pp. 868–74, 2002. 0028-0836 Journal Article Review Review, Tutorial.

[58] Liew, A. W. C., Leung, S. H., and Lau, W. H., "Fuzzy image clustering incorporating spatial continuity," *Iee Proceedings-Vision Image And Signal Processing*, vol. 147, no. 2, pp. 185–192, 2000.

[59] Liew, A. W. C. and Yan, H., "An adaptive spatial fuzzy clustering algorithm for 3-d mr image segmentation," *Ieee Transactions On Medical Imaging*, vol. 22, no. 9, pp. 1063–1075, 2003.

[60] Lin, J. S., Cheng, K. S., and Mao, C. W., "Segmentation of multispectral magnetic resonance image using penalized fuzzy competitive learning network," *Computers And Biomedical Research*, vol. 29, no. 4, pp. 314–326, 1996.

[61] Liu, F., Xu, D., Ferguson, M. S., Chu, B., Saam, T., Takaya, N., Hatsukami, T. S., Yuan, C., and Kerwin, W. S., "Automated in-vivo segmentation of carotid plaque mri with morphology-enhanced probability maps," *Magn Reson Med*, vol. 55, no. 3, pp. 659–68, 2006. 0740-3194 (Print) Journal Article.

[62] Lusis, A. J., "Atherosclerosis," *Nature*, vol. 407, no. 6801, pp. 233–41, 2000. 0028-0836 Journal Article Review Review, Tutorial.

[63] Maynor, C. H., Charles, H. C., Herfkens, R. J., Suddarth, S. A., and Johnson, G. A., "Chemical shift imaging of atherosclerosis at 7.0 tesla," *Invest Radiol*, vol. 24, no. 1, pp. 52–60, 1989. 0020-9996 Journal Article.

[64] Meyer, C. R., Bland, P. H., and Pipe, J., "Retrospective correction of intensity inhomogeneities in mri," *Ieee Transactions On Medical Imaging*, vol. 14, no. 1, pp. 36–41, 1995.

[65] Mlynarik, V., Degrassi, A., Toffanin, R., Jarh, O., and Vittur, F., "A method for generating magnetic resonance microimaging t2 maps with low sensitivity to diffusion," *Magn Reson Med*, vol. 35, no. 3, pp. 423–5, 1996. 0740-3194 Journal Article.

[66] Naghavi, M., Falk, E., Hecht, H. S., Jamieson, M. J., Kaul, S., Berman, D., Fayad, Z., Budoff, M. J., Rumberger, J., Naqvi, T. Z., Shaw, L. J., Faergeman, O., Cohn, J., Bahr, R., Koenig, W., Demirovic, J., Arking, D., Herrera, V. L., Badimon, J., Goldstein, J. A., Rudy, Y., Airaksinen, J., Schwartz, R. S., Riley, W. A., Mendes, R. A., Douglas, P., and Shah, P. K., "From vulnerable plaque to vulnerable patient–part iii: Executive summary of the screening for heart attack prevention and education (shape) task force report," *Am J Cardiol*, vol. 98, no. 2A, pp. 2H–15H, 2006. SHAPE Task Force Consensus Development Conference Journal Article Review United States.

[67] Naghavi, M., Libby, P., Falk, E., Casscells, S. W., Litovsky, S., Rumberger, J., Badimon, J. J., Stefanadis, C., Moreno, P., Pasterkamp, G., Fayad, Z., Stone, P. H., Waxman, S., Raggi, P., Madjid, M., Zarrabi, A.,

Burke, A., Yuan, C., Fitzgerald, P. J., Siscovick, D. S., de Korte, C. L., Aikawa, M., Juhani Airaksinen, K. E., Assmann, G., Becker, C. R., Chesebro, J. H., Farb, A., Galis, Z. S., Jackson, C., Jang, I. K., Koenig, W., Lodder, R. A., March, K., Demirovic, J., Navab, M., Priori, S. G., Rekhter, M. D., Bahr, R., Grundy, S. M., Mehran, R., Colombo, A., Boerwinkle, E., Ballantyne, C., Insull, W., J., Schwartz, R. S., Vogel, R., Serruys, P. W., Hansson, G. K., Faxon, D. P., Kaul, S., Drexler, H., Greenland, P., Muller, J. E., Virmani, R., Ridker, P. M., Zipes, D. P., Shah, P. K., and Willerson, J. T., "From vulnerable plaque to vulnerable patient: a call for new definitions and risk assessment strategies: Part i," *Circulation*, vol. 108, no. 14, pp. 1664–72, 2003. Journal Article Review United States.

[68] Naghavi, M., Libby, P., Falk, E., Casscells, S. W., Litovsky, S., Rumberger, J., Badimon, J. J., Stefanadis, C., Moreno, P., Pasterkamp, G., Fayad, Z., Stone, P. H., Waxman, S., Raggi, P., Madjid, M., Zarrabi, A., Burke, A., Yuan, C., Fitzgerald, P. J., Siscovick, D. S., de Korte, C. L., Aikawa, M., Airaksinen, K. E., Assmann, G., Becker, C. R., Chesebro, J. H., Farb, A., Galis, Z. S., Jackson, C., Jang, I. K., Koenig, W., Lodder, R. A., March, K., Demirovic, J., Navab, M., Priori, S. G., Rekhter, M. D., Bahr, R., Grundy, S. M., Mehran, R., Colombo, A., Boerwinkle, E., Ballantyne, C., Insull, W., J., Schwartz, R. S., Vogel, R., Serruys, P. W., Hansson, G. K., Faxon, D. P., Kaul, S., Drexler, H., Greenland, P., Muller, J. E., Virmani, R., Ridker, P. M., Zipes, D. P., Shah, P. K., and Willerson, J. T., "From vulnerable plaque to vulnerable patient: a call for new definitions and risk assessment strategies: Part ii," *Circulation*, vol. 108, no. 15, pp. 1772–8, 2003. Consensus Development Conference Journal Article Review United States.

[69] Nissen, S. E. and Yock, P., "Intravascular ultrasound: novel pathophysiological insights and current clinical applications," *Circulation*, vol. 103, no. 4, pp. 604–16, 2001. 1524-4539 Journal Article Review Review, Tutorial.

[70] Pachot-Clouard, M., Vaufrey, F., Darrasse, L., and Toussainti, J. F., "Magnetization transfer characteristics in atherosclerotic plaque components assessed by adapted binomial preparation pulses," *Magma*, vol. 7, no. 1, pp. 9–15, 1998. 0968-5243 Journal Article.

[71] Pham, D., Prince, J. L., Xu, C. Y., and Dagher, A. P., "An automated technique for statistical characterization of brain tissues in magnetic resonance imaging," *International Journal Of Pattern Recognition And Artificial Intelligence*, vol. 11, no. 8, pp. 1189–1211, 1997.

[72] Pham, D. L., "Spatial models for fuzzy clustering," *Computer Vision And Image Understanding*, vol. 84, no. 2, pp. 285–297, 2001.

[73] Pham, D. L. and Prince, J. L., "Adaptive fuzzy segmentation of magnetic resonance images," *Ieee Transactions On Medical Imaging*, vol. 18, no. 9, pp. 737–752, 1999.

[74] Pipe, J. G., "Motion correction with propeller mri: application to head motion and free-breathing cardiac imaging," *Magn Reson Med*, vol. 42, no. 5, pp. 963–9, 1999.

Journal Article United states official journal of the Society of Magnetic Resonance in Medicine / Society of Magnetic Resonance in Medicine.

[75] Porter, K. E., Varty, K., Jones, L., Bell, P. R., and London, N. J., "Human saphenous vein organ culture: a useful model of intimal hyperplasia?," *Eur J Vasc Endovasc Surg*, vol. 11, no. 1, pp. 48–58, 1996. 1078-5884 (Print) Journal Article.

[76] Pruessmann, K. P., Weiger, M., Scheidegger, M. B., and Boesiger, P., "Sense: sensitivity encoding for fast mri," *Magn Reson Med*, vol. 42, no. 5, pp. 952–62, 1999. Comparative Study Journal Article Research Support, Non-U.S. Gov't United states official journal of the Society of Magnetic Resonance in Medicine / Society of Magnetic Resonance in Medicine.

[77] Raynaud, J. S., Bridal, S. L., Toussaint, J. F., Fornes, P., Lebon, V., Berger, G., and Leroy-Willig, A., "Characterization of atherosclerotic plaque components by high resolution quantitative mr and us imaging," *J Magn Reson Imaging*, vol. 8, no. 3, pp. 622–9, 1998. 1053-1807 Journal Article.

[78] Ross, R., "Atherosclerosis–an inflammatory disease," *N Engl J Med*, vol. 340, no. 2, pp. 115–26, 1999. 0028-4793 Journal Article Review Review, Tutorial.

[79] Rumberger, J. A., Simons, D. B., Fitzpatrick, L. A., Sheedy, P. F., and Schwartz, R. S., "Coronary artery calcium area by electron-beam computed tomography and coronary atherosclerotic plaque area. a histopathologic correlative study," *Circulation*, vol. 92, no. 8, pp. 2157–62, 1995. 0009-7322 Journal Article.

[80] Rutt, B. K., Clarke, S. E., and Fayad, Z. A., "Atherosclerotic plaque characterization by mr imaging," *Curr Drug Targets Cardiovasc Haematol Disord*, vol. 4, no. 2, pp. 147–59, 2004. 1568-0061 Journal Article Review Review, Tutorial.

[81] Serfaty, J. M., Chaabane, L., Tabib, A., Chevallier, J. M., Briguet, A., and Douek, P. C., "Atherosclerotic plaques: classification and characterization with t2 weighted high-spatial-resolution mr imaging– an in vitro study," *Radiology*, vol. 219, no. 2, pp. 403–10, 2001. 0033-8419 Journal Article.

[82] Sharma, S, G. G., "Current trends and future applications of intravascular ultrasound," *Ind J Radiol Imag*, vol. 13, no. 1, pp. 53–60, 2003.

[83] Shinnar, M., Fallon, J. T., Wehrli, S., Levin, M., Dalmacy, D., Fayad, Z. A., Badimon, J. J., Harrington, M., Harrington, E., and Fuster, V., "The diagnostic accuracy of ex-vivo mri for human atherosclerotic plaque characterization," *Arterioscler Thromb Vasc Biol*, vol. 19, no. 11, pp. 2756–61, 1999. 1079-5642 Journal Article.

[84] Simmons, A., Arridge, S. R., Barker, G. J., Cluckie, A. J., and Tofts, P. S., "Improvements to the quality of mri cluster-analysis," *Magnetic Resonance Imaging*, vol. 12, no. 8, pp. 1191–1204, 1994.

[85] Sled, J. G., Zijdenbos, A. P., and Evans, A. C., "A nonparametric method for automatic correction of intensity nonuniformity in mri data," *IEEE Trans Med Imaging*, vol. 17, no. 1, pp. 87–97, 1998. 0278-0062 Journal Article.

[86] Sodickson, D. K. and Manning, W. J., "Simultaneous acquisition of spatial harmonics (smash): fast imaging with radiofrequency coil arrays," *Magn Reson Med*, vol. 38, no. 4, pp. 591–603, 1997. Journal Article United states official journal of the Society of Magnetic Resonance in Medicine / Society of Magnetic Resonance in Medicine.

[87] Stary, H. C., Blankenhorn, D. H., Chandler, A. B., Glagov, S., Insull, W., J., Richardson, M., Rosenfeld, M. E., Schaffer, S. A., Schwartz, C. J., Wagner, W. D., and et al., "A definition of the intima of human arteries and of its atherosclerosis-prone regions. a report from the committee on vascular lesions of the council on arteriosclerosis, american heart association," *Arterioscler Thromb*, vol. 12, no. 1, pp. 120–34, 1992. 1049-8834 Duplicate Publication Journal Article Review.

[88] Stary, H. C., Chandler, A. B., Dinsmore, R. E., Fuster, V., Glagov, S., Insull, W., J., Rosenfeld, M. E., Schwartz, C. J., Wagner, W. D., and Wissler, R. W., "A definition of advanced types of atherosclerotic lesions and a histological classification of atherosclerosis. a report from the committee on vascular lesions of the council on arteriosclerosis, american heart association," *Arterioscler Thromb Vasc Biol*, vol. 15, no. 9, pp. 1512–31, 1995. 1079-5642 Journal Article.

[89] Stary, H. C., Chandler, A. B., Glagov, S., Guyton, J. R., Insull, W., J., Rosenfeld, M. E., Schaffer, S. A., Schwartz, C. J., Wagner, W. D., and Wissler, R. W., "A definition of initial, fatty streak, and intermediate lesions of atherosclerosis. a report from the committee on vascular lesions of the council on arteriosclerosis, american heart association," *Circulation*, vol. 89, no. 5, pp. 2462–78, 1994. 0009-7322 Duplicate Publication Journal Article Review Review, Tutorial.

[90] Styner, M., Brechbuhler, C., Szekely, G., and Gerig, G., "Parametric estimate of intensity inhomogeneities applied to mri," *Ieee Transactions On Medical Imaging*, vol. 19, no. 3, pp. 153–165, 2000.

[91] Sun, B., Giddens, D. P., Long, R., J., Taylor, W. R., Weiss, D., Joseph, G., Vega, D., and Oshinski, J. N., "Characterization of coronary atherosclerotic plaque using multicontrast mri acquired under simulated in-vivo conditions," *J Magn Reson Imaging*, vol. 24, no. 4, pp. 833–41, 2006. R01 hl70531/hl/nhlbi Comparative Study In Vitro Journal Article Research Support, N.I.H., Extramural United States Jmri.

[92] Tincher, M., Meyer, C. R., Gupta, R., and Williams, D. M., "Polynomial modeling and reduction of rf body coil spatial inhomogeneity in mri," *Ieee Transactions On Medical Imaging*, vol. 12, no. 2, pp. 361–365, 1993.

[93] Toussaint, J. F., LaMuraglia, G. M., Southern, J. F., Fuster, V., and Kantor, H. L., "Magnetic resonance images lipid, fibrous, calcified, hemorrhagic, and thrombotic components of human atherosclerosis in-vivo," *Circulation*, vol. 94, no. 5, pp. 932–8, 1996. 0009-7322 Journal Article.

[94] Toussaint, J. F., Southern, J. F., Fuster, V., and Kantor, H. L., "T2 weighted contrast for nmr characterization of human atherosclerosis," *Arterioscler Thromb Vasc Biol*, vol. 15, no. 10, pp. 1533–42, 1995. 1079-5642 Journal Article.

[95] Toussaint, J. F., Southern, J. F., Fuster, V., and Kantor, H. L., "Water diffusion properties of human atherosclerosis and thrombosis measured by pulse field gradient nuclear magnetic resonance," *Arterioscler Thromb Vasc Biol*, vol. 17, no. 3, pp. 542–6, 1997. 1079-5642 Journal Article.

[96] Uchida, Y., Nakamura, F., Tomaru, T., Morita, T., Oshima, T., Sasaki, T., Morizuki, S., and Hirose, J., "Prediction of acute coronary syndromes by percutaneous coronary angioscopy in patients with stable angina," *Am Heart J*, vol. 130, no. 2, pp. 195–203, 1995. Clinical Trial Journal Article United states.

[97] van Vaals, J. J., Brummer, M. E., Dixon, W. T., Tuithof, H. H., Engels, H., Nelson, R. C., Gerety, B. M., Chezmar, J. L., and den Boer, J. A., "Keyhole method for accelerating imaging of contrast agent uptake," *J Magn Reson Imaging*, vol. 3, no. 4, pp. 671–5, 1993. 1053-1807 Journal Article.

[98] Vinitski, S., Consigny, P. M., Shapiro, M. J., Janes, N., Smullens, S. N., and Rifkin, M. D., "Magnetic resonance chemical shift imaging and spectroscopy of atherosclerotic plaque," *Invest Radiol*, vol. 26, no. 8, pp. 703–14, 1991. 0020-9996 Journal Article.

[99] Virmani, R., Kolodgie, F. D., Burke, A. P., Farb, A., and Schwartz, S. M., "Lessons from sudden coronary death: a comprehensive morphological classification scheme for atherosclerotic lesions," *Arterioscler Thromb Vasc Biol*, vol. 20, no. 5, pp. 1262–75, 2000. 1079-5642 Journal Article Review Review, Tutorial.

[100] Vlaardingerbroek, M. T., *Magnetic resonance imaging : theory and practice*. Physics and astronomy online library, Berlin ; New York: Springer, 3rd ed., 2003. 2002030464 Marinus T. Vlaardingerbroek, Jacques A. den Boer ; with a historical introduction by Andre Luiten. ill. ; 24 cm. Includes bibliographical references (p. [477]-491) and index.

[101] Vlaardingerbroek, M. T. and Boer, J. A. d., *Magnetic resonance imaging : theory and practice*. Berlin ; New York: Springer, 2nd, rev. and enl. ed., 1999. 99036438 Marinus T. Vlaardingerbroek, Jacques A. den Boer ; with a foreword by Freek Knoet and a historical introduction by Andre Luiten. ill. ; 25 cm. Includes bibliographical references (p. [461]-474) and indexes.

[102] von Ingersleben, G., Schmiedl, U. P., Hatsukami, T. S., Nelson, J. A., Subramaniam, D. S., Ferguson, M. S., and Yuan, C., "Characterization of atherosclerotic plaques at the carotid bifurcation: correlation of high-resolution mr imaging with histologic analysis–preliminary study," *Radiographics*, vol. 17, no. 6, pp. 1417–23, 1997. 0271-5333 Journal Article.

[103] Wells, W. M., Grimson, W. E. L., Kikinis, R., and Jolesz, F. A., "Adaptive segmentation of mri data," *Ieee Transactions On Medical Imaging*, vol. 15, no. 4, pp. 429–442, 1996.

[104] Wicks, D. A. G., Barker, G. J., and Tofts, P. S., "Correction of intensity nonuniformity in mr images of any orientation," *Magnetic Resonance Imaging*, vol. 11, no. 2, pp. 183–196, 1993.

[105] Yang, F., Holzapfel, G., Schulze-Bauer, C., Stollberger, R., Thedens, D., Bolinger, L., Stolpen, A., and Sonka, M., "Segmentation of wall and plaque in in vitro vascular mr images," *Int J Cardiovasc Imaging*, vol. 19, no. 5, pp. 419–28, 2003. 1569-5794 Journal Article.

[106] Yuan, C., Beach, K. W., Smith, L. H., J., and Hatsukami, T. S., "Measurement of atherosclerotic carotid plaque size in-vivo using high resolution magnetic resonance imaging," *Circulation*, vol. 98, no. 24, pp. 2666–71, 1998. 0009-7322 Journal Article.

[107] Yuan, C. and Kerwin, W. S., "Mri of atherosclerosis," *J Magn Reson Imaging*, vol. 19, no. 6, pp. 710–9, 2004. 1053-1807 Journal Article Review.

[108] Yuan, C., Kerwin, W. S., Yarnykh, V. L., Cai, J., Saam, T., Chu, B., Takaya, N., Ferguson, M. S., Underhill, H., Xu, D., Liu, F., and Hatsukami, T. S., "Mri of atherosclerosis in clinical trials," *NMR Biomed*, vol. 19, no. 6, pp. 636–54, 2006. Journal Article Review England.

[109] Yuan, C., Mitsumori, L. M., Ferguson, M. S., Polissar, N. L., Echelard, D., Ortiz, G., Small, R., Davies, J. W., Kerwin, W. S., and Hatsukami, T. S., "In-vivo accuracy of multispectral magnetic resonance imaging for identifying lipid-rich necrotic cores and intra-plaque hemorrhage in advanced human carotid plaques," *Circulation*, vol. 104, no. 17, pp. 2051–6, 2001. 1524-4539 Clinical Trial Journal Article.

[110] Zarins, C. K., Giddens, D. P., Balasubramanian, K., Sottiurai, V., Mabon, R. F., and Glagov, S., "Carotid plaques localize in regions of low flow velocity and shear-stress," *Arteriosclerosis*, vol. 1, no. 5, pp. A358–A358, 1981. Mq704 Times Cited:2 Cited References Count:0.

[111] Zhu, C. Z. and Jiang, T. Z., "Multicontext fuzzy clustering for separation of brain tissues in magnetic resonance images," *Neuroimage*, vol. 18, no. 3, pp. 685–696, 2003.

VITA

Binjian Sun was born in Shenyang, China. He received his Bachelor of Science degree in Biomedical Engineering from Tianjin University, Tianjin, China, in 2002. Since then, he has been pursuing his Ph.D. degree in Bioengineering at the Wallace H. Coulter department of Biomedical Engineering of Georgia Institute of Technology and Emory University, Atlanta, GA, USA. During this period, he also worked as a graduate research assistant at the Fredrik Philips MR Research Center of the Radiology Department in the Emory university Hospital. His research interests span Cardiovascular Magnetic Resonance Imaging, Image Segmentation and/or Tissue Classification, Pattern Recognition and Image Reconstruction.